Strål
säkerhets
myndigheten
Swedish Radiation Safety Authority

Forskning

2012:12

APRI-7 Accident Phenomena of Risk Importance

En lägesrapport om forskningen inom området svåra haverier under åren 2009-2011

Rapportnummer: 2012:12 ISSN:2000-0456
Tillgänglig på www.stralsakerhetsmyndigheten.se

Strål
säkerhets
myndigheten
Swedish Radiation Safety Authority

Redaktörer: Ninos Garis[1], Maria Agrell[1],Henrik Glänneskog[2], Lennart Agrenius[3]
Bidragit till olika avsnitt: Wiktor Frid[1], Ninos Garis[1], Jan-Olov Liljenzin[4], Weimin Ma[5], Pavel Kudinov[6],
Annan personal från Avd för Kärnkraftssäkerhet vid KTH Christian Ekberg[6], Joachim Holm[6], Mark Foreman[6] och Sabrina Tietze[6]

[1)]SSM, [2)]Vattenfall Research and Development, [3)]Agrenius Ingenjörsbyrå AB, [4)]Liljenzins data och kemikonsult, [5)]KTH, [6)]Chalmers

2012:12

APRI-7 Accident Phenomena of Risk Importance

En lägesrapport om forskningen inom området svåra haverier under åren 2009-2011

Rapportnummer: 2012:12 **ISSN:**2000-0456
Tillgänglig på www.stralsakerhetsmyndigheten.se

Denna rapport har tagits fram på uppdrag av Strålsäkerhetsmyndigheten, SSM. De slutsatser och synpunkter som presenteras i rapporten är författarnas och överensstämmer inte nödvändigtvis med SSM:s.

SSM 2012:12

Forskningsprojektet APRI-7 har genomförts i samarbete mellan följande organisationer:

- Strålsäkerhetsmyndigheten (SSM)
- Ringhals AB (RAB)
- OKG Aktiebolag (OKG)
- Forsmarks Kraftgrupp AB (FKA)

Projektet har varit underställd en styrgrupp med representanter från SSM och kraftbolagen enligt följande:

Mauritz Gärdinge, OKG (ordförande)
Ninos Garis, SSM
Johan Ljung, SSM (t o m våren 2011)
Anders Henoch, RAB
Staffan Dittmer, RAB (f o m 2010)
Henrik Glänneskog, RAB (2009)
Margareta Tanse Larsson, FKA
Lennart Agrenius, Agrenius Ingenjörsbyrå AB (projektledare)

Arbetet har genomförts i projektform med deltagande från parterna och andra svenska och utländska uppdragstagare och samarbetspartners.

Redaktörer:

Ninos Garis, SSM
Maria Agrell, SSM
Henrik Glänneskog, Vattenfall Research and Development
Lennart Agrenius, Agrenius Ingenjörsbyrå AB

Personer som har bidragit till olika avsnitt:

Wiktor Frid, SSM
Ninos Garis, SSM
Jan-Olov Liljenzin, Liljenzins data och kemikonsult
Weimin Ma, KTH
Pavel Kudinov, KTH
Annan personal från Avd för Kärnkraftssäkerhet vid KTH
Christian Ekberg, Chalmers
Joachim Holm, Chalmers
Mark Foreman, Chalmers
Sabrina Tietze, Chalmers

SAMMANFATTNING

Kunskap om de fenomen som kan uppträda vid svåra haverier i en kärnkraftanläggning är en viktig förutsättning för att kunna förutse anläggningens beteende, för att kunna utforma rutiner och instruktioner för haverihantering, för beredskapsplaneringen samt för att få god kvalitet på haverianalyser och riskstudier.

Sedan början på 80-talet har kärnkraftföretagen och myndigheten i Sverige samarbetat inom forskningsområdet svåra reaktorhaverier. Samarbetet i början var framför allt knutet till att förstärka skyddet mot omgivningskonsekvenser efter ett svårt reaktorhaveri genom att bl.a. ta fram system för filtrerad tryckavlastning av reaktorinneslutningen. Sedan början på 90-talet har samarbetet delvis ändrat karaktär och inriktats mer på fenomenologiska frågor av riskdominerande betydelse.

Under åren 2009-2011 har samarbetet fortsatt inom forskningsprogrammet APRI-7. Syftet har varit att visa om de lösningar som har valts i den svenska strategin för haverihantering ger ett tillräckligt skydd för omgivningen. Detta sker genom att få fördjupad kunskap om dels viktiga fenomen vid härdsmälteförlopp, dels mängden radioaktivitet som kan släppas ut till omgivningen vid ett svårt haveri.

För att nå syftet har forskningsprogrammet omfattat dels uppföljning av den internationella forskningen inom svåra haverier och utvärdering av resultaten, dels fortsatt stöd till forskningen på KTH och Chalmers om svåra haverier.

Uppföljningen av den internationella forskningen har främjat utbyte av kunskap och erfarenheter samt har gett tillgång till en mängd information om olika fenomen av betydelse för händelseförlopp vid svåra haverier. Detta är viktigt för att erhålla en god bedömningsgrund av de utsläppsbegränsande åtgärderna i svenska kärnkraftsreaktorer.

Det fortsatta stödet till KTH har gett ökad kunskap om möjligheten att kyla den smälta härden i reaktortanken och om processer i samband med kylbarheten i inneslutningen samt vid ångexplosioner. Ett beräkningsverktyg har vidareutvecklats för att analysera en härdsmälta i reaktortankens botten. Beräkningarna visar att ett kylflöde genom drivdonen kan ge möjlighet att fördröja tankgenomsmältning men riskerar att försvåra det fortsatta förloppet om tankgenomsmältning ändå sker. Experiment och analyser visar att porositeten hos grusbädden är hög och att geometrier med ett isolerande lager av fina partiklar ovanpå en grusbädd är mindre sannolika. Båda resultaten visar på ökad kylbarhet jämfört med tidigare bedömningar. Minskande vattendjup och/eller ökande diameter på smältstrålen ökar risken för en ickekylbar konfiguration. Genomförd forskning om ångexplosioner har gett oss ökad detaljkunskap men denna är ännu inte tillräcklig för att ge full förståelse av förloppet vid en ångexplosion i samband med en härdsmälta.

Baserat på resultaten av forskningen vid KTH, görs bedömningen att det inte är realistiskt att på helt deterministisk grund kunna avgöra hur en haverisekvens utvecklas.

Stödet till Chalmers har gett ökad kunskap om haverikemi, främst jods uppförande i inneslutningen och scrubbern efter ett haveri. Förståelsen av det grundläggande sambandet för fördelning av metyljodid mellan vatten och gasfas har ökat. Experiment och analyser har klarställt att redoxpotentialen i en vattenmiljö har en underordnad betydelse för förmågan att kvarhålla jod så länge som pH hålls ovanför det sura området. Det finns förutsättningar att förstärka scrubberns jodavskiljande förmåga med tillsats av en organisk fosforförening.

INNEHÅLLSFÖRTECKNING

1. INLEDNING

Kunskap om de fenomen som kan uppträda vid svåra haverier i en kärnkraftanläggning är en viktig förutsättning för att kunna förutse anläggningens beteende, för att kunna utforma rutiner och instruktioner för haverihantering, för beredskapsplaneringen samt för att få god kvalitet på haverianalyser och riskstudier.

De svenska parterna, SSM (tidigare SKI) och kraftföretagen i Sverige har under en följd av år samarbetat inom forskningsområdet svåra reaktorhaverier. Detta har skett inom projekten FILTRA, RAMA, RAMA II, RAMA III, HAFOS, APRI, APRI 2, APRI 3, APRI 4, APRI 5 och APRI 6. TVO har deltagit i projekten APRI, APRI 3 och APRI 4.

FILTRA- och RAMA-projekten var knutna till processen att utforma, genomföra och verifiera de haveriförebyggande och konsekvenslindrande åtgärder som 1989 införts vid samtliga kärnkraftverk.

I projekten HAFOS, APRI, APRI 2, APRI 3, APRI 4, APRI 5 och APRI 6 var en viktig uppgift att följa internationell forskning rörande svåra härdhaverier. En annan uppgift var att stödja eget arbete inom Sverige där forskningen på härdsmälteförlopp genomförts vid KTH och kemiska förhållanden i inneslutningen har undersökts vid Chalmers.

APRI 7-projektet har i stora drag haft samma inriktning som tidigare APRI.

I slutet av projektperioden (den 11 mars 2011) inträffade en naturkatastrof i Japan som medförde att reaktorerna 1-4 vid Fukushima Dai-ichi havererade. Haverisekvensen så som den är känd har värderats av APRI-projektet och slutsatsen är att inga avgörande okända fenomen har identifierats.

1.1 Kort historik

Sedan början på 80-talet har kärnkraftföretagen i Sverige och myndigheten samarbetat inom forskningsområdet svåra reaktorhaverier. Samarbetet i början var framför allt knutet till att förstärka skyddet mot omgivningskonsekvenser efter ett svårt reaktorhaveri genom att bl.a. ta fram system för filtrerad tryckavlastning av reaktorinneslutningen. Sedan början på 90-talet, har samarbetet delvis ändrat karaktär och inriktats mer på fenomenologiska frågor av riskdominerande betydelse.

I början av 1986 beslutade regeringen att som villkor för fortsatt drift skulle utsläppsbegränsande åtgärder vidtas vid reaktorerna i Forsmark, Oskarshamn och Ringhals. Åtgärderna skulle vara genomförda senast vid utgången av 1988. I anslutning till dessa regeringsbeslut uppdrog[1] regeringen åt dåvarande Statens kärnkraftinspektion (SKI) att utöver redovisning av beslut som myndigheten fattat med anledning av regeringens nya driftvillkor även redovisa en bedömning av behovet av fortsatta insatser inom området svåra haveriförlopp.

[1] Regeringsbeslut 14 ”Uppdrag att redovisa det fortsatta arbetet att begränsa utsläpp vid svåra reaktorhaverier”. Industridepartementet 1986-02-27.

Efter myndighetens granskning av de åtgärder som vidtagits vid berörda anläggningar konstaterades i ett beslut[2] av den 19 december 1988 att de mål som regeringen angivit som villkor för fortsatt drift hade uppfyllts. I myndighetens beslut pekades emellertid också på att tillståndshavarna även fortsättningsvis behövde följa de forsknings- och utvecklingsinsatser som bedrevs och dra slutsatser om vilka ytterligare säkerhetshöjande åtgärder som bör komma ifråga vid de egna anläggningarna.

I slutet av 1990-talet förtydligades myndighetens allmänna krav på utsläppsbegränsande åtgärder genom föreskrifterna SSMFS 2008:1 (tidigare SKIFS 1998:1 och SKIFS 2004:1) om säkerhet i kärntekniska anläggningar. I föreskrifterna ställdes krav på att radiologiska olyckor skall förebyggas genom en för varje anläggning anpassad grundkonstruktion med flera barriärer och ett anpassat djupförsvar. Bestämmelserna om djupförsvar innehåller bl.a. krav på att utsläpp av radioaktiva ämnen till omgivningen skall förhindras och begränsas genom anordningar och förberedda åtgärder. I föreskrifterna infördes även krav på att säkerheten vid en anläggning fortlöpande skall analyseras och bedömas på ett systematiskt sätt, och i allmänna råd pekades på att bl.a. forskningsresultat särskilt bör beaktas vid sådan fortlöpande analys och bedömning.

Genom föreskrifterna SSMFS 2008:17 (tidigare SKIFS 2004:2) om konstruktion och utförande av kärnkraftsreaktorer har myndigheten sedan ytterligare förtydligat och skärpt kraven i vissa avseenden. Även svåra haverier med större härdskador skall beaktas när det gäller konstruktionen av inneslutningsfunktionen, instrumentering för övervakning av anläggningens tillstånd, samt för att kunna uppnå ett stabilt sluttillstånd med reaktorn så att den inte utgör ett hot mot omgivningen på lång sikt. I konsekvensutredningen[3] av föreskrifterna konstaterades att dessa krav, som inte fanns då reaktorerna konstruerades, tillkom i viss omfattning genom regeringsbeslutet om utsläppsbegränsande åtgärder 1986.

Den svenska strategin för haverihantering innebär att inneslutningarna försetts med förstärkt inneslutningskylning, tryckavlastning och filtrering av utsläpp. Den svenska strategin för att hantera en härdsmälta - att låta en härdsmälta falla i djupt vatten i inneslutningen – har visat sig vara ovanlig. Endast i ett fåtal andra reaktorer i världen tillämpas denna strategi aktivt. Eftersom den svenska strategin är ovanlig, finns det mycket lite internationell forskning som direkt belyser denna. Dock bedrivs internationell forskning om fenomen som även kan inträffa under ett svårt haveri i ett svenskt verk.

Det finns kvarvarande osäkerheter förknippade med den svenska strategin som behöver belysas ytterligare genom forskning. Genom den svenska strategin undviks troligen en stor inledande interaktion mellan betong och smälta. Å andra sidan kan ångexplosioner inträffa när smältan faller i djupt vatten. Forskningen på svåra haverier inriktas nu på att visa om de lösningar som har valts ger ett tillräckligt skydd för

---

[2] SKI-beslut ”Utsläppsbegränsande åtgärder vid kärnkraftverken i Forsmark, Oskarshamn och Ringhals”. SKI 1988-12-19.

[3] Konsekvensutredning av Statens kärnkraftinspektions förslag till föreskrifter (SKIFS 2004:2) om konstruktion och utförande av kärnkraftsreaktorer, Statens kärnkraftinspektion 2004-10-07.

omgivningen, vilket vi idag håller för troligt med vissa osäkerheter som nämnts ovan.

Utgående från regeringens och myndighetens beslut i slutet av 1980-talet har myndigheten och tillståndshavarna tillsammans fortsatt att bedriva forskning om svåra haverier samt följa upp internationell forskning.

1.2 Projektets syfte

Projektet syftar till att visa om de lösningar som har valts i den svenska strategin för haverihantering ger ett tillräckligt skydd för omgivningen. Detta sker genom att få fördjupad kunskap om dels viktiga fenomen vid härdsmälteförlopp, dels mängden radioaktivitet som kan släppas ut till omgivningen vid ett svårt haveri.

För att nå syftet och i enlighet med rekommendationerna från APRI-6 (SSM rapport 2009:25) har projektet arbetat med följande uppgifter:

- att följa den internationella forskningen inom svåra haverier och utvärdera resultaten för att erhålla en god bedömningsgrund av de utsläppsbegränsande åtgärderna i svenska kärnkraftsreaktorer.
- att fortsätta att stödja forskningen på KTH och Chalmers om svåra haverier.
- att speciellt studera vissa fenomen som t ex smältans kylbarhet i reaktor-tanken och i reaktorinneslutningen samt haverikemi.

1.3 Organisation och arbetsformer

Projektet har bedrivits under åren 2009 - 2011 med en total kostnadsram på 20,0 MSEK. SSM och kraftföretagen har bidragit med ungefär hälften var till denna budget. Arbetet inom projektet har varit uppdelat i 11 delprojekt med var sin delprojektledare.

1.3.1. Deltagande i CSARP - NRC:s forskningsprogram

Delprojektledare har varit Wiktor Frid, SSM. En redogörelse för denna verksamhet ges i avsnitt 2.1

1.3.2. Deltagande i SARNET – Integration av EU:s forskning inom svåra haverier

Delprojektledare har varit Ninos Garis, SSM. En redogörelse för denna verksamhet ges i avsnitt 2.2

1.3.3. Deltagande i PHEBUS – Experiment med härdsmältor

Delprojektledare har varit Prof. Jan-Olov Liljenzin, Chalmers. En redogörelse för denna verksamhet ges i avsnitt 2.3.

1.3.4. Deltagande i MCCI 2 – Växelverkan mellan härdsmälta och betong

Delprojektledare har varit Wiktor Frid. En redogörelse för denna verksamhet ges i avsnitt 2.4.

1.3.5. Deltagande i SERENA2 – Ångexplosioner i reaktorinneslutningen

Delprojektledare har varit Wiktor Frid, SSM. En redogörelse för denna verksamhet ges i avsnitt 2.5.

1.3.6. Deltagande i BIP – Jodkemi i reaktorinneslutningen

Delprojektledare har varit Prof. Christian Ekberg. En redogörelse för denna verksamhet ges i avsnitt 2.6.

1.3.7. KTH:s forskning inom svåra haverier

Forskningen vid KTH beskrivs i kap. 3 och har följts upp av styrgruppen genom två möten per år. Under perioden har forskningen behandlat följande: Smältans kylbarhet i reaktortanken beskrivs i avnsitt 3.2, smältans/partikelbäddens formbildning beskrivs i avsnitt 3.3, smältans kylbarhet i reaktorinneslutningen beskrivs i avsnitt 3.4, ångexplosioner beskrivs i avsnitt 3.5 och värderingen av forskningen inom SARNET beskrivs i avsnitt 3.6.

1.3.8. Chalmers forskning inom svåra haverier

Forskningen vid Chalmers beskrivs i kap. 4 och har följts upp av styrgruppen genom ett möte per år. Forskningen under perioden har behandlat följande: Allmän beskrivning av jodkemi under svåra haverier ges i avsnitt 4.1, undersökning av kabelisoleringsmaterial som t ex Hypalon redovisas i avsnitt 4.2, samarbetet mellan Chalmers och VTT avseende studier av radiolytisk oxidation av jod beskrivs i avsnitt 4.3, potentiostatmätningar av vatten-jod-systemet redovisas i avsnitt 4.4, egenskaper hos metyljodid i avsnitt 4.5, modifiering av scrubberlösning för att bättre fånga metyljodid beskrivs i avsnitt 4.6, studier av hur jod i olika former reagerar med färger i inneslutningen redovisas i avsnitt 4.7 och värderingen av forskningen inom SARNET beskrivs i avsnitt 4.8.

1.3.9. Handbok i haverikemi

Arbetet med att ta fram en handbok i haverikemi har väsentligen slutförts under perioden. Det finns en draft framme i dagsläget och KSU har fått i uppdrag att göra ett tryckbart manus av materialet. Planen är att ge ut handboken vid halvårsskiftet 2012.

1.4 Erfarenhetsutbyte och seminarier

Ett slutseminarium med ca 60 deltagare arrangerades i APRI:s regi den 25-26 januari 2012 på Johannesbergs slott, Stockholm. Seminariets syfte var att presentera det arbete som utförts och de resultat som erhållits inom projektet APRI-7. Ett annat syfte med seminariet var också att ge möjlighet till diskussioner mellan representanter för kraftverken och de som deltagit i APRI:s arbete.

1.5 Ekonomi och rapportering

Ekonomiskt har en viss omfördelning skett mellan olika delprojekt och några nya delprojekt har tillkommit men den totala budgetramen har innehållits.

De olika delprojekten har genererat publicerade artiklar, reserapporter och dylikt vilket framgår av referenslistan i varje kapitel.

2. INTERNATIONELL FORSKNING INOM SVÅRA HAVERIER

2.1 CSARP – NRC:s Forskningsprogram

CSARP står för ”Cooperative Severe Accident Research Programme” och var från början den amerikanska kärnsäkerhetsmyndigheten NRC:s (Nuclear Regulatory Commissions) forskningsprogram om svåra haverier. Numera deltar de flesta kärnkraftsländer, inklusive Sverige och Finland, i CSARP-programmet där man utbyter forskningsresultat och erfarenheter samt gemensamt diskuterar inriktning och prioriteringar av fortsatt forskning inom området svåra haverier. CSARP-möten hålls årligen i september månad i USA.

I direktanslutning till ett CSARP-möte hålls ett MCAP-möte (MELCOR Cooperative Assessment Program) om applikationer av MELCOR-koden. MELCOR har blivit ett väletablerat verktyg för analys av svåra haverier och antalet användare världen över växer. MELCOR används mer och mer för beräkningar på nya reaktorkoncept och för haveriscenarier med stora härdskador.

Under CSARP-mötena redovisas forskning om olika haverifenomen och detta gäller speciellt de internationella projekt som pågår inom området, som t ex OECD MCCI 2, OECD SERENA, OECD BIP 2, PHEBUS, SARNET, etc. En annan punkt på dagordningen är utveckling och validering av olika programkoder. En tredje punkt berör kodutveckling för nya reaktorkoncept. Under CSARP-mötet för år 2011 hölls även en session om händelsen i Fukushima.

För mer information hänvisas till följande reserapporter utgivna av Vattenfall Power Consultant:

1. Reserapport från CSARP-möte, 15-18 september, 2009, Bethesda (USA), T-CKA 09-39, Vattenfall Power Consultant, 2010-01-25.
2. Reserapport från CSARP-möte, 14-16 september, 2010, Bethesda (USA), T-NSS 10-72, Vattenfall Power Consultant, 2010-10-20.
3. Reserapport från CSARP-möte, 20-22 september, 2011, Bethesda (USA), AE-NNR 11-45, Vattenfall Power Consultant, 2011-09-23.

2.2 SARNET2 – Integration av EU:s forskning inom svåra haverier

I april 2004 bildades nätverket SARNET (Severe Accident Research – NETwork of excellence) för att bl.a. samordna forskningen inom svåra haverier inom EU. Avsikten var att SARNET efter en 4-års period skulle leva vidare av egen kraft. Så blev dock inte fallet, utan i början av 2009 bestämdes att projektet skulle fortsätta, dvs. SARNET 2, och pågå under fyra år med fortsatt stöd från EU.

Främsta syftet med SARNET 2 är att uppnå ett tillräckligt bra kunskapsläge om ett antal återstående frågor inom området. Vid genomgång av olika haverifenomen fick följande frågor högsta prioritet: Härdens kylbarhet under återflödning, härdresternas kylning efter tankgenomsmältning, ångexplosioner efter tankgenomsmältning, om-

blandning och förbränning av vätgas i inneslutningen, frigörelse av rutenium efter tankgenomsmältning, jodkemi i primärsystem och inneslutning.

I projektet deltar 41 organisationer (8 universitet, 23 forskningsorganisationer, 5 kraftföretag och 5 myndigheter) från 21 länder (18 europeiska plus USA, Kanada och Korea). Från Sverige deltar Chalmers och KTH.

Verksamheten inom projektet omfattar följande uppgifter att:

a) genomföra experiment och analysera dessa för att få bättre förståelse för fenomen,
b) fortsätta utvecklingen av haverianalyskoden ASTEC[4] baserat på ny kunskap om haverifenomen,
c) lagra resultat från experiment i databaser och
d) sprida kunskap om svåra haverier genom att anordna konferenser och kurser.

Ett exempel på det senare är att presentera och diskutera resultaten från SARNET vid ERMSAR[5]-möten vilka arrangeras ungefär vartannat år. Senaste ERMSAR-mötet hölls den 11-12 maj 2010 i Bologna (Italien), se reserapport från Vattenfall Power Consultant, T-NA 10-49, 2010-08-25. För ytterligare information om SARNET, hänvisas till nätverkets hemsida: http://www.sar-net.eu/

2.3 PHEBUS – Experiment med härdsmältor

PHEBUS är namnet på en reaktor som ligger i Cadarache (södra Frankrike). Det är en bassängreaktor med höganrikat bränsle och en central experimentkanal. År 1985 föreslog det franska atomenergiorganet CEA (Commissariat à l'Energie Atomique) att anläggningen skulle kunna utnyttjas för en serie integrala studier av frigörelse, transport och avskiljning av fissionsprodukter (FP) under simulerade svåra haverier med härdsmälta. Avsikten var i första hand att studera dels härdsmältans beteende vid ett antaget reaktorhaveri, dels hur fissionsprodukter frigörs från en överhettad reaktorhärd och deponeras i reaktorns primärsystem och dess inneslutning. Syftet var även att med hjälp av erhållna data kontrollera funktionen hos olika haverikoder samt att klarlägga om man eventuellt missat något integralt fenomen. Anläggningen visas i stiliserad form i figur 2.3.1.

För att genomföra projektet modifierades reaktorn och speciella heta celler byggdes i samma hus. Under år 1988 skrevs kontrakt mellan CEA, energibolaget EDF (Électricité de France) och EG (Europeiska Gemenskapen) om sex experiment. Fler deltagare/finansiärer inbjöds vilket ledde till att även USA (NRC), Kanada (CANDU Owners Group), Japan (MITI), Korea (KAERI) och Schweiz (HSK) blev deltagare. Sverige avstod men deltog senare i projektet i och med vårt inträde i EU.

Projektet är nu i princip avslutat, men viss rapportering släpar fortfarande efter. Ett sista avslutande seminarium kommer att hållas sommaren 2012 i Aix-en-Provence.

[4] Accident Source Term Evalutation Code.
[5] European Review Meeting on Severe Accident Research.

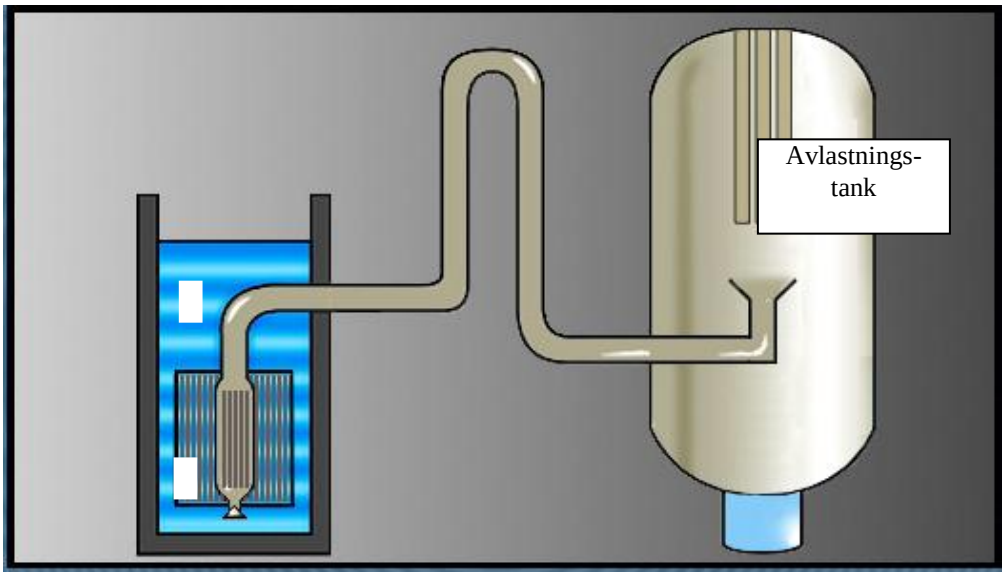

Figur 2.3.1. En förenklad skiss av PHEBUS-anläggningen med drivande reaktor, testsektion och en simulerad PWR-krets med ånggenerator och inneslutning (anläggningen nedskalad 1:5000).

Programmet omfattade ursprungligen sex experiment vilka betecknas FPT0-5, (FPT = Fission Product Test), se tabell 2.3.1. FPT0, FPT1, FPT4, FPT2 och FPT3 genomfördes under åren 1993, 1996, 1999, 2000 och 2004, medan det 5:e experimentet ströks. Ursprungligen planerade man att utföra ett experiment per år. Det visade sig dock snart att nedmontering och dekontaminering efter varje experiment, samt uppsättning av utrustningen för nästa experiment, var svårare och mer tidskrävande än man antagit. Kraven på säkerhet, arbetsmiljö och strålskydd har dessutom höjts från år till år. Kostnaderna för de fem experiment som utförts uppskattas till drygt 2 miljarder kronor. Frankrike står för 60 procent och EU för 25 procent. Resten fördelas mellan de andra deltagande länderna.

Experiment FPT4 skiljde sig från övriga genom att utgångsgeometrin motsvarade en bädd av bränslerester. Det första experimentet skulle använda färskt bränsle medan nr 2, 4 och 5 skulle återanvända utbränt bränsle från någon lämplig reaktor. Av detta material tillverkades stavar (en partikelbädd för FPT4) med en längd som passade till Phebus-reaktorns experimentkanal. Ett par speciella stavar med inbyggda termoelement som skulle mäta temperturförloppet i bränsleknippet under experimentet ingick i samtliga bränsleknippen. För att orientera läsaren om programmet i sin helhet sammanfattas testmatrisen i tabell 2.3.1.

En förenklad skiss av PHEBUS-uppställningen visas i figur 2.3.1. Anläggningen består i huvudsak av en drivande kärnreaktor, en testsektion, en anslutande yttre krets, en inneslutningstank, samt en avlastningstank. Den drivande reaktorn används först för att återskapa kortlivade klyvningsprodukter i bränslet under normal kylning vid full effekt, samt därefter för att upphetta den nu okylda testsektionen tills dess att bränslet i den relokerar och smälter. Testsektionen består av ett bränsleknippe omgivet av ett keramiskt säkerhetshölje av toriumdioxid (innerst) och zirkoniumdioxid (ytterst). Ett typiskt bränsleknippe består av ca 18 bränslestavar och en central styrstav i en axiellt rotationssymmetrisk geometri. Den yttre kretsen skall simulera

en del av primärkretsen hos en PWR med varma benet och ånggenerator, samt reaktorinneslutning.

Tabell 2.3.1: Aktuell testmatris för utförda PHEBUS-experiment.

Experiment	Typ av bränsle	Bränsle	Primärkrets	Inneslutning
FPT0 År 1993	Färskt bränsle i oxiderande miljö	Smältning <20% Bränsle-degradering	FP retention i primärkrets. ÅG med het sekundärsida.	Aerosol-fenomen Jodkemi vid pH 5
FPT1 År 1996	Använt bränsle i oxiderande miljö	Som FPT0	Som FPT0	Som FPT0
FPT4 År 1999	”Debris bed”	Total nedsmältning	Ingen (filter)	Ingen
FPT2 År 2000	Använt bränsle i reducerande miljö	Som FPT0 In-sprutning av borsyra	Som FPT0	Som FPT0 men med pH 9
FPT3 År 2004	Använt bränsle med styrstavs-material av B_4C	Max ca 1 kg relokerat bränsle	Som FPT0	Som FPT0 men med pH 9 och rekombinatorer

För att simulera inverkan av styrstavar på smältförloppet ingick en centralt placerad styrstav med ytterhölje i bränsleknippet. Geometrin ges av figur 2.3.2.

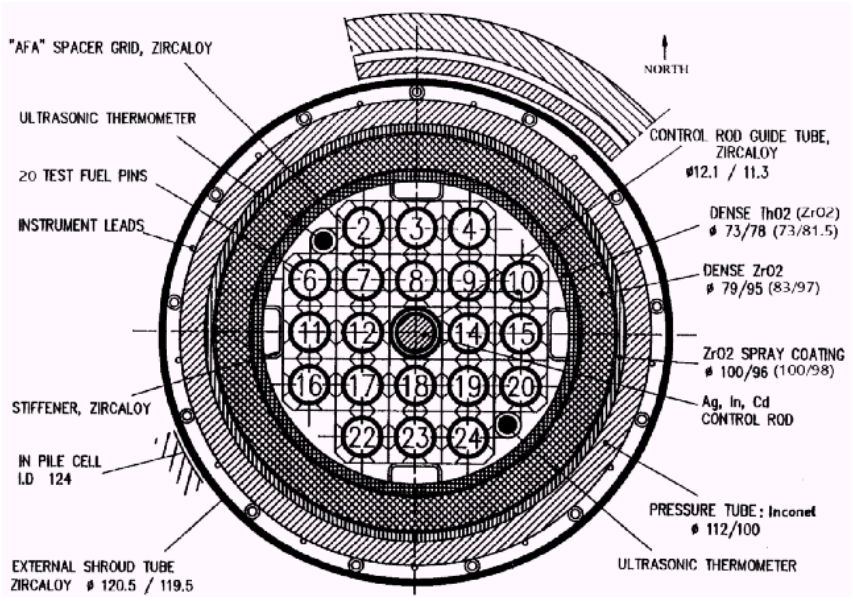

Figur 2.3.2. Tvärsnitt genom försökskanalen med monterat bränsleknippe.

Styrstavarna i FPT0, -1, och -2 var av den typ och geometri som normalt används i tryckvattenreaktorer (PWR), dvs. baserade på en silver-indium-kadmiumlegering (SIC). I försöket FPT3 användes en styrstav som innehöll sintrade stavar av borkarbid (B_4C). Valet av styrstavsmaterial visade sig sedan ha en stor betydelse för jodkemin under och efter härdsmältningen. Orsaken var att silver (och i viss mån

även de andra två metallerna i SIC) förångades, bildade aerosol, reagerade med elementär jod och eventuellt bildade silverjodid. Avgivet silver från styrstaven dominerar kraftigt i mängd över joden i bränslet. I ett senare stadium av haverisekvensen var därför nästan all jod bunden som silverjodid. Någon liknande dramatisk inverkan på jodkemin hade inte borkarbiden i FPT3.

Ett experiment börjar med att det kylda testknippet bestrålas med högt neutronflöde under några veckor för att uppnå jämviktshalter av mera kortlivade radionuklider. Det egentliga experimentet startas sedan genom att det utgående kylflödet från testkanalen omlänkas till den simulerade PWR-kretsen, ingående kylflöde stryps samtidigt som reaktoreffekten sänks kraftigt. Reaktoreffekten ökas sedan åter i steg tills provknippet börjar relokera eller smälta. Experimentet stoppas genom att reaktorn slås av och knippet kyls med inert gas. Detta görs av både praktiska och säkerhetsmässiga skäl eftersom provet kan förstöras vid återflödning med vatten. Man vill vidare inte ha för mycket smälta eftersom detta skulle kunna leda till en reaktion mellan smälta och skyddshölje eller ett dränage av smälta till den nedersta delen av testsektionen.

Möjligheten att följa experiment under själva utförandet med direkta observationer och mätningar är ytterst begränsad. Temperaturen i bränsleknippet blir så hög att stora delar av instrumenteringen i detta smälter, förångas eller reagerar kemiskt med närvarande gaser. Eftersom skyddshöljet är termiskt kopplat till bränsleknippet, kan man genom att mäta temperaturen på olika ställen i höljet få indirekt information om temperaturen i knippet. Genom tvådimensionella beräkningar fastställs i förväg vilka uppmätta temperaturer på olika platser i skyddshöljet som motsvarar önskade temperaturer i bränsleknippet och vilka mätvärden som skall leda till reaktoravstängning. Dessutom finns speciella mätdon i skyddshöljet som skall reagera på eventuell smältning av höljets inre del och utlösa omedelbar reaktoravstängning.

Förutom temperaturmätningar och gammaspektroskopi erhålls de flesta resultaten från experimenten genom analys av tagna stickprover och genom olika typer av undersökningar som görs i efterhand. Ultraljudtermometrar med mätkroppar av sintrad toriumoxid (smältpunkt ca 3220 ^{o}C) monterade i bränslet har använts i de senare experimenten för att utöka mätområdet. Speciellt studeras tagna gas- och aerosolprov, deponering av material på olika ytor, sammansättning av vattenlösningen i sumpen och återstoden av bränsleknippet, se figur 2.3.2.

Experimenten motsvarar närmast haverier med utebliven reaktoravstängning eftersom kortlivade fissionsprodukter nybildas i stigande fart under hela förloppet fram till reaktorsnabbstopp. Under t.ex. FPT3 ökades effekten hos den drivande reaktorn från ca 0.38 MW, när de första kapslingsbrotten observerades, upp till ca 4.6 MW vid experimentets slut. I stora drag följer neutronflödet genom bränsleknippet denna effekt och därigenom stiger även fissionsraten kraftigt. Detta bör man ha i åtanke vid jämförelse av resultaten från PHEBUS med verkliga tänkbara reaktorhaverier. I de flesta tänkbara haverifall är det ju resteffekten som leder till uppvärmning medan fissionsraten är låg.

Experimenten genomfördes i en serie faser med olika avsikt. Punkterna 1-4 var gemensamma för alla experimenten. Punkterna 6-10 användes vid stavformat bränsle och 11-13 för partikelbädden:

1. Förbestrålning av bränslet under några veckor med vattenkylning för att återskapa kortlivade nuklider.
2. Kalibrering av effekten från reaktorns neutronflöde på knippets energiproduktion under fortsatt vattenkylning.
3. Nedgång till låg reaktoreffekt, stängning av vattenkylningen och ersättning med ett flöde av den ånga plus gas som skulle användas under experimentet.
4. Stegvis ökning av reaktoreffekten till en nivå där bränsle smälter och relokerar.
5. För experiment med bränsle i stavform skedde sedan följande
6. Snabbstopp av reaktorn och stängning av gas/ång-tillförseln till experimentkanalen. Detta inleder ett förlopp där aerosolernas uppträdande i ånggeneratortuben och inneslutningen studeras i ett nästan stagnant system.
7. Stängning av förbindelsen mellan ångenerator och inneslutning. Detta stadium användes för att studera kemin i inneslutningen efter härdsmälta.
8. Sprayning av inneslutningen med återcirkulerat vatten från dess sump för att studera uppträdandet av deponerat material, bla jod.
9. Slutlig nedkylning av experimentkanalen med ånga och kvävgas som sedan ej leds till ånggenerator och inneslutning utan direkt till en avfallstank.
10. Demontering av experimentkanalen, tomografi på denna, ingjutning av bränsleknippet och slutligen en snittning av kanalen på utvalda ställen.
11. För bränsle som partikelbädd användes inte den simulerade ånggeneratorn och inneslutningen. I stället utnyttjades en serie filter och gasen efter dessa fick sedan passera direkt till anfallsbehållaren. Dessa filter var placerade dels i överdelen av experimentkanalen och dels något senare innan gasen leddes till avfallstanken.
12. Slutlig nedkylning av experimentkanalen med ånga och kvävgas som sedan ej leds till ånggenerator och inneslutning utan direkt till en avfallstank.
13. Demontering av experimentkanalen, tomografi på denna, ingjutning av bäddresten och slutligen en snittning av kanalen på utvalda ställen.

I samtliga fall stabiliserades bränsleåtersoden genom ingjutning i epoxyplast eller woods metall. Epoxyplast fungerade bra, men visade sig bilda mindre mängder vätgas genom radiolys. Woods metall, som användes i FPT3 (på grund av vätgasrisken), fungerade dåligt då dess täthet och ytspänning gav en ofullständig fyllning av knippet. Den stora densiteten ledde dessutom till att bränslerester och annat löst material flöt upp vid ingjutningen.

Förutom transmissiontomografi med högenergiröntgen utfördes tomografiska mätningar med högupplösande gammaspektroskopi. Dessa mätningar korrigerades sedan med absorptionsfaktorer beräknade ur röntgentomografin. Härigenom kunde den geometriska fördelningen av ett flertal grundämnen bestämmas med mm-upplösning som funktion av radie och höjd.

Resultaten från röntgentomografin ges i figur 2.3.3, som är färgkodad så att svart är tomrum, blått är lägst densitet och rött högst densitet.

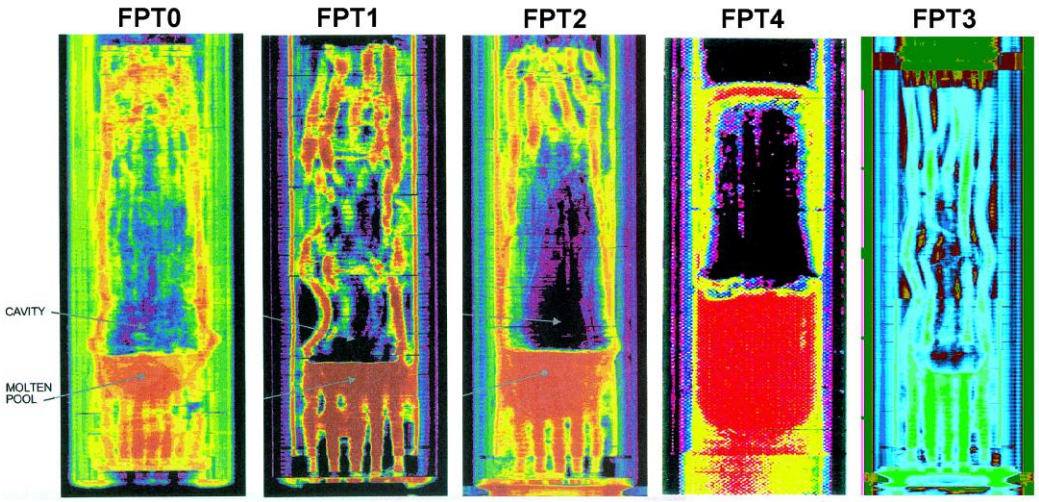

Figur 2.3.3. Tomografiskt tvärsnitt genombränslekanalen efter de olika experimenten. Täthetem har åskådliggjorts med hjälp av en färgskala, som tyvärr ändrats för FPT3. I samtliga fall ser man hur en betydande mängd bränsle relokerat till bränslekanalens botten vilket lett till bildning av överliggande hålrum.

Det är svårt att beskriva allt vi lärt oss från ett 20-årigt projekt på några sidor varför följande sammanställning måste bli mycket summarisk. Några viktiga observationer och lärdomar från Phebus-FP experimenten kan dock sammanfattas i följande uppställning.

2.3.1. Bränslet

- Nedsmältning och relokering sker tidigare än vad som de flesta koder predikterat före dessa experiment.
- Överhettningen leder till bildning av hålrum i centrum av bränsleknippet.
- Smält bränsle bildar en vätskepöl, som sedan delvis dränerar nedåt.
- Materialet i styrstaven verkar påverka smältförloppet.

2.3.2. Källtermen

- Inga tecken på att cesiumjodid bildas i större mängd.
- Beräkningar antyder att t ex Cs_2MoO_4 (cesiummolybdat) bildats och minskat tillgängligheten av cesium för bildning av cesiumjodid.
- Silver från styrstaven utgjorde en betydande andel av frigjort material, band jod och ledde till en liten halt gasformig jod.
- Borkarbid gav endast en liten produktion av metan och organiska jodider, men en betydande mängd elementär jod.
- Förångning av U och Pu var mycket mindre än väntat.
- Transport av jod i primärsystemet var ca 1/3 som gas, men mer i FPT3

2.3.3. Aerosoler

- Partiklar har en ”lök”-struktur och agglomererar sedan till större enheter.

- De flesta partiklarna har en kärna av t.ex silver.
- Partiklarnas AMD[6] tycks variera med plats, tid och flöde, men många mätningar on-line har misslyckats.
- En stor mängd aerosoler har nästan alltid deponerat i ånggeneratorns varma ben.
- Sedimentation är dominant för avskiljning i inneslutningen medan diffusiofores är viktig vid ångkondensation på kalla ytor.
- Numerisk modellering av gasens strömning visar att denna i vertikalled på vissa platser överskrider aerosolens fallhastighet.

2.3.4. Inneslutningskemi

- Jod och andra nuklider deponerar initialt på inneslutningens väggar.
- Nästan all deponerad jod tvättas ned till sumpen vid sprayning av inneslutningens väggar.
- Det mesta av joden hamnar i sumpen som delvis löst och delvis sediment.
- Inneslutningens gasfas innehåller efter en tid bara en liten mängd jod såväl i som utan närvaro av silver från SIC.

2.3.5. Kodjämförelser

- Samtliga testade koder har uppenbarligen modifierats under hand - i större eller mindre grad - med ledning av resultaten från Phebus-FP. Oklart om detta alltid har relevans för verkliga härdhaverier eller om det gör koden specifik för Phebus-FP.
- Ingen kod verkar ha kunnat ge samma resultat i alla avseenden som experimenten. Man behöver nu definiera ett användbart mått på hur bra en kod beskriver experimentens data i sin helhet - även med hänsyn till experimentella osäkerheter.
- Massövergångstal har uppmätts i den inaktiva kopian av Phebus-inneslutningen och sedan använts vid olika beräkningar.
- Vid beräkningarna på Phebus-FP försöken användes en betydande mängd mätdata, bla för termodynamiken, som troligen kommer att saknas när en postulerad härdsmälta i en riktig reaktor skall modelleras före eller under ett haveri.

Ett flertal observerade kemirelaterade frågeställningar återstår efter Phebus-FP. För att studera dessa, och även för att behålla viss kritisk personal, startades ett uppföljande projekt. Detta kallades för International Source Term Project (ISTP). Resterande medel från EU, som inte kom till användning för det inställda experimentet FPT5, har delvis finansierat ISTP. Trots att Sverige inte deltagit direkt som finansiär av ISTP har vi ändå kunnat ta del av erhållna resultat genom att projektet delfinansierats av EU. Även ISTP har nu avslutats. En kort redogörelse för detta och några betydelsefulla resultat ges nedan.

---

[6] AMD = Aeordynamical Mean Diameter. Storleks- och formberoende parameter.

2.3.6. ISTP-Mät och analysprogram

Trots att Sverige inte deltagit direkt som finansiär av ISTP har vi ändå kunnat ta del av erhållna resultat genom att det delfinansierats av EU. ISTP har nu avlsutats.

ISTP-projektet har i princip studerat följande frågeställningar:

- Kemi vid höga temperaturer varvid jämvikts- och hastighetskonstanter bestäms. Aktuella grundämnen har i första hand varit H, O, Mo, Cs och I.
- Reaktion av kapslingsmaterial vid hög temperatur med strömmande ånga, vätgas, kvävgas och luft. Kvävgasen har en klar inverkan på oxidationsförloppet genom att bildad nitrid sedan oxiderar, se figur 2.3.4, och leder till lossnande ytskikt.
- Reaktion mellan borkarbid och ånga - särskild bildning av oxider och metan (BECARRE).
- Reaktion mellan borkarbid och rostfritt stål eller zircaloy (BECARRE).
- Oxidation med vattenånga av den smälta som bildas vid reaktion mellan borkarbid och järn. Figur 2.3.5 visar hur bildad gas bubblar genom smältan av boroxider.
- Radiolys av jod och cesiumjodid i några olika miljöer och på olika ytor med gammastrålning från ^{60}Co.

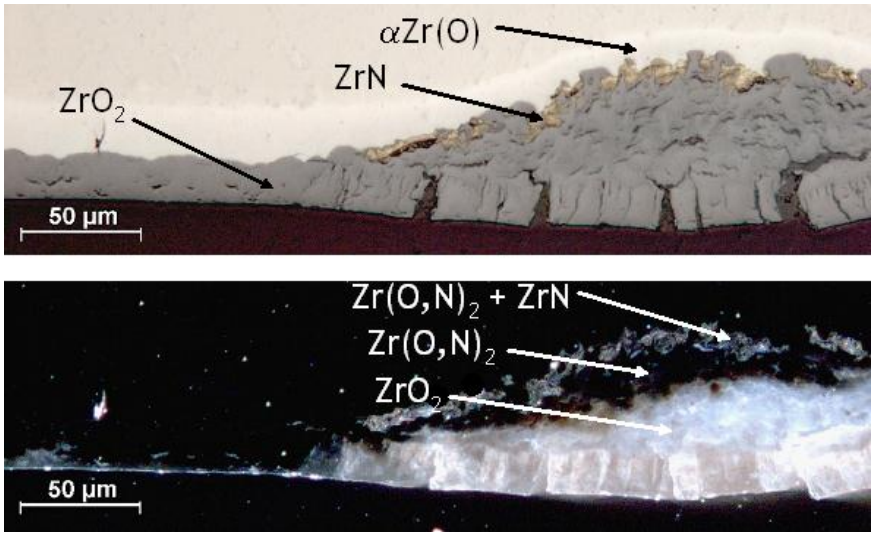

Figur 2.3.4. Reaktionsprodukter mellan zircaloy och luft (MOZART).

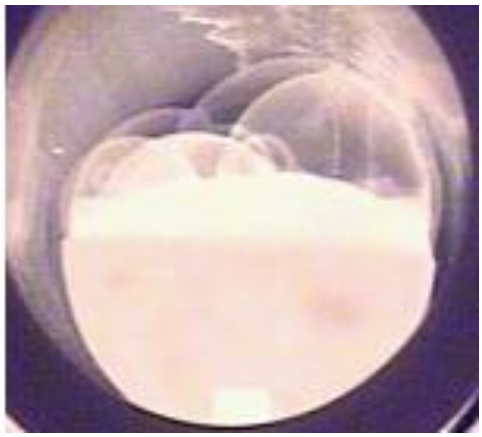

Figur 2.3.5. Bildning av gasbubblor vid oxidation av B_4C-SS-Smälta med ånga.

För svenskt vidkommande är resultaten från experimenten med borkarbid av särskilt intresse. Som tidigare observerats är reaktionen mellan B_4C och rostfritt stål eller zircaloy snabb och leder till en smälta. Denna oxideras i vattenånga varvid gasformiga produkter bildas. Då uppträder ett lager av smälta boroxider på underlagets yta, bubblar och hindrar delvis oxidationen. En stor del av kolet i smältan oxideras av ångan till kolmonoxid eller koldioxid. Endast lite metan har observerats vid dessa försök. Troligen kommer även resultaten från ISTP-projektet att presenteras vid Phebus-FP-seminariet i Aix-en-Provence sommaren 2012.

Vidare kan noteras att vissa resultat från PHEBUS har beaktats i beräkningskoder, exempelvis genom att bildning av cesiummolybdat modelleras i MAAP5.

2.4 MCCI 2 – Växelverkan mellan härdsmälta och betong

Projektet MCCI (Molten Core Concrete Interaction) har genomförts i två etapper. Etapp 1 (MCCI 1) genomfördes på Argonne National Laboratory (ANL) från januari 2002 till december 2005. Etapp 2 (MCCI 2) genomfördes under åren 2006 – 2009 och avslutades med ett slutseminarium som hölls i Cadarache i november 2010. Syftet med MCCI-projektet har varit att studera hur en smält härd reagerar med betong och hur den kan kylas med vatten ovanifrån.

Studier av fenomen relaterade till reaktioner mellan smälta och betong inleddes efter TMI och genomfördes i ACE experimenten, utförda vid ANL. Kylbarhet av smältan började studeras i det påföljande MACE-projeket. MCCI är fortsättning på dessa projekt. Totalt har 21 experiment inom MCCI-projektet genomförts varav 10 inom MCCI 2. Tidigare hade omkring 20 liknade experiment utförts inom projekten ACE och MACE.

I MCCI har experiment genomförts i två olika uppställningar:

- I en experimentuppställning kallad SSWICS (Small Scale Water Ingression and Crust Strength) etableras en smälta och kylning av denna studeras om den kyls genom att pumpa in vatten över smältan (”top flooding”). Härvid studeras kylmekanismer, krustabildning, krustans egenskaper, mm. Hur kylbarheten påverkas genom att pumpa in gas och/eller vatten från botten har också studerats.

- I en uppställning kallad CCI (Core Concrete Interaction) skapas en smälta och smälta-betongreaktioner studeras. Även i dessa experiment pumpas vatten in ovanpå smältan några timmar efter det att betong-smälta reaktioner har kommit igång.

2.4.1. Experiment i MCCI 2

Syftet med MCCI 2 har varit att komplettera tidigare resultat genom att:

- ytterligare undersöka kylmekanismer på en smälta om den kyls genom att hälla på vatten (top flooding),
- undersöka återstående osäkerheter i betong-smälta reaktioner i två dimensioner (axiellt/radiellt),
- verifiera konstruktionslösningar i härdfångare i nya reaktorer.

Experimenten har varit indelade i fyra kategorier:

1. Kombinerade experiment för att undersöka samspelet mellan olika kylmekanismer som ger data för modell- och kodutveckling,
2. Experiment för att undersöka nya konstruktioner utvecklade för att öka kylbarheten,
3. Experiment för att generera tvådimensionella data för betong-smälta reaktioner,
4. Integrala experiment för att validera koder för svåra haverier.

Inom kategori 1 utfördes 4 experiment, SSWICS 8 till 11. Experimenten bekräftade de mätningar av krustans hållfasthet som gjordes i tidigare experiment. Det demonstrerades också att gasbildningen vid betong-smälta reaktioner ökar vatteninträngningen och kylningen i krustan.

Två småskaliga experiment, SSWICS-12 och 13 samt ett storskaligt experiment, WCB-1 genomfördes i kategori 2. I dessa experiment erhölls data om hur vattentryck och gasinblandning påverkar kylningen av smältan då vatten tillförs underifrån. Vidare demonstrerades hur kylning av smältan sker genom en vattenkyld stålplatta.

I kategori 3 genomfördes två experiment, CCI-4, CCI-5. Data för hur långsiktiga betong-smältareaktionen påverkas av olika sammansättningar av smältan erhölls. Dessa experiment visade också att storleken på experimentuppställningen inte påverkar effektens fördelning axiellt/radiellt för kiselbaserad betong.

I kategori 4 genomfördes ett experiment, CCI-6. Här visades att tidig flödning med vatten ovanifrån ökar kylbarheten signifikant även för kiselbaserad betong och att gaseruptioner är en betydande kylmekanism.

2.4.2. Fenomenologi och modellutveckling

Omfattande arbeten med utveckling av koder och modeller har genomförts baserade på data från MCCI-projekten. Som exempel kan nämnas:

- Argonne utvecklar koden COREQUENCH. Denna kod inkluderar de kylmekanismer som observeras i experimenten: eruption i smältan, vatteninträngning, krustans tillväxt och förankring i väggen samt modeller för betongablation.
- University of Wisconsin utvecklar modeller för värmetransport vid eruption i smältan och vatteninträngning.
- GRS gör CFD-beräkningar för att studera egenkonvektion i närvaro av temperaturberoende materialegenskaper och ojämn uppvärmning.
- JNES (Japan Nuclear Energy Safety Organization) gör beräkningar med COCO-koden och GRS gör beräkningar med MEDICIS-koden. IRSN använder ASTEC/MEDICIS.

2.4.3. Sammanfattning och slutsatser

Arbetet som genomförts inom MCCI-2 presenterades och diskuterades på det avslutande seminariet i november 2010 i Cadarache. Resultatet av detta seminarium blev följande stycken om vad som uppnåtts, vad som fattas och förslag till fortsättning:

I OECD-MCCI-1/2 programmen har värdefulla data och kunskaper erhållits om MCCI-fenomen framför allt betong-smälta reaktioner och smältans kylning. Tillräckliga data finns om krustans hållfasthet och förankring, olika betongtypers inverkan på betong smälta reaktioner och vatteninträngning uppifrån.

Begränsade data finns och frågor finns om fördelen med tidig vattenflödning, kylning av smältan underifrån och vatteninpumpning från botten.

För att hantera kvarvarande frågor görs följande rekommendationer:

- Färdigställ en state-of-the-art rapport om smältans kylbarhet och betong-smälta reaktioner som återger de senaste trettio årens forskningsresultat.
- Ta fram ett internationellt standardproblem (ISP[7]) inklusive en storskalig blindtest för att utvärdera beräkningkoder rörande betong-smälta-reaktioner. Testen kan utföras så att ytterligare data om tidig flödning erhålls.

Det noteras också att ANL:s experimentanläggningar är unika i att utföra storskaliga MCCI-experiment. Det noteras vidare att experimentuppställningarna är främst tillämpliga för anläggningar med ”dry cavity” (haveristrategi där smältan inte faller i vatten). För svenska förhållanden har resultaten därför varit av begränsat intresse.

Det finns i dagsläget inga beslut om att fortsätta MCCI-projektet vilket kan leda till att anläggningen kan läggas ner.

2.5 SERENA – Ångexplosioner i reaktorinneslutningen

Under januari 2002 startades ett OECD/NEA-projekt kallat SERENA – Steam Explosion REsolution for Nuclear Applications. Det övergripande målet med SERENA var att få en tillräckligt bra förståelse för ångexplosioner för att kunna

[7] Experimentresultat som används för att validera beräkningskoder och administreras av OECD/NEA.

göra riskbedömningar av reaktoranläggningar. När projektet avslutades i december 2005 kunde man konkludera dels att reaktortanken skulle motstå postulerade ”in-vessel” ångexplosioner, dels att ”in-vessel” ångexplosioner inte utgör något hot mot inneslutningens integritet. Beträffande ”ex-vessel” explosioner var slutsatsen att det inte gick att utesluta att en ångexplosion skulle kunna hota inneslutningens integritet.

Ett annat problem var att olika datamodeller som beräknar förloppen vid ångexplosioner, gav mycket stor spridning i resultaten. Detta kunde tyda på att det finns brister i förståelsen av fenomen relaterade till ångexplosioner i reaktorinneslutningen.

Utvärderingen av resultaten från SERENA-projektet ledde till en rekommendation för fortsatt forskning med syfte att minska osäkerheter och därigenom uppnå större tillförlitlighet i beräkningar av säkerhetsmarginalerna, i synnerhet vad gäller inneslutningsbelastningar.

2.5.1. SERENA 2 – Fortsättningen av SERENA

Fas 2 av SERENA-projektet startade i oktober 2007 och 11 länder deltar. Syftet med fas 2 av projektet är att bringa klarhet i ångexplosionsfenomen för prototypiska smältor genom att genomföra ett begränsat antal väl designade experiment med avancerad mätutrustning.

Ett annat syfte är att tillhandahålla experimentella data för vidareutveckling och validering av ångexplosionskoder. Som stöd till den experimentella delen finns en grupp vars uppdrag är att genomföra för- och efterberäkningar med olika koder samt beräkningar för realistiska haveriscenarier.

En serie med sex kompletterande tester vardera i TROI och KROTOS ingår i SERENA 2, dvs. totalt 12 tester. Grundkompositionen är en eutektisk blandning av UO_2 och ZrO_2, dvs. 70% UO_2 och 30% ZrO_2, eftersom tidigare TROI-experiment visade att denna sammansättning kan ge spontana explosioner med större verkningsgrad än andra kompositioner. Andra kompositioner kommer att bestämmas senare. För att garantera att en explosion kommer att inträffa, används en trigger i alla tester.

I tabell 2.5.1 visas förslag till testmatris. Smältans temperatur kommer att ligga nära den temperatur som ges av realistiska bedömningar av haveriförloppet. Stark överhettning som i vissa tidigare TROI-experiment kommer att undvikas.

KAERI har genomfört alla sina experiment och man fick triggade explosioner i fem tester av sex. Ett test i KROTOS återstår och det är planerat till mars 2012. Ett resultat från SERENA 2 som är något överraskande är att kraftigast explosioner inträffade med 80 % UO_2-20 % ZrO_2 och inte med eutektisk sammansättning.

När det gäller den teoretiska aspekten och modelleringen av FCI i koder så finns det många delfenomen som är olika noggrant modellerade. En viktig fråga, som identifierades i det tidigare SERENA-projektet, gäller voidproduktionen under ”premixing” och dess roll i det försatta förloppet.

Tabell 2.5.1: Testmatris för anläggningarna KROTOS och TROI inom SERENA-projektet samt status för olika experiment.

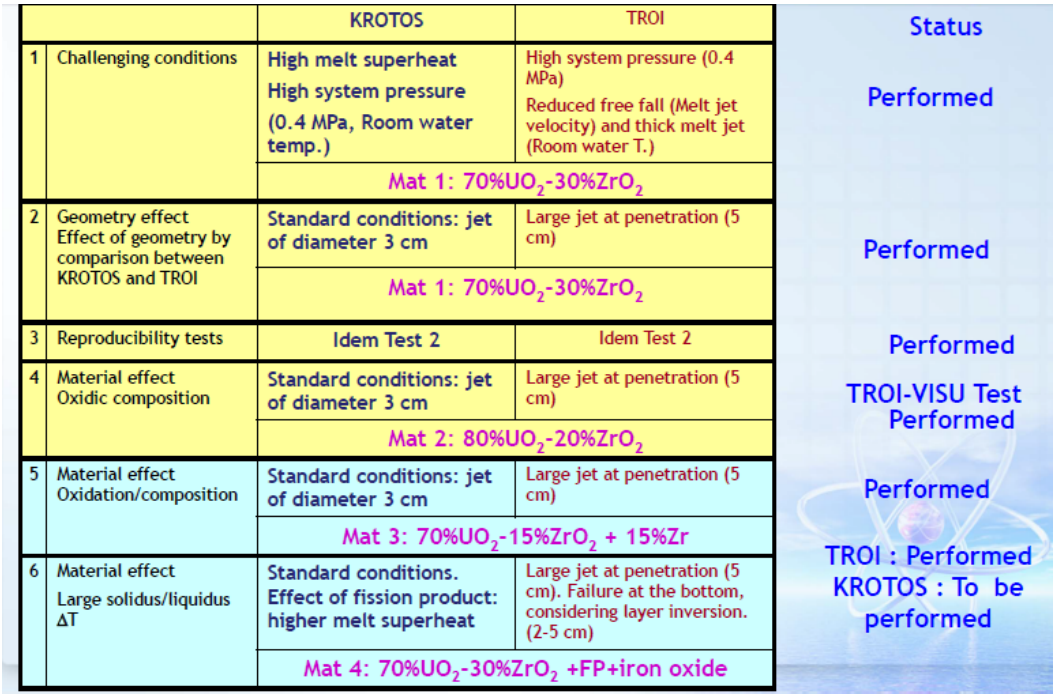

		KROTOS	TROI	Status
1	Challenging conditions	High melt superheat High system pressure (0.4 MPa, Room water temp.)	High system pressure (0.4 MPa) Reduced free fall (Melt jet velocity) and thick melt jet (Room water T.)	Performed
		Mat 1: 70%UO_2-30%ZrO_2		
2	Geometry effect Effect of geometry by comparison between KROTOS and TROI	Standard conditions: jet of diameter 3 cm	Large jet at penetration (5 cm)	Performed
		Mat 1: 70%UO_2-30%ZrO_2		
3	Reproducibility tests	Idem Test 2	Idem Test 2	Performed
4	Material effect Oxidic composition	Standard conditions: jet of diameter 3 cm	Large jet at penetration (5 cm)	TROI-VISU Test Performed
		Mat 2: 80%UO_2-20%ZrO_2		
5	Material effect Oxidation/composition	Standard conditions: jet of diameter 3 cm	Large jet at penetration (5 cm)	Performed
		Mat 3: 70%UO_2-15%ZrO_2 + 15%Zr		
6	Material effect Large solidus/liquidus ΔT	Standard conditions. Effect of fission product: higher melt superheat	Large jet at penetration (5 cm). Failure at the bottom, considering layer inversion. (2-5 cm)	TROI : Performed KROTOS : To be performed
		Mat 4: 70%UO_2-30%ZrO_2 +FP+iron oxide		

I Analytical Working Group pågår beräkningar med olika ångexplosionskoder som har utvecklats baserat på den kunskap som har erhållits. Förhoppningen är att spridningen mellan koderna blir mindre än tidigare noterat i första fasen av SERENA.

SERENA 2-projektet kommer att sammanfattas i en rapport som beskriver alla experiment i TROI och KROTOS samt redovisar analyserna och resultaten. Vidare kommer beräkningsresultaten med ångexplosionskoder att redovisas samt slutsatser från hela projektet att dras. Ett slutseminarium planeras till 13 – 15 november 2012.

2.6 BIP – Behaviour of Iodine Project

Although the understanding of iodine behaviour in the containment has advanced significantly in the past decades there is still a considerable work to be made on the understanding of the detailed mechanisms and thus also about the prevention of possible releases during a severe accident. Hence, further studies in an international context are warranted.

As a result of this, the Nuclear Energy Agency (NEA) Committee for the Safety of Nuclear Installations (CSNI) initiated the Behaviour of Iodine Project (BIP) with AECL as the operating agent. The project officially started in July 2007 and should have ended in June 2010, but it was prolonged several extra months in order to perform some more tests and to complete the documentation. The members included Belgium, Canada, Finland, France, Germany, Japan, Korea, the Netherlands, Spain, Switzerland, Sweden, the United Kingdom and the United States. The total budget of the project was about 1.5 million Canadian dollars, half of which was contributed

by Canada. The project reports will be available to non-participants in September 2013.

This three-year program had three research areas, each of which will be summarized in the following sections:

1. Iodine deposition onto surfaces,

2. Organic iodide formation from irradiated surfaces,

3. Radioiodine Test Facility experiments.

2.6.1. Iodine Deposition onto Surfaces

The OECD Status Report on Iodine Behaviour highlighted uncertainties that still exist regarding the adsorption of iodine on containment surfaces, the speciation of sorbed iodine, the potential for its revolatilisation, and the ease of decontamination of surfaces. It also noted that iodine deposition on surfaces as a function of temperature and relative humidity (including condensing conditions) has not been established rigorously.

Previous studies at AECL (Atomic Energy of Canada Limited) have determined that the rate of adsorption of gaseous iodine on organic paints, stainless steel, carbon steel, zinc primer paint and aluminium are strongly dependent upon the temperature and relative humidity of the air stream containing iodine as well as on the nature of the carrier gas (e.g., desorption from stainless steel is dependent upon the oxygen concentration) and the rate of mass transfer to the surface. Most iodine codes do not capture these effects because there is not sufficient understanding regarding the conditions under which adsorption of iodine on surfaces occurs, and what conditions are necessary to initiate adsorption and corrosion. The BIP tests provide data from which kinetic parameters, such as deposition velocity can be derived for the various surfaces found in containment. The main parameters adjusted were surface type (including steel samples), temperature and relative humidity.

In addition to measurements of iodine adsorption in the gas phase, some tests were performed to study the deposition of aqueous I_2 (or I^-) onto various containment surfaces. In addition to paint, insulation and some corrosion product material (aluminium hydroxide and iron oxide) were also tested for affinity for iodine.

These sorption measurements can be used to develop a model for iodine adsorption onto (and desorption from) surfaces which can be incorporated in iodine behaviour codes.

2.6.2. Organic Iodide Formation from Irradiated Surfaces

The formation of organic iodides in post accident containment could result from gas or aqueous phase homogeneous processes, or from processes initiated at the surfaces of containment paints.

Although there are some data available on the production of organic iodides from painted surfaces, a systematic study was warranted. The need for additional data on

organic iodide production was also highlighted in the OECD sponsored Status Report on Iodine behaviour.

BIP experiments studied the rate of organic iodide production by monitoring the concentration of methyl iodide in the vessel during irradiation. In addition to studying the effect of different epoxy paints (epoxy was chosen because it is one of the most common containment paint types), one of the main goals of the project was to demonstrate that organic iodide production depends upon the amount of water that is co-adsorbed. Therefore, in addition to paint type (age and treatment), the main experimental parameters included various methods of altering the surface water loading (aqueous or gas loading, with or without pre-soaking in water).

Any methyl iodide produced is subjected to continuous irradiation. As such, the radiolytic degradation rate of gas phase methyl iodide is also important and was determined at the conditions of the BIP tests (dose rate, concentration, etc.). The experiments quantified the overall (or steady-state) rate of production of organic iodide.

These experiments are complementary to those performed within IRSN's EPICUR facility. The EPICUR experiments provide information regarding the rate of production of organic iodides, but do not give information about its destruction. The combination of the two experimental programmes provides a comprehensive view of organic formation.

2.6.3. Radioiodine Test Facility Experiments

The time-dependent concentration of airborne radioiodine in reactor containment is an important parameter used to evaluate the radiological impact of a reactor accident. Predicting this concentration is not a straightforward problem because a number of complex kinetic phenomena must be considered. The RTF (Radioiodine Test Facility) was built at AECLs Whiteshell Laboratories (WL) to study these phenomena by reproducing many of the features of a reactor containment building, and simulating postulated reactor accident conditions. In the RTF, the effects of a variety of parameters on the volatility of iodine could be examined, separately, or in combination. These included the presence of a radiation field, the temperature of the gas and aqueous phases and surfaces, the circulation of the gas and aqueous phases, venting of the gas phase, the influence of surface treatments and coatings, the effect of addition of various chemicals, the pH, and the presence of condensing conditions.

The RTF was designed and built starting in 1986 and was commissioned in 1988. The last test was performed in November 1998, and the facility was decommissioned in the following years.

BIP members selected the results from 5 tests to be released in the BIP program, where the main focus was on organic paints and impurities. The tests demonstrate the dissolution of residual paint solvents and their subsequent radiolytic degradation and formation of organic iodides. The tests also demonstrate the relative importance of various iodine sinks. The RTF data will help members develop and validate computer models.

2.6.4. Conclusions

Although good progress was achieved regarding the understanding of the formation of methyliodide from irradiated paint, the mechanism is not understood. A mechanistic understanding, applied to models for these phenomena, will improve our ability to explain results to our regulatory agencies, and justify application of these results to ranges outside of the tested conditions (e.g., extrapolation to wider selection of materials and to larger scale experiments and containment conditions). A more detailed mechanistic understanding of the formation of methyl iodide from irradiated paint is the goal of the continuation project – BIP2.

3. KTH RESEARCH ON SEVERE ACCIDENTS

3.1 Research Goals, Approach and Activities

The ultimate goal of the ongoing severe accident (SA) research at KTH is to help resolve two long-standing severe accident issues (i.e., ex-vessel debris coolability and steam explosion) in the Nordic BWR plants that employ cavity flooding as the cornerstone of severe accident management (SAM) to avoid ex-vessel molten corium concrete interaction (MCCI) which may threaten containment integrity. It is based on assumption that a coolable porous debris bed will be formed on the basemat in case of melt ejection into the deep water pool in the cavity following reactor pressure vessel (RPV) failure (see Figure 3.1). This SAM measure, however, increases the risk of steam explosion, while the efficacy of debris coolability still needs to be verified.

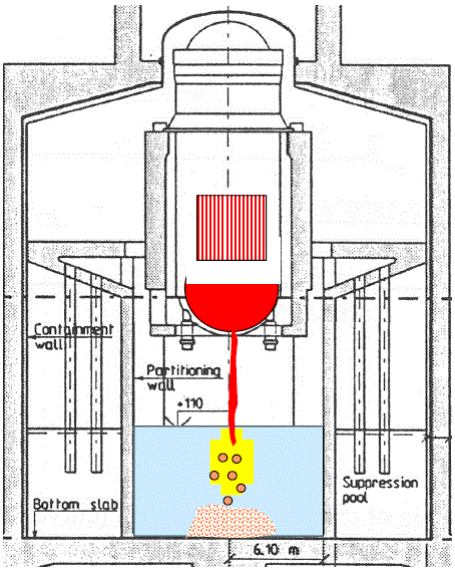

Figure 3.1: Severe accident management strategy in a Nordic BWR.

Started in APRI-6 (2006-2008) and continued in APRI-7 (2009-2011), the severe accident research at KTH was driven by the hypotheses that (i) corium melt discharge from the BWR vessel is gradual and in dripping mode that largely eliminates steam explosion risk and facilitates the formation of a well-fragmented debris bed, (ii) the characteristics (e.g., porosity, debris morphology) of the porous debris bed ensures debris coolability, even for a deep and/or stratified bed, and (iii) non-eutectic corium melt renders low conversion ratio in a steam explosion.

The APRI-7 activities at KTH were divided into four (subprojects):

- **INCOSAM (**IN-vessel COolability and Severe Accident Management);
- **DEFOR (**Debris in- and ex-vessel FORmation);
- **POMECO** (POrous MEdia in- and ex-vessel Coolability);
- **SERA (**Steam Explosion Risk Assessment);

and one international collaboration task **SAID (**Severe Accident Information Distillation from EU projects).

They are intended to establish the solid knowledge base (e.g., data, models, codes, methodologies and insights) to confirm the above hypotheses. The theme of the APRI-7 research remains "issue-resolution" and is directed by the risk-oriented approach (cf. Figure 3.2) which links the topical areas. This means that instead of addressing all scenarios and phenomena we concentrate our efforts on the limiting conditions and limiting mechanisms which are the bottlenecks in severe accident risks of Nordic BWRs.

The INCOSAM study was chosen in order to identify the limiting melt release conditions which are of importance to ex-vessel corium risk (debris coolability and steam explosion). The DEFOR study is to address the limiting mechanisms in debris bed formation, which govern the characteristics of debris beds, while the POMECO study is to assess the limits in coolability of the debris beds with the given prototypical characteristics. The SERA study is focused on opportunistic and fundamental aspects in the steam explosion energetics (conversion ratio), by addressing limiting conditions (melt release) and limiting physical mechanisms (low explosivity of corium), respectively. The idea of the opportunistic aspect is that if the melt is discharged in dripping mode, the risk of large-scale steam explosions is diminishing.

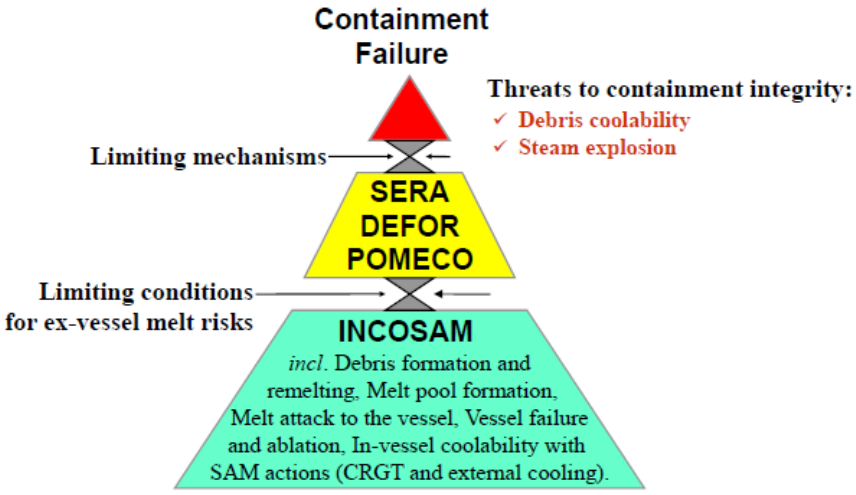

Figure 3.2: Risk-oriented approach and links between the topical areas.

The APRI-7 activities at KTH capitalize on the existing knowledge base of severe accident phenomena and scenarios, which was developed and obtained in the past national and international research programs. In particular, the APRI-7 research has synergetic collaboration with the ongoing projects EU SARNET2, OECD SERENA2 and US CSARP.

This report summarizes the key achievements in the topical areas. More detailed descriptions of the research activities can be found in the publications and technical presentations of project review meetings listed in the References.

3.2 In-Vessel Coolability (INCOSAM)

3.2.1. Motivation

The objective of the INCOSAM subproject is to quantify the vessel failure modes, timing, and the melt discharge characteristics. Ultimate success of the severe accident management (SAM) strategy in Nordic type Boiling Water Reactors (BWR) is contingent on effectiveness of ex-vessel melt coolability and absence of energetic steam explosion in a deep water pool located under the reactor vessel. When melt is ejected from the reactor pressure vessel, it is assumed that it will fragment, quench, and form a porous debris bed. But the resulting properties of the debris bed, that affect coolability of the bed [1] - [7], depend significantly on the mode of vessel failure (rupture size and location, characteristic time of melt release from the vessel, temperature and composition of the melt, amount of melt ejected at the first instant, etc.). The vessel failure mode also affects the potentials of steam explosion. In general, uncertainties in the ex-vessel melt behavior are largely due to uncertainties in the melt ejection characteristics which are determined by the phenomena of in-vessel stage of the accident and vessel failure. Therefore, in order to establish a firm basis that containment integrity can be preserved, it is necessary to reduce uncertainties in understanding the modes of vessel failure, which is the focus of this research.

3.2.2. Combined CRGT and External Vessel Cooling Efficiency for a BWR

The goal of this study is to clarify if coolant flow in Control Rod Guide Tubes (CRGT) and ex-vessel cooling of the vessel can aid in reducing uncertainties in the vessel failure mode of Nordic type BWRs. Timing of the accident progression and implementation of SAM measures is considered as a key factor in defining success of the in-vessel melt retention. Specifically, the focus of the study is to identify the mode and timing of vessel failure which will also set the time allotted for activation of external vessel cooling e.g., by pumping water into the deep reactor cavity up to the level of the vessel lower head.

We consider melt-vessel thermo-mechanical interaction in a hypothetical severe accident in a Nordic-type BWR with molten core materials relocated to the lower head and subsequent debris bed and melt pool formation. The melt inflicts thermal and mechanical loads which can induce creep leading to a mechanical failure of the reactor vessel wall. Different melt pool configurations with the corresponding depths of 0.7 m, 1.1 m, 1.5 m, and 1.9 m are considered. Deformation of the vessel wall are assumed to have negligible effect on the melt pool heat transfer, therefore only one way coupling is employed. Debris bed heatup, remelting, melt pool formation, and heat transfer are predicted with the Phase-change Effective Convectivity Model (PECM) [8][9]. The PECM is implemented on the platform of the commercial CFD code FLUENT and transient heat transfer characteristics are provided for the thermo-mechanical strength calculations. The creep analysis is performed using commercial code ANSYS, taking into account both the thermal and integral mechanical loads on the RPV. Figure 3.3 shows the 2D axisymmetric geometry, mesh, and mechanical load on the reactor vessel that are considered in the structural analysis. Details of the computational treatment can be seen in [10] [11].

A snapshot of the temperature and melt fraction for H = 0.7 m debris bed at t = 4.44 h is shown in Figure 3.4. The debris bed is surrounded by the water-cooled CRGTs so that higher level of temperature can be seen in-between CRGTs and consequently the debris is melted first in these regions. The volume-averaged temperature at this time is about 2367 K while the volume fraction of the liquid melt is around 0.5. Figure 3.5 shows the temperature and liquid melt fraction for H = 1.9 m debris bed at t = 3.47 h. In comparison to the 0.7 m case, the cooled CRGTs are not evenly placed in the space occupied by the melt and there is a significant region on the upper end where the debris is melted faster than in the rest of the debris bed. At this time the volume fraction of liquid melt is around 0.3 and the volume averaged temperature is about 2386 K.

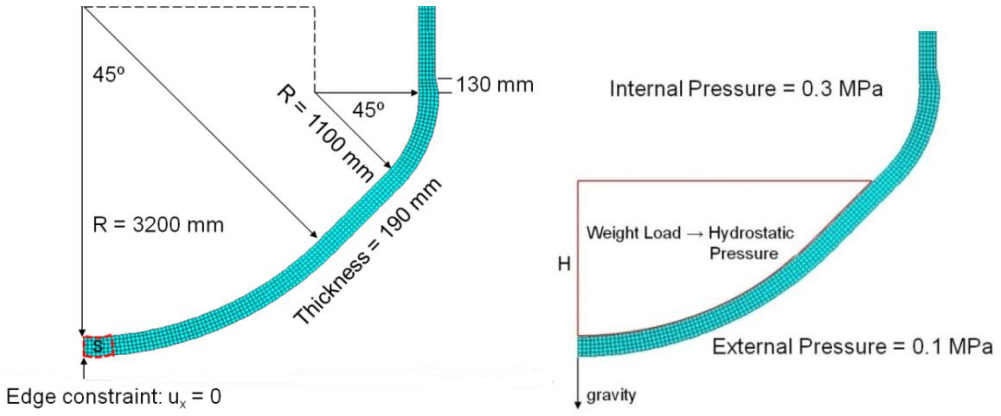

(a) *(b)*

Figure 3.3: (a) 2D axisymmetric geometry and mesh with 850 quadrilateral elements and 2901 nodes, and (b) mechanical load on the reactor vessel. The mark 'S' corresponds to the IGT section considered in the IGT failure study.

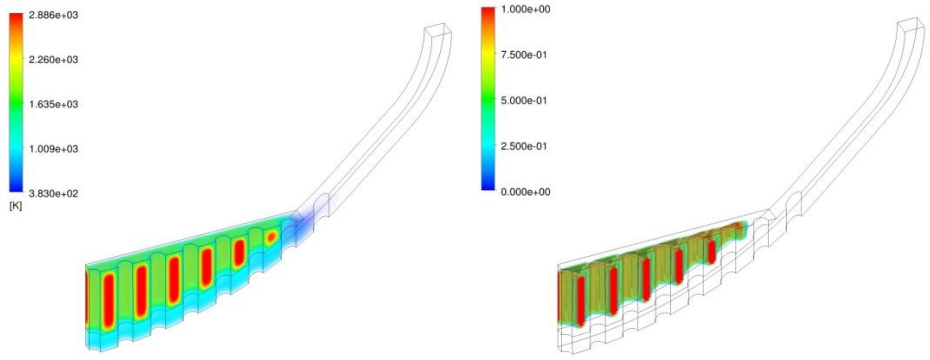

(a) *(b)*

Figure 3.4: PECM calculation with (a) Temperature profile at t = 4.44 h for H = 0.7 m debris bed, and (b) corresponding melt fraction.

Figure 3.6 shows the von Mises creep strains and displacements of the vessel wall for the case with melt pool depth H = 0.7 m (about 30 tons of melt). At time t = 4.72 h in Figure 3.6a, the maximum creep strain has reached 0.018 with maximum displacement of 0.06 m. Then at time t = 4.92 h (Figure 3.6b), the maximum creep strain has reached 0.19 located along the vicinity of the top of the melt pool

while most part of the lower section has creep strains between 0.02-0.17. Furthermore, the maximum displacement at the bottom center of the pressure vessel has become 0.26 m and displacements get smaller as one reaches the top of the pool which indicates a 'ballooning' type of failure. The rest of the vessel has negligibly small displacements. This ballooning mode of failure intensifies in Figure 3.6c at a later time t = 5.0 h, although, we cannot consider the displacements and creep strains at this time to be reliably predicted since the maximum creep strain has reached 0.39[8]. To demonstrate the importance of inclusion of creep analysis, Figure 3.6d shows a thermo-mechanical analysis with the same thermal loading but without creep modeling in mechanical analysis at time t = 5.0 h and the maximum total mechanical and thermal strain has only reached 0.008 with a maximum displacement of 0.05 m. Even at a later time t = 10.0 h, the total mechanical and thermal strain has reached 0.03 and the maximum displacement has become 0.10 m.

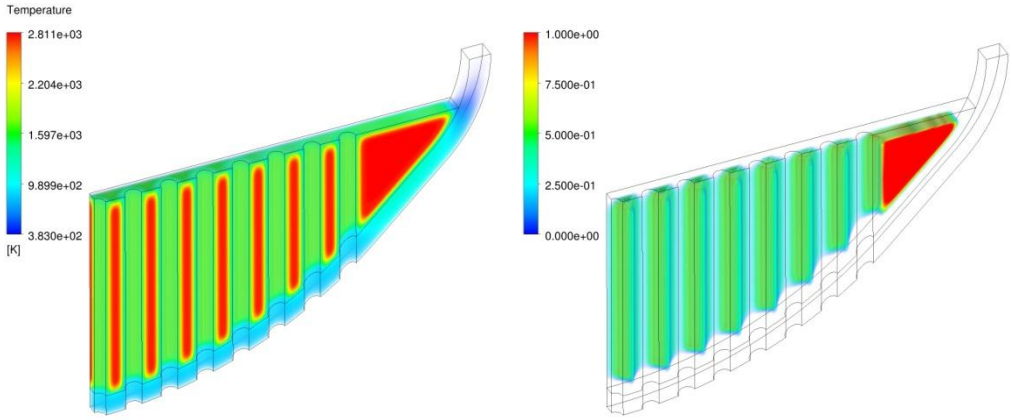

(a) *(b)*

Figure 3.5: PECM calculation with (a) Temperature profile at t = 3.47 h for H = 1.9 m debris bed, and (b) corresponding melt fraction.

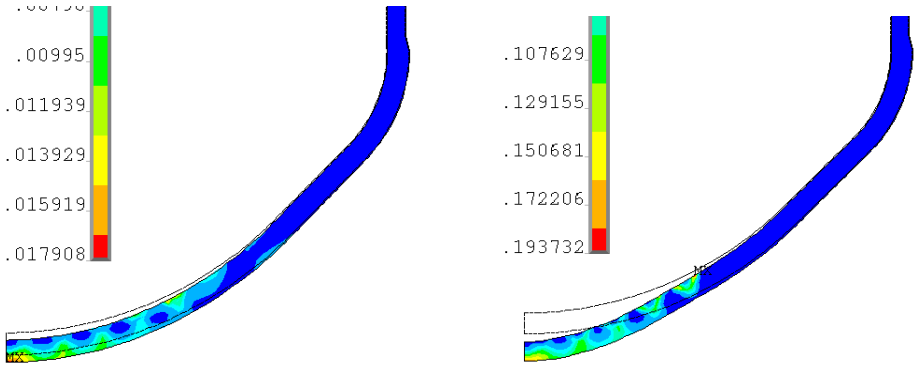

(a) t = 4.72 h (with creep modeling) *(b) t = 4.92 h (with creep modeling)*

[8] Generally creep strains above 0.20 are considered less reliable.

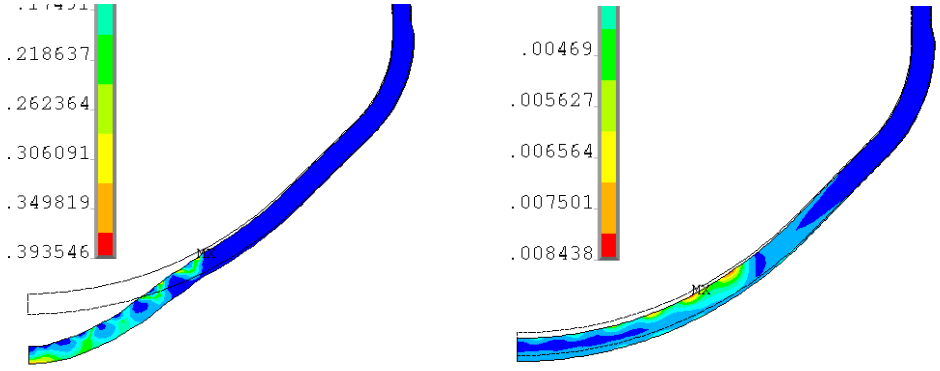

(c) t = 5.0 h (with creep modeling) *(d) t = 5.0 h (without creep modeling)*

Figure 3.6: Thermo-mechanical creep analysis with melt pool depth H = 0.7 m, (a)-(c) von Mises creep strains and displacements at 4.72 h, 4.92 h, and 5.0 h, respectively, and (d) Without creep: von Mises total mechanical and thermal strain at 5.0 h. The initial undeformed edges are superimposed. The maximum displacements are (a) 0.06 m, (b) 0.26 m, (c) 0.48 m, and (d) 0.05 m.

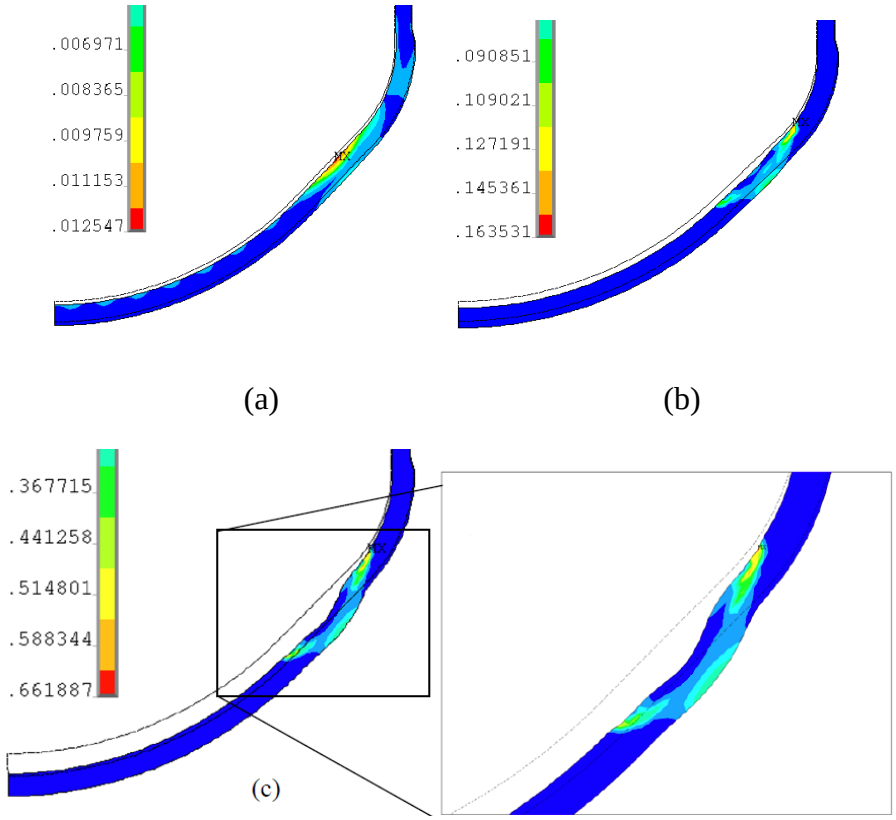

Figure 3.7: von Mises creep strains and displacements with melt pool depth H = 1.9 m at (a) 3.19 h, (b) 3.47 h, and (c) 3.61 h with a close-up of the localized creep region. The maximum displacements are (a) 0.04 m, (b) 0.07 m, and (c) 0.18 m.

At the maximum melt pool depth H = 1.9 m (which corresponds roughly to 200 tons of debris), a localized creep is also observed, as shown in Figure 3.7a. The maximum von Mises creep strain at time t = 3.19 h is 0.012 with a maximum displacement of 0.04 m. In Figure 3.7b which corresponds to a later time t = 3.47 h, the maximum creep strain increases to 0.16 with creep strains localized in the region right below the pool top surface. Furthermore, the maximum displacement is 0.07 m and displacements are almost uniform (small deformations) in the region below the localized creep. The same qualitative behavior intensifies at a later time t = 3.61 h as shown in Figure 3.7c with a magnified view of the localized creep region.

In both 0.7 m and 1.1 m cases, the melt pool covers a region in the lower head where cooled CRGTs are evenly distributed. A relatively uniform thermal load in this cases result in creep strains spread evenly in the vessel region heated by the pool. In combination with a relatively small mechanical load, that is, a melt pool mass below 80 tons, the distributed creep strain accounts for the ballooning type of failure.

In case of 1.5 m and 1.9 m deep pools the outer periphery of the melt pool (beyond the radius of 2.1 m) is not penetrated by cooled CRGTs. Along with the increased natural convection heat flux at the top region of the big pool, this results in a considerably higher temperature of the vessel wall above the height of 1.2 m from the bottom (or above 45°, see 10a for an example). The effect of higher thermal load in the region right below the top pool surface dominates along with the effect of considerably bigger mechanical load (more than 130 tons of melt) and changes failure mode to the localized creep. This behavior is consistent with our previous study [11] on a similar design but with smaller vessel lower head. With a 1.0 m debris depth, there exists a region in the outer periphery of the melt pool that is not penetrated by cooled CRGTs, thus changing the mode of failure to localized creep from a ballooning mode in the 0.7 m case.

Figure 3.8a shows the vertical displacement of the bottom center of the reactor vessel. We consider failure of the global vessel wall to happen when the maximum creep strain goes beyond 20 % but cannot infer exactly the time of failure and the corresponding deformations. However, once the maximum creep strain follows an accelerated increase, failure of the global vessel wall is considered imminent. For melt pool depths of 0.7 m and 1.1 m which shares the same mode of failure, the vertical displacement of their bottom center is almost identical within the reliably predicted range. A rapid increase of relative displacement and acceleration of vessel creep takes place after about 4.47 h. The external cooling of the vessel has to be applied prior to this time in order to be effective.

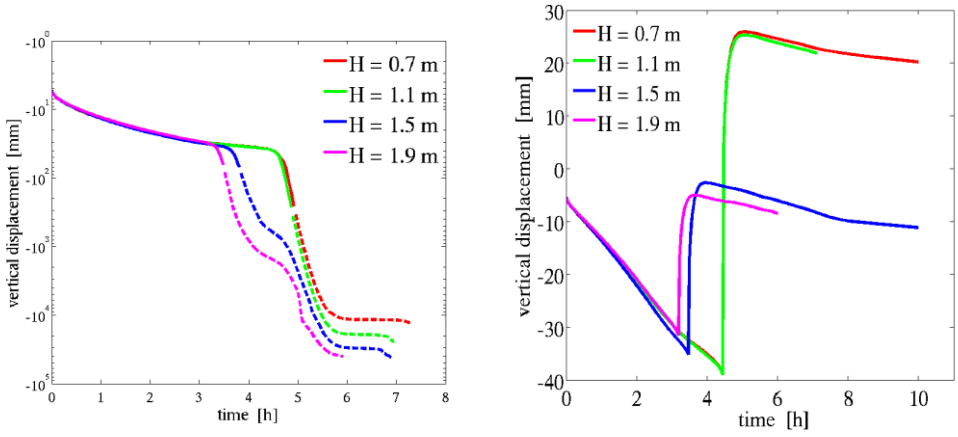

(a) *(b)*

Figure 3.8: (a) Vertical displacement of the bottom center of the reactor vessel with melt pool depths H = 0.7, 1.1, 1.5, and 1.9 m. The solid lines indicate reliably predicted results that correspond to maximum creep strains within 20 %. (b) Effect of external vessel cooling for pool depth H = 0.7 m with external cooling applied at t_c = 4.4 h, H = 1.1 m at t_c = 4.4 h, H = 1.5 m at t_c = 3.47 h, and H = 1.9 m at t_c = 3.19 h.

A summary of debris bed conditions for all cases, H = 0.7 m, 1.1 m, 1.5 m, and 1.9 m, is given in Table 3.1. This information can provide an estimate of the debris bed conditions in case of a global vessel wall failure, that is, the amount and superheat of the melt that is available for ex-vessel melt release. For the case H = 0.7 m, the two timings t1 = 4.47 h and t2 = 4.9 h correspond to the estimated start of creep acceleration and the time where 20 % maximum creep strain has been reached, respectively. The amount of melt at t2 = 4.49 h is around 18 tons (from the total mass of 30 tons) with an average melt superheat of about 160 K. After 30 min, the amount of melt increases to about 20 tons with an average melt superheat of around 168 K. For the debris bed conditions of H = 1.9 m with a total mass of 200 tons, an estimated 68 tons of melt has formed at t2 = 3.5 h with an average melt superheat of only 23 K. But after 30 min, the amount of melt rapidly increases to about 112 tons and also with a significant increase in melt superheat to around 103 K.

In all considered cases, the results of analysis indicate that vessel failure has to be expected if only CRGT cooling is applied. An important question for accident management is the possibility of in-vessel retention (IVR) by the means of combined CRGT cooling and ex-vessel cooling. In reality, the timing for activation of ex-vessel cooling (in the event of core damage) depends on many plant design-specific factors (time necessary to remove vessel insulation and pump the water up to the vessel level, etc.). In this study, we choose the time of external vessel cooling to be right before the beginning of vessel creep acceleration. In both the 0.7 m and 1.1 m cases, this time is 4.44 h, while it is 3.47 h in the 1.5 m and 3.19 h in the 1.9 m case. We assume that the water level at the external cavity pool has instantaneously reached the same level as the melt pool at the specified times. In this work, we use the simplest way to implement such vessel cooling by setting a temperature boundary condition at water saturation temperature, T = 373 K. The effect of external vessel cooling on the vertical displacement of the bottom center of the reactor vessel is

shown in Figure 3.8b. Prior to the application of external cooling, the vertical displacements are identical with the previous results (Figure 3.8a). Right after the application of external cooling, the relative vertical displacements in all cases rapidly decrease and two of those cases (shallower pools 0.7 m and 1.1 m) even surpass their initial positions. A check on the displacements of the other parts of the vessel wall also reveals the same behavior.

Table 3.1: Debris bed conditions at time t_2 where 20 % maximum creep strain has been reached and then after 30 minutes.

H [m]	Start time of creep acceleration, t_1 [h]	Time at max ~20 % creep strain, t_2 [h]	Amount of liquid melt at t_2 (and after 30 min) [ton]	Average melt superheat at t_2 (and after 30 min) [K]
0.7	4.47	4.9	18 (20)	160 (168)
1.1	4.47	4.9	52 (56)	187 (232)
1.5	3.58	3.8	58 (81)	72 (139)
1.9	3.31	3.5	68 (112)	23 (103)

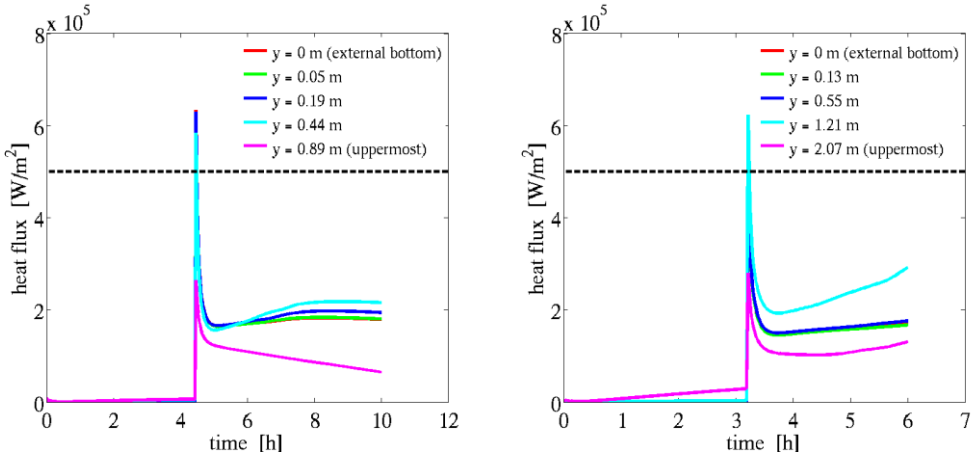

(a) *(b)*

Figure 3.9: Surface normal heat fluxes at the external vessel wall probed at different points with heights y from the external bottom for melt pool depths (a) H = 0.7 m, and (b) H = 1.9 m. The horizontal dashed lines represent the assumed CHF limit.

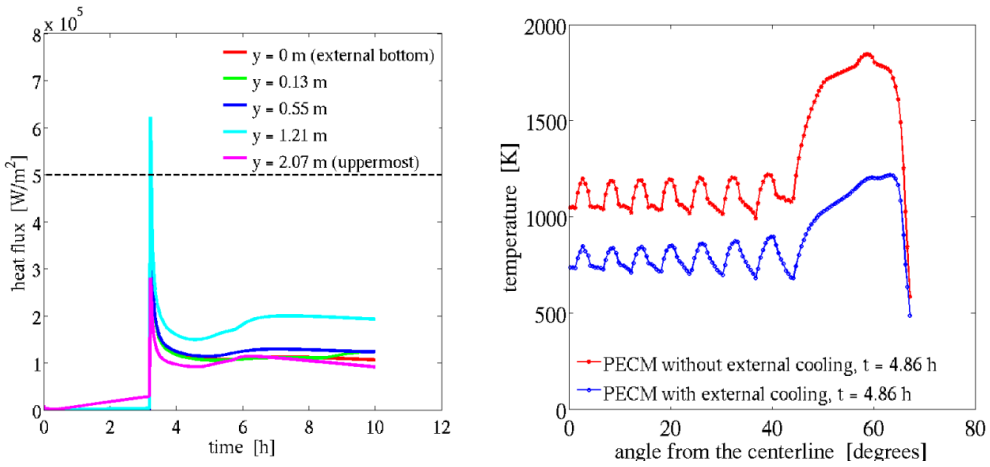

(a) *(b)*

Figure 3.10: (a) Effect of external cooling on the thermal load from the melt pool at a snapshot time t = 4.86 h for H = 1.9 m debris bed. (a) Heat flux at the external vessel surface for H = 1.9 m debris bed; (b) external vessel wall temperature.

It is known that the key to IVR by external vessel cooling is the avoidance of film boiling regime which is characterized by the critical heat flux (CHF), which is conservatively assumed as 500 kW/m^2 here [10]. The normal heat fluxes at the external vessel surface probed at different points with depths y from the vessel bottom are shown in Figure 3.9 for all considered cases. Prior to the corresponding cooling times, the normal heat fluxes are negligible according to the prescribed boundary condition. At the instant of application of external vessel cooling, the normal heat fluxes suddenly peak which is a result of assumed instantaneous changes in thermal boundary condition. In reality, the vessel external surface is initially at temperature higher than the minimum film boiling temperature and its cooling and then re-wetting processes are expected to be gradual. The eventual transition from film boiling to nucleate boiling is expected to occur since the steady heat flux is well below CHF, however, how much time this process may take has to be addressed in a separate study.

In all cases, the heat flux quickly settles to a level below the CHF limit. It should be noted that external vessel cooling was considered only in the ANSYS simulation of thermo-mechanical behavior of the vessel wall. However, the external vessel cooling also has an effect on the heat transfer in the melt pool, which was not taken into account in this case. To assess the effect, we rerun the melt heat transfer problem for the 1.9 m pool case, taking into account the vessel cooling by changing external vessel temperature boundary conditions in the PECM analysis (see Figure 3.10b for a snapshot) and then performing the structural analysis with new temperature boundary conditions supplied by PECM. As shown in Figure 3.10b, we found that the wall normal heat flux settles to the level of about 110 *kW/m*^{2} except for one location y = 1.21 m which settles to the level of about 200 *kW/m*^{2} which means that all are well below the assumed CHF limit.

3.2.3. Effect of low Pr on Heat Transfer from Melt Pool to Vessel Wall

In this work we use Computational Fluid Dynamics (CFD) method, experiments and the Effective Convectivity Model (ECM) and Phase-change ECM (PECM) for uncertainty reduction in accident analysis for Boiling Water Reactors (BWRs). The effect of low fluid Prandtl number (*Pr*) on heat transfer from a melt pool to the BWR vessel wall has been examined using numerical experiments performed with a reliable CFD tool. The local heat transfer effect due to corium melt low Prandtl number on the downward heat transfer coefficient has been found to be significant [12]. The local downward heat transfer coefficient is a function of *Pr*; as the *Pr* is decreased, the local effect is enlarged to a broader area. However, the *Pr* dependency of the Nusselt number, *Nu*, local peak value is non-monotonic.

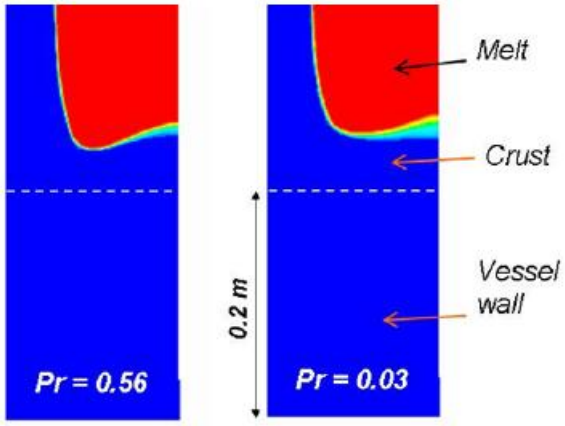

Figure 3.11: Evolution of the crust boundaries after 4.2h (liquid fraction in red).

Figure 3.11 shows melt pool (red), crust (blue) and mushy zone (green) configuration at t=15000 s (about 4.2 h) for two cases of the downward heat transfer coefficient profile (*Pr*=0.56 and *Pr*=0.03). Due to local crust erosion, the minimum crust thickness in these two cases is considerably thinner compared with the case where uniform, correlation based profile is used for downward *Nu*. Such erosion of the crust results in a higher heat flux to the vessel wall and in higher vessel temperature (see [12] for more details).

The integral effect of the local heat transfer enhancement is found to be significant, and the vessel wall temperature is considerably increased. However, we also found that this effect takes place at a later timing than the rapid acceleration of vessel thermal creep starts, at least as considered in the case of 0.7 m deep melt pool. Thus global vessel failure is not sensitive to the local heat transfer enhancement caused by fluid low *Pr*. Further work is needed to examine systematically the timing of heat transfer and thermo-mechanical creep effects in different relevant configurations of the melt pool including different values of solidus/liquidus temperatures.

3.2.4. Coupled PECM/RELAP5/ANSYS Analysis of CRGT Cooling Efficiency

Assessment of the efficiency of CRGT tube cooling efficiency requires resolving heat transfer not only in the melt pool, but also water flow and heat transfer inside the CRGTs. Therefore part of this project involves development of code coupling employing a domain decomposition scheme [13]. The coupled code is used to simu-

late heat transfer in a debris bed located in the lower plenum of a BWR vessel in the presence of CRGT cooling. Heat transfer in a solid debris bed can be simulated by a pure heat conduction model. In presence of liquid pools, the PECM implemented in the FLUENT code to simulate convection and phase change is used. Two-phase flow inside the CRGTs and heat conduction in the CRGT walls are simulated by the RELAP5 code. FLUENT and RELAP5 are coupled through their boundary conditions (see Figure 3.12). The temperature on the external surface of CRGTs calculated by RELAP5 is used as a boundary condition for the PECM, while the heat flux on the external CRGT surface calculated by FLUENT is used as a boundary condition for RELAP5 simulation. No mass crosses the boundary between the FLUENT and the RELAP5 subdomains.

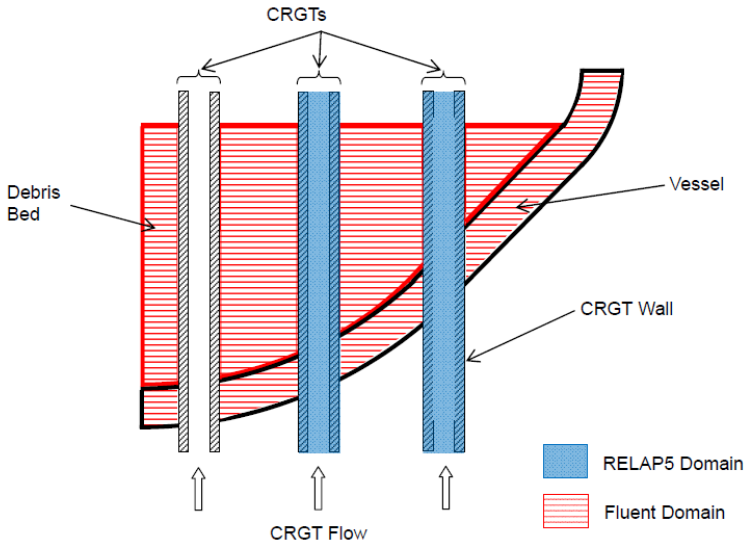

Figure 3.12: The simulation domain is decomposed into two non-overlapping domains. RELAP5 and FLUENT are coupled in space through the boundary conditions.

For the coupling in time (see Figure 3.12), the two codes march in parallel and exchange information on the fly. To guarantee the consistency of the solution on the RELAP5 and the FLUENT side, an internal iteration is performed within each time step. The efficiency of the calculation is increased by an adaptive coupling time step strategy. Since no experimental or analytical solution is available for comparison with the results of the coupled code, the calculation goal is to assess the implementation with regards to a time-converged reference solution. This comparison shows that, as long as the solution is stable, it is possible to drive an adaptive coupling time stepping strategy by controlling the simulation error, calculated on the basis of the coupling quantities (heat flux and temperature on the external CRGT wall). This allows the current implementation of the coupled code to balance accuracy and computational efficiency.

3.2.5. Instrumentation Guide Tube Failure during a Severe Accident in a BWR

Another important part of this subproject focuses on the nature and timing of Instrumentation Guide Tube (IGT) failure in case of severe core melt accident in a Nordic BWR (see [14] for more details). Two succeeding calculations were performed, a thermo-mechanical creep analysis for lower-head of the vessel wall (see

Figure 3.3) and subsequently for an IGT section. We have considered the maximum melt pool depth of 1.9 m and one location of the IGT that is closest to the center of the lower plenum. Details of the computational treatment and results can be seen in [14]. In the first calculation, we have found a localized creep mode of global vessel wall failure where creep strains are concentrated in the vicinity of the uppermost region of the melt pool. Results of global vessel deformation and timing of failure from this calculation as well as local transient thermal load from PECM calculations are then used for the next analysis of the IGT section.

There are two attributing factors that can affect the displacement of the flow limiter area: (i) thermal expansion due to local thermal load, and (ii) applied displacement (normal to the right curved-surface boundary) as consideration of the global displacement of the vessel lower head. Figure 3.13 shows that the displacement of the IGT housing points in a horizontal cross section of the flow limiter is parallel to the applied displacement, which indicates that the global displacement of the lower head dominates over thermal expansion in the flow limiter area.

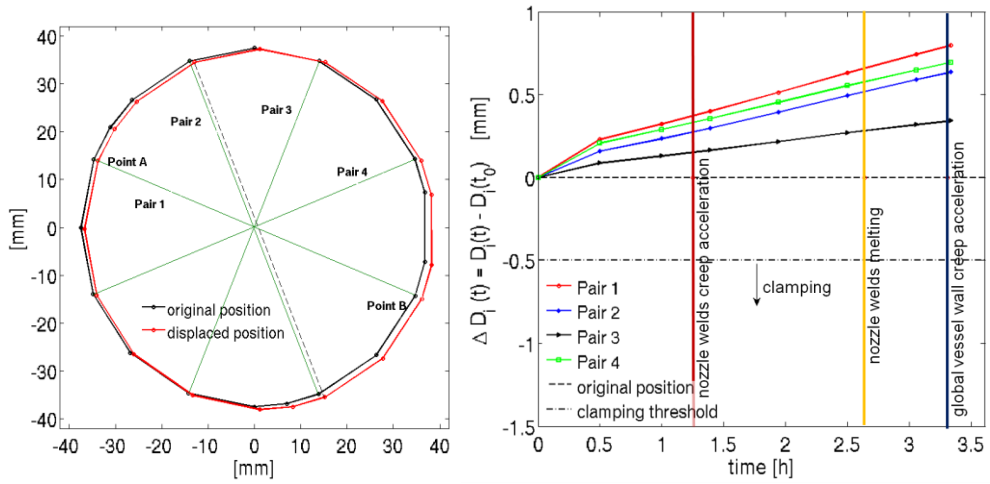

(a) *(b)*

Figure 3.13: (a) Displacement of points along the flow limiter area and four pairs of points for which the distances between points are measured with respect to time; (b) The change in distances $\Delta D_i(t) = D_i(t) - D_i(t_0)$ for each pair i and time t where $D_i(t_0)$ is the distance between the points in pair i at time t = 0. The vertical lines correspond to the estimated time of nozzle welds creep acceleration, nozzle welds melting, and global vessel wall creep acceleration.

In Figure 3.13b the change in distances between the points with respect to time is shown. The maximum distance between the edge of the flow limiter and the IGT casing is given at 0.5 mm. Thus, clamping is defined as $\Delta Di\ (t) \leq -0.5$ mm, for any pair i at any time t > 0 but before the nozzle welds fail. Analysis of results presented in Figure 3.13b suggests that at given melt pool depth of 1.9 m and a location of the IGT close to the bottom center, the IGT is not clamped in its housing during the entire time until global vessel wall failure takes place. This result suggest that in the considered case of 1.9 m melt pool, the dominant vessel failure mode is IGT failure and it happens at least 1 h before the global vessel failure. Other melt pool depths and/or other locations of the IGT might result otherwise, but are not covered here

and will be the subject of further inquiry. Preliminary calculations with smaller depth pools indicate that an opposite behavior can also be observed, namely a contraction of the flow limiter gap. An important future step for further improvement in the current methodology is full 3D modeling of the vessel global deformation, taking into account penetrations.

3.2.6. Implications to Reactor Safety

For a Nordic BWR, a coupled thermo-mechanical creep analysis reveals that if only CRGT cooling is activated, then (i) the cases with 0.7 m and 1.1 m melt pool depths result in a ballooning type of vessel failure where creep strains are distributed in the lower section of the vessel that is covered by melt pool, and (ii) the cases with 1.5 m and 1.9 m melt pool depths result in a localized creep where the creep strains are concentrated in the vicinity of the uppermost region of the melt pool. These two modes may lead to different melt releases in terms of breach size, melt mass and melt compositions and superheat. If an external vessel cooling is implemented right before creep accelerates, in all the melt pool configurations considered above, we found that in-vessel retention (IVR) of the melt is possible by the CRGT plus external cooling.

Another coupled thermo-mechanical creep analysis reveals that at given melt pool depth of 1.9 m and a location of the IGT close to the bottom center, the IGT is not clamped in its housing during accident, and the dominant vessel failure mode is IGT melt-through and it happens at least 1 h before the global vessel failure. The consequence of an IGT failure is quite different from a global vessel wall failure in terms of melt release conditions.

The other activities in INCOSAM subproject demonstrated that the coupling of PECM/RELAP5/ANSYS codes provides an approach to improve the fidelity of CRGT cooling analysis, and the global vessel failure is not sensitive to the local heat transfer enhancement caused by fluid low *Pr* of corium, at least in the case of 0.7 m deep melt pool.

3.3 Debris Formation (DEFOR)

3.3.1. Motivation and Approach

There are three major sources of uncertainties in assessment of the risk of formation of a non-coolable debris bed: (i) conditions of the melt release from the vessel, which generally depend on the accident scenario and in-vessel accident progression, (ii) phenomena of the debris bed formation in the process of core-melt fragmentation in water, that define porous media properties of the debris bed, and finally (iii) phenomena of the two-phase flow and heat transfer that define coolability of the volumetrically heated debris bed. While INCOSAM is considering item (i), DEFOR and POMECO are focused on the issues related to item (ii) and (iii).

The objective of the DEFOR study is to quantify the configurations and characteristics of debris beds which are important for the debris bed coolability under different accident scenarios. Complex phenomena and feedbacks in the process of the debris bed formation were first identified in [24] as defining for the properties of the bed and thus its coolability. The architecture of the DEFOR research program was de-

signed with the ultimate goal to develop a Debris Bed Formation and Coolability Map. The program is based on decomposition of the complex task in a set of separate effect studies, namely development of (i) agglomeration mode map; (ii) particle size and morphology (porosity) map; and (iii) debris bed shape map. Sensitivity and uncertainty analyses are employed at synthesis stage in order to connect melt release conditions with the debris bed coolability (see Figure 3.14: DEFOR Research program).

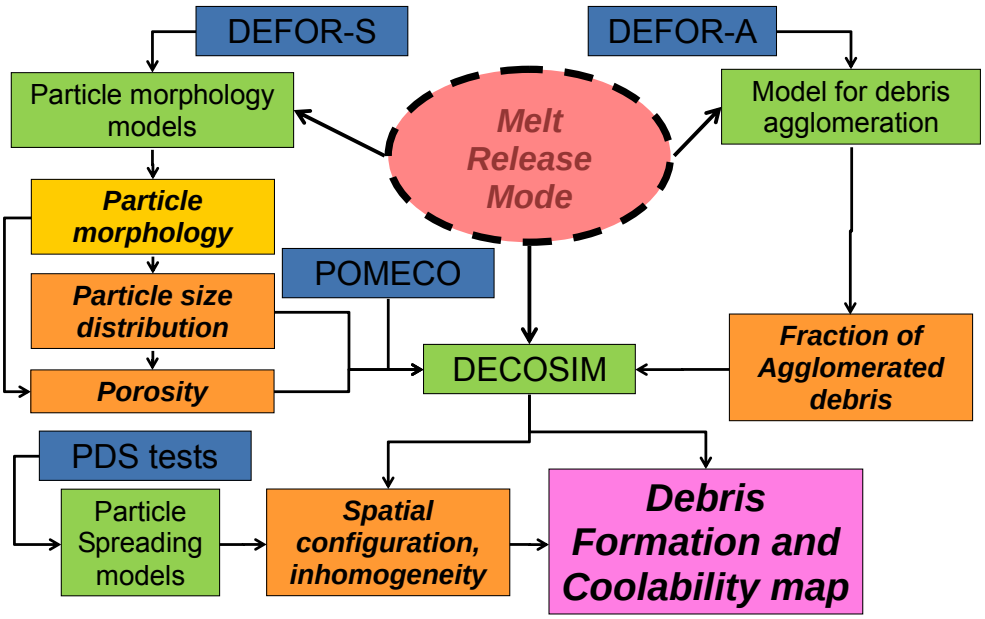

Figure 3.14: DEFOR Research program

3.3.2. Development of Models for Prediction of Particle Morphology and Size Distribution

Prediction of particle size distribution and morphology (porosity) is of paramount importance for assessment of the bed coolability. Results of the DEFOR-S tests paved way to suggestions that melt fragmentation and the resulting particle morphology are largely influenced by (i) melt droplet instability and breakup; (ii) melt cooling and solidification; (iii) cavity formation; and (iv) solid particle [3]. In this section we discuss new insights into mechanisms of a debris particle formation in the process of a melt pouring and quenching in a pool of water.

Water subcooling was identified as an important factor which governs transition between the hydrodynamic breakup dominated and solid particle fracture dominated regimes of the debris formation which significantly affects porosity of the debris bed [3], [16], [17]. The debris formed at low subcooling of water, have rounded shape (Figure 3.15 left) which is an evidence of hydrodynamic breakup, while at higher subcooling the particles are rock-like with sharp edges (Figure 3.15 right) apparently originated from solid particle fracture [3]. It is instructive to note that the difference in subcooling of water which causes transition from round-shape to rock-like debris morphology is only about 30°C. Observations of particle morphology reported in experiments performed in the past with prototypic corium mixtures and water as a coolant and in experiments with UO2 fuel poured in sodium suggest that corium and UO2 debris morphology is inclusive of types identified in the DEFOR-S

tests. See also a detailed review of available data from experiments with prototypic materials [16].

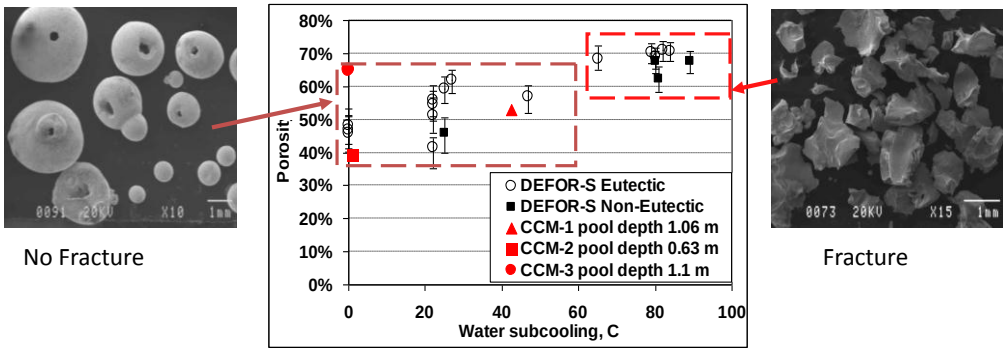

Figure 3.15: Influence of the morphology of debris on porosity of the bed.

The following hypothesis was considered in [16] [17] in order to explain how moderate changes in water subcooling can drastically change morphology of the debris particle: i) Transition from round-shape to rock-like particle morphology is a result of transition from hydrodynamic breakup to solid particle fracture due to catastrophic increase of thermal stress; ii) The growth of thermal stress is caused by rapid changes in the heat transfer during transition from film to nucleate boiling which is highly sensitive to water subcooling. There are considerable uncertainties related to the physical mechanisms of solid particle fracture, transition from film to nucleate boiling heat transfer, effects of particle size, material properties, and non-uniform distribution of the heat flux over the particle surface. Therefore simplified, computationally efficient models (see details in [16] [17]) were employed to perform sensitivity studies in order to assess the importance of different uncertainties.

In order to resolve thermo-elastic stress in a spherical particle we are considering cooling and solidification dynamics of an initially molten droplet. The solidification of the droplet starts from the outer surface. To handle the uncertainties in minimum film boiling temperature T_{mfb} and in the maximum nucleate boiling heat flux Qnb a parametric sensitivity study has been performed [16], [17].

Figure 3.16 depicts typical extreme values of normalized tangential thermal stress at the internal and external surfaces of 2 mm size particle made of UO2 (Figure 3.16a) and DEFOR simulant material (Figure 3.16b) as functions of instantaneous temperature of the particle surface. There are two maximums of the normalized stress for UO2 particle. The first (and the biggest) maximum corresponds to the moment of time when solidification of the particle is just finished. Although tangential stress is order of magnitude higher than fracture stress, the temperature is well above brittle-ductile limit (which is considered to be in the range of 1000 K – 1570 K). It is expected that above the brittle-ductile limit the material will experience plastic deformations and no crack initiation solid particle fracture will occur. Second maximum of tangential stresses is observed during transition from film to nucleate boiling. Intensity of the second peak of the stress increases when water subcooling is increasing. When stress exceeds the fracture limit ($|\bar{\sigma}|>1$) crack initiation, growth and eventually solid fracture can be expected because particle temperature is below

the brittle-ductile limit. There are some differences in behavior of the stress in case of the melt simulant particle (Figure 3.16b). Main reason for the differences is that collapse of film boiling at high subcooling of water (>60K) can occur even prior to completion of the particle solidification leading to significant thermal stress which is achieved at relatively low surface temperatures (700 K – 1000K).

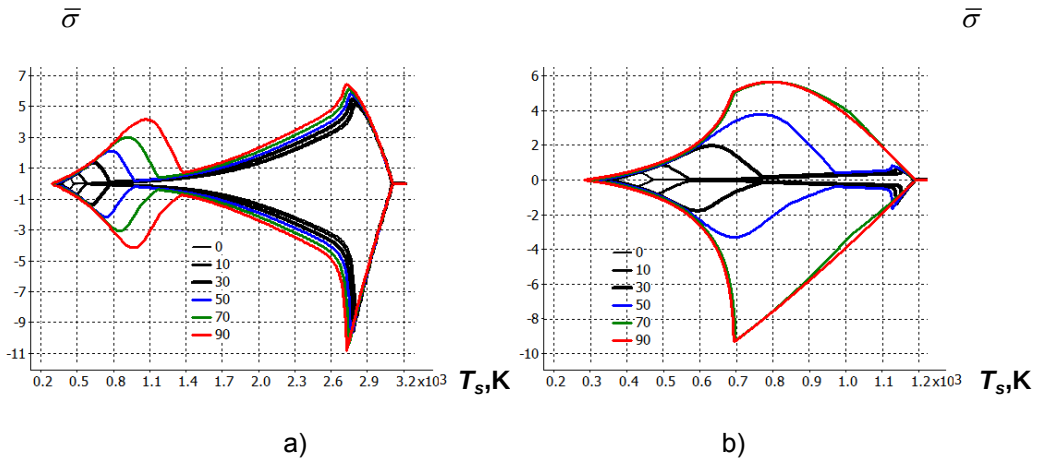

Figure 3.16: Tangential stresses normalized by fracture stress as a function of particle surface temperature for UO_2 (a) and simulant material (b) particle of 2 mm in diameter. Different curves correspond to water different subcooling ΔT_{sub} =0 K, 10 K, 30 K, 50 K, 70 K, 90 K [16], [17].

Based on the simulation results, the influence of water subcooling on particle fragmentation mode was summarized in a form of a map (Figure 3.17), which defines whether the particle will experience fracture or not. The map has two parameters: particle diameter, and subcooling of water. To develop the map extensive parametric study has been performed (see details in [16][17]). All together to create one map for each material we calculated 2304 cases of particle quenching. Analysis of the results suggested that there is no significant influence of initial melt superheat on solid particle fracture.

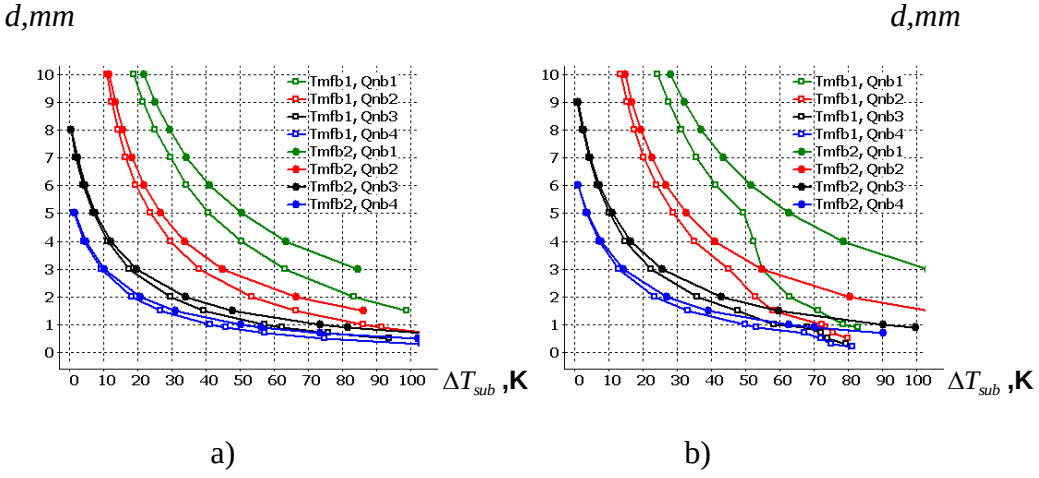

Figure 3.17: Maps of particle fracture: a) UO2; b) melt simulant material.

We determine critical water subcooling for each particle diameter at which $|\bar{\sigma}| = |\sigma_\theta / \sigma_F| = 1$ and temperature is below brittle-ductile limit. The curves in Figure 3.17 define two domains in the map: above the curve particles will be fractured, below the curve particle will not fragment. Analysis of the map suggests that if water subcooling is above 70K only very small sub-millimeter particle may survive and the rest will be fractured by thermal stress. This finding is in good agreement with observations from DEFOR-S experiments [3]. Map for UO_2 particle is qualitatively similar to the simulant material map. Detailed discussion of the influence of competing processes of hydrodynamic fragmentation and crust formation is presented in [16][17]. The map provides a tool for prediction of particle morphology (round shape or rock-like). The map, provides valuable insights into sensitivity of particle fracture to different factors such as transition boiling and melt properties. The results also suggest that with proper simulant material it is possible to model fragmentation behavior and resulting particle morphology of core melt material in out-of-pile experiments.

3.3.3. Development of Agglomeration Mode Map

Debris agglomeration and especially formation of "cake" regions can significantly increase hydraulic resistance for the coolant flow and thus negatively affect coolability of the debris bed [18]. If melt is not completely solidified prior to settlement on top of the debris bed, then agglomeration of the debris and even "cake" formation is quite possible [4][19]. Although agglomeration of the debris and "cake" formation have been observed in previous fuel-coolant interaction (FCI) experiments with prototypic corium mixtures (e.g. FARO and CCM tests) and with corium simulant materials (e.g. DEFOR-E and DEFOR-S tests), there was a lack of systematic experimental data and understanding of the governing physical mechanisms of the debris agglomeration. Debris agglomerate is a group of particles "soldered" together by liquid melt (Figure 3.18b). "Cake" (Figure 3.18c) can be formed when fraction of liquid melt is big enough to solder together most of the solidified melt in the bed.

The goal of the first series of DEFOR-A (Agglomeration) tests is to provide systematic experimental data about mass fraction of agglomerated debris obtained in the process of melt pouring into a pool of water under well-defined conditions. Specific goal of the tests is to study the effects of (i) pool depth; (ii) water subcooling; (iii) melt jet diameter; and (iv) initial melt superheat, on the fraction of agglomerated debris.

The DEFOR-A tests are performed in the DEFOR facility (Figure 3.18a) which is composed of a 45kW medium-frequency (up to 30 kHZ) Induction Furnace (IF) for melt generation, a melt delivery funnel, and a coolant tank with glass windows for visual imaging of transient melt-coolant mixing and debris formation. The simulant-material melt is generated in a SiC crucible. The liquid melt is delivered to the funnel by tilting the crucible. The delivery funnel is conical with a replaceable discharge nozzle up to 25 mm in diameter. The test section is a rectangular tank (2 m tall, with horizontal cross section 0.5x0.5 m) open to the atmosphere of the lab.

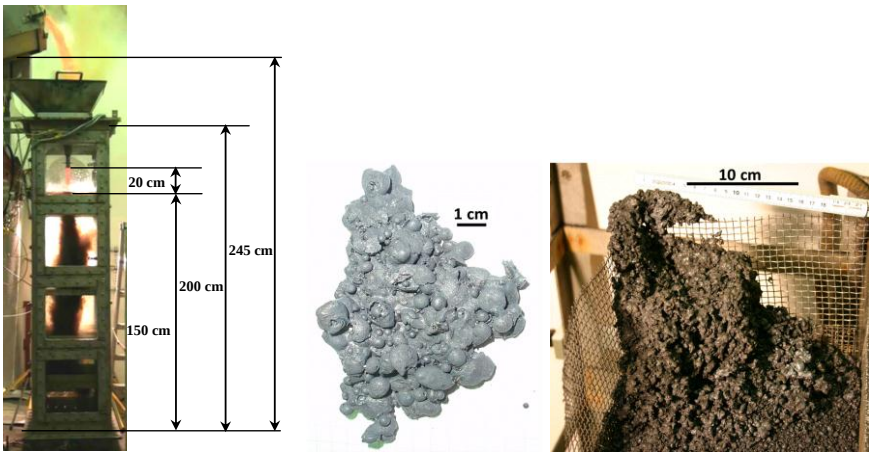

a) (b) (c)

Figure 3.18: DEFOR-A experimental facility (a), Agglomerated debris (b);cake (c).

In the DEFOR-A experiment up to 3 liters of melt simulant materials are poured in a pool of water about 1.5 m deep. The catchers for the debris are installed at different elevations inside the test section to collect debris and agglomerates during the melt pouring process. Analysis of the debris collected in the catchers provides data about mass fraction of agglomerated debris as a function of water pool depth at given conditions of the tests. Experimental conditions of the DEFOR-A1~A9 tests are presented in Table 3.2. Eutectic mixture of Bi_2O_3–WO_3 (molar fractions Bi_2O_3=27%, WO_3=73%) is used in all tests. Melting temperature of the mixture is 1143°K. Detailed discussion of the DEFOR-A results are presented in [19], [4]. The results of the tests are summarized in Figure 3.19. The DEFOR-A tests provide first of its kind systematic experimental data about the mass fraction of agglomerated debris as a function of water pool depth. Particle size distribution measured in the DEFOR-A tests is in good agreement with the data from the FARO fuel-coolant interaction experiments with corium mixtures, which confirms that material employed as simulant material reproduces fragmentation behavior of corium melt.

Table 3.2: DEFOR-A tests conditions.

Parameters	**Tests**								
	A1	A2	A3	A4	A5	A6	A7	A8	A9
Melt temperature, K	1253	1246	1483	1221	1245	1279	1349	1255	1343
Melt superheat, K	110	103	-*	78	102	136	206	112	200
Melt jet initial diameter, mm	10	20	20	20	10	12	25	25	20
Elevation of nozzle outlet, m	1.7	1.7	1.7	1.7	1.7	1.7	1.62	1.62	1.7
Jet free fall height, m	0.18	0.18	0.18	0.20	0.18	0.18	0.20	0.20	0.18
Duration of melt release, s	38	11	-	11	38	20	10	10	11
Average flow rate, l/s	0.079	0.273	-	0.273	0.079	0.150	0.300	0.300	0.273
Initial average melt jet velocity, m/s	1.01	0.87	-	0.87	1.01	1.33	0.61	0.61	0.87
Water pool depth, m	1.52	1.52	1.52	1.50	1.52	1.52	1.42	1.42	1.52
Water initial temperature, K	346	366	345	346	364	346	356	355	355
Water subcooling, K	27	7	28	27	9	27	17	18	18

* Apparently, chemical changes in the melt composition occurred in the DEFOR-A3 test due to erosion of the SiC crucible by the melt.

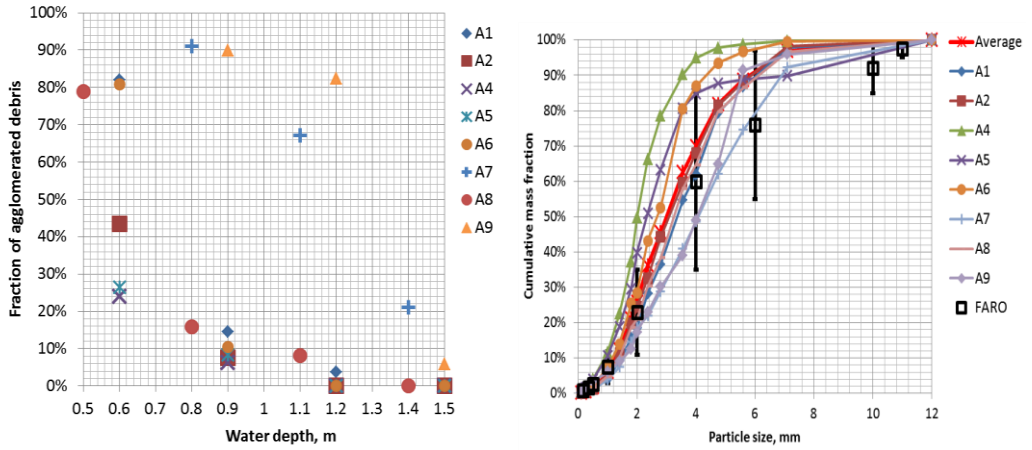

a) b)

Figure 3.19: DEFOR-A: (a) Fraction of agglomerated debris as a function of water pool depth; (b) Particle size distribution.

Main finding of the DEFOR-A tests is that fraction of agglomerated debris decreases rapidly as a function of the pool depth. Debris below 1.5 m consists of completely fragmented particles in all tests, except the DEFOR-A7 test conducted at 206°C melt superheat. Significant increase of the fraction of agglomerated debris in all catchers is observed in the DEFOR-A7 test when compared with other tests. Nevertheless, the same tendency of rapid decrease of the fraction of agglomerates is clearly visible from the DEFOR-A7 data. Higher melt superheat and bigger jet diameter generally leads to increase of mass fraction of agglomerated debris. Jet diameter (in the range 10 mm – 25 mm) has less profound influence than melt superheat. The effect of water subcooling on fraction of agglomerates is non-monotone and needs further investigation. Increasing of high subcooling of water effectively prevents agglomeration. At relatively low subcooling an inverse dependency is observed. There is a hypothesis [20] that upward directed steam flow (which increases with decreasing of subcooling of water) in the melt-coolant interaction zone can considerably increase characteristic time for particle settlement and thus decrease mass fraction of agglomerates.

Until recently, debris agglomeration and cake formation have not been studied systematically in experiments and there was no analytical activity for modeling of the agglomeration phenomena. A concept of agglomeration mode map has been proposed in [20] for prediction of debris agglomeration in different plant accident conditions. A conservative-mechanistic approach to quantify the mass fraction of agglomerated debris was developed and validated [5] [21][22] against DEFOR-A data. The approach combines (i) the deterministic code VAPEX [21], which is used as a computational vehicle for the simulation of the fuel coolant interaction (FCI) phenomena including jet breakup, formation of liquid droplets, sedimentation and solidification of the particles, with (ii) conservative assumptions in modeling, which are used to bound intrinsic epistemic uncertainties in physical phenomena. The sensitivity of predicted mass fraction of agglomerated debris to different assumptions in modeling (epistemic uncertainty) and to different uncertain parameters of scenario (aleatory uncertainty) of melt-coolant interaction was studied in [5]. Specifically

the influence of jet breakup mode and effect of modeling of inter-phase heat transfer and resulting steam production rate in the melt-coolant interaction zone were considered. It was demonstrated that conservative treatment of the uncertainties creates sufficient margin and simulation data are enveloping the set of mass fractions of agglomerated debris obtained at various experimental conditions.

Three different modes of agglomeration were defined in [21] according to their potential impact on coolability:

1. No agglomeration. The bed consists of completely fragmented debris.
2. Agglomerated debris. The bed consists of partially agglomerated debris connected by inter-particle bonds.
3. Cake. The bed represents a chunk of solidified melt with no open porosity for coolant ingression into the cake interior.

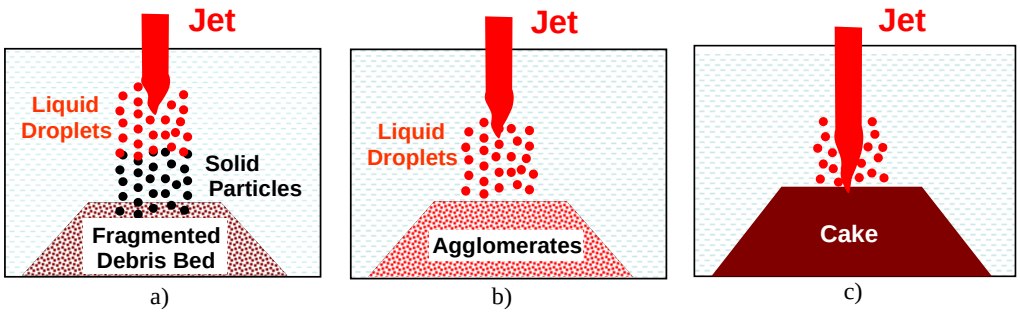

Figure 3.20: Modes of debris agglomeration: a) fragmented debris; b) agglomerated debris; c) cake.

Conservative assumptions about the conditions for onset of the different modes of the debris agglomeration are as follows: we assume that agglomeration modes are defined by the state of the melt fragments right before depositing (pre-deposition state) on top of the debris bed as shown in Figure 3.20. No-agglomeration (first mode, Figure 3.20a) is expected when melt particles already have a thick crust when they are depositing on the top of the bed. Partial agglomeration (second mode, Figure 3.20b) is expected when some fraction of the debris may reach the top of the debris bed in the form of liquid droplets. A cake is formed when jet breakup length is greater than or equal to the depth of the water pool (third mode, Figure 3.20c). It is assumed that agglomeration is a result of interactions between partially liquid droplets with each other and with neighboring solid particles. The jet breakup phenomena and melt droplet solidification processes affect distribution of relative crust thickness, which in turn defines mass fraction of agglomerated debris. It is further assumed that mass fraction of agglomerated debris is proportional to the mass fraction of completely liquid droplets and thin-crust particles (“liquid” or “glue” particles).

$$m_{aggl} = \alpha \cdot m_{liq} \qquad \textbf{(1)}$$

where m_{aggl} is mass fraction of agglomerated debris, m_{liq} is mass fraction of liquid particles (with relative crust thickness less than 0.1), $\alpha = \alpha\left(m_{liq}\right)$ is coefficient of agglomeration, which is a function of mass fraction of the liquid particles. A set of values $\alpha_{ij} = m_{agl}^{j} / m_{liq}^{i}$ is calculated by combining data about m_{liq}^{j} from the simulations with the data about mass fraction of agglomerated debris m_{agl}^{i} from DEFOR-A experiments. The coefficient of agglomeration α is defined as a curve which envelops the domain covered by the set of α_{ij} values, providing a bounding assessment which takes into account both uncertainties in mechanistic modeling of melt-coolant interaction phenomena and in the physical properties of the melt. The following enveloping assessment is made for the coefficient α ([5] [20][21] [22]):

$$\alpha\left(m_{liq}\right) = \begin{cases} 4 \cdot m_{liq}, & m_{liq} \le 0.5 \\ 1/m_{liq}, & m_{liq} > 0.5 \end{cases} \qquad \textbf{(2)}$$

We also consider formula (3) to assess how sensitive the predicted mass fraction is of agglomerated debris, in an experimental scale problem and in a plant scale analysis, to variations in enveloping assessment of α.

$$\alpha\left(m_{liq}\right) = \begin{cases} 25/4 \cdot m_{liq}, & m_{liq} \le 0.4 \\ 1/m_{liq}, & m_{liq} > 0.4 \end{cases} \qquad \textbf{(3)}$$

The goal of the validation performed in this work differs from the standard goal for validation of a best estimate code when a "best match" between experimental and simulation data is the aim. The method was validated against DEFOR-A data to demonstrate that it provides a robust bounding but physically reasonable assessment of the fraction of agglomerated debris despite the inherent uncertainties in the physical phenomena (e.g. jet breakup, steam production rate in the melt-coolant interaction zone) [5], [20], [22]. It was demonstrated that the most conservative estimate of the fraction of agglomerated debris for the DEFOR-A test conditions is predicted with Kelvin-Helmholtz (KH) jet breakup model. Two bounding assumptions in modeling of steam production rate were also examined. In the first case, denoted as "sat", all heat released by the melt goes to evaporation of the water (as in saturated water). In the second case, denoted as "sub", all heat released by the melt goes only to heating of water and all locally generated steam condenses immediately (as in deeply subcooled water).

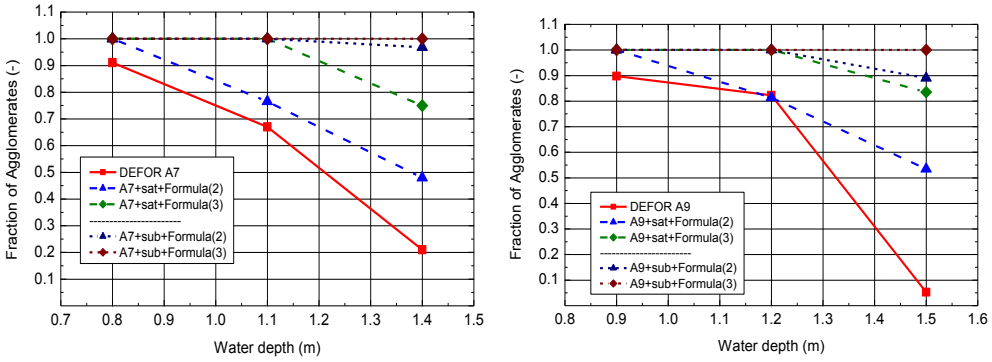

a) b)

Figure 3.21: *Validation against experimental data: a) DEFOR-A7; b) DEFOR-A9.*

The melt superheat is the most influential parameter for the fraction of agglomerated debris within the ranges of parameters considered in the DEFOR-A tests. The biggest values of the mass fraction of agglomerated debris are observed in DEFOR-A7 and DEFOR-A9 at about 200 K melt superheat. However, fraction of agglomerated debris reduces rapidly as a function of the water pool depth even in the test with high melt superheat. Example of validation results against DEFOR-A7 and DEFOR-A9 is shown in 3.21. The mass fractions of agglomerated debris from the DEFOR-A tests and from simulations are presented as function of water pool depth. It can be seen that predicted values of agglomerated debris provide conservative estimates while reducing rapidly with pool depth similarly to the experimental values.

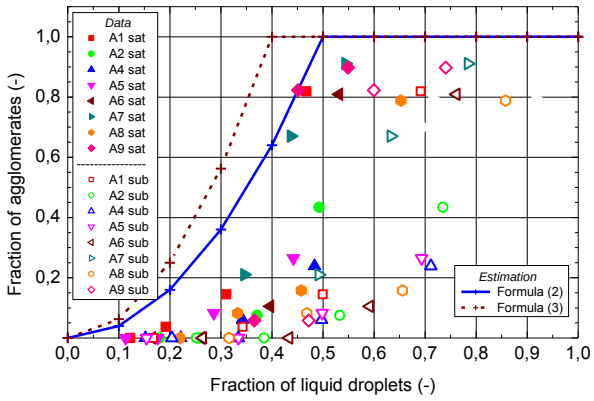

Figure 3.22: Conservatism in the estimation of the mass fraction of agglomerates. All cases are calculated with Kelvin-Helmholtz (KH) jet breakup mode: "sub" – "subcooled" water assumption; "sat" – saturated water assumption.

Figure 3.22 summarizes the data about dependency of mass fraction of agglomerated debris on the mass fraction of liquid particles obtained for all DEFOR-A tests and simulation conditions. Bounding estimates obtained according to (1) with the formulas for coefficient of agglomeration (2) and (3) are presented in Figure 3.22. It is clear that both formulas (2) and (3) provide enveloping estimates for the semi-empirical set of data on the mass fraction of agglomerated debris including the tests

with high melt superheat. We use formula (2) for analysis of agglomeration in the plant accident conditions.

Results of simulations for development of agglomeration mode map for a Nordic BWR accident conditions are presented in this section. Main parameters for the calculations are presented in Table 3.3. In addition, we use following assumptions in the modeling:

1) Fixed size distribution of the debris measured in DEFOR-A tests was used in the modeling in order to reduce the influence of epistemic uncertainty in the modeling of melt droplet fragmentation.
2) According to realistic geometry of a Nordic BWR the distance from the bottom of reactor vessel to the floor of reactor cavity was kept equal to 13 m. Thus height of the melt jet free fall decreases when the depth of the pool is increasing;
3) Prototypic geometry of the vessel lower-head is taken into account in assessment of the melt pool depth (1.75 m) according to the total mass of the pool (180 tons).

The influence of melt superheat on the fraction of agglomerated debris in reactor accident conditions was considered in [22]. Apparently, the influence of melt superheat on pre-deposition state of the debris and eventually on the fraction of agglomerates is not as big as in the DEFOR-A experimental conditions. The main reason is that in the plant accident conditions the ratio of solidification length to jet breakup length is considerably smaller than that for the DEFOR-A test conditions. Therefore, the effect of increase in the solidification length is much more visible in DEFOR-A tests, and less important for the plant.

Two correlations, that are considered in the present work, can be considered as a lower bound (Taylor correlation) and an upper bound (Saito correlation) respectively. Taylor correlation suggests that non-dimensional jet breakup length depends only on the ratio of the densities: $L/D = 5.3\sqrt{\rho_m/\rho_w}$, while Saito correlation takes into account the velocity of the jet at the entrance to the coolant: $L/D = 2.1\sqrt{Fr}\sqrt{\rho_m/\rho_w}$, where L - jet breakup length, D - diameter of the jet at the entrance to the coolant, ρ_m - density of the melt, ρ_w - density of the coolant, $Fr = u^2/gD$ - Froude number, u - jet velocity at the entrance to the coolant. Taylor correlation provides constant dimensionless length of the jet breakup for the plant accident conditions: L/D~14. Saito correlation predicts jet breakup length L/D~54, 45 and 32 for the jets reaching the bottom of 7, 9 and 12 m deep pools respectively. The difference between jet lengths calculated according to these correlations is about 6 m in case of 12 m pool. On the other hand, the distance between the leading edge of the jet and the depth at which agglomeration becomes negligible, for the plant accident conditions is about 1.5 – 2.0 m (Figure 3.23). It becomes obvious that epistemic uncertainty in jet breakup length is dominating. The main implication of the present results is that melt superheat has less significant contribution to the uncertainty in the debris agglomeration than jet breakup length. Liquid droplets, once formed, solidify quite fast. No significant agglomeration is expected if there is more than 2 meters between the leading edge of the melt jet and the top of

the debris bed. Results of the plant accident analysis obtained with Saito correlation are summarized in the form of the agglomeration mode map in Figure 3.23.

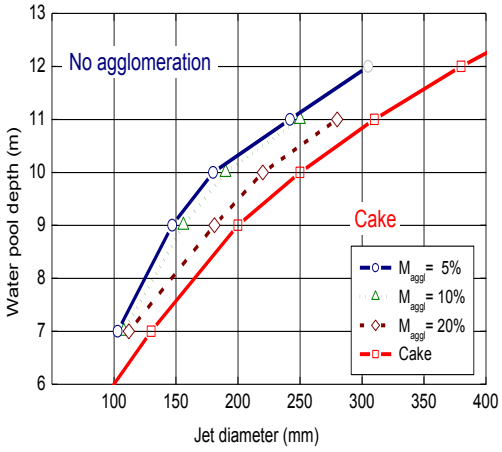

Figure 3.23: Agglomeration mode map.

Table 3.3: Plant accident conditions.

Pool parameters	**Value**
Diameter, m	9
Depth, m	7-12
Initial pressure, bar	1
Water temperature, K	373
Melt parameters	
Composition	Eutectic corium
Total mass, t	180
Initial temperature, K	3000-3200
Initial met superheat, K	200-400
Jet diameter, mm	50-300
Jet release height, m	1-6

In this work, a conservative-mechanistic approach to prediction of mass fraction of agglomerated debris has been further developed and validated against DEFOR-A tests data. Validated models along with conservative assumptions are used for development of an agglomeration mode map at different plant accident conditions (e.g. pool depth, initial jet diameter and melt superheat). Performed analysis suggests that debris bed formed few meters below the leading edge of the jet will be completely fragmented. It is concluded that epistemic uncertainty in the modeling of the jet breakup length is currently dominating over the other sources of epistemic and aleatory uncertainties. Further reduction of potentially excessive-conservatism in the jet breakup length and clarification of potential influence of the other sources of uncertainty (e.g. particle size distribution) is necessary.

3.3.4. Self-Organization Phenomena in Debris Spreading and Bed's Shape

Given the total mass of the material, the conditions for the occurrence of local dryout are contingent on the particle diameters, porosity, as well as on the debris bed shape. In particular, a tall mound-shaped debris bed would be more prone to dryout than a debris layer of the same volume uniformly spread over the pool basemat. For comprehensive assessment of coolability margins of an ex-vessel debris bed, it is required to develop a "map" of possible debris bed shapes. The map has to connect the melt release scenario parameters and the resulting shape of the bed. The most important scenario parameters are the timing and scenario of reactor pressure vessel (RPV) failure, ex-vessel melt relocation conditions, initial temperature and depth of the water pool in the lower drywell. There are many uncertainties in these parameters, so that parametric studies are necessary.

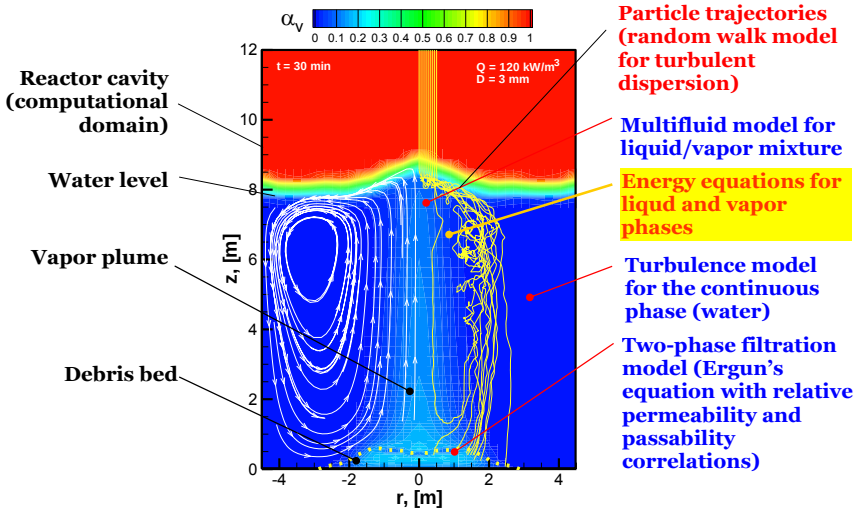

Figure 3.24: DECOSIM code models.

Development of a debris bed shape map, together with the studies on debris agglomeration, size distribution, porosity, friction laws and dryout incipience is a key element in the development of a generic "coolability map" needed for the issue resolution related to long-term ex-vessel coolability of reactor debris in the case of a severe accident. Current work addresses formation of a debris bed from gradually release corium particles in an initially subcooled water pool. For the Nordic BWR design, one of the severe accident scenarios to be considered is the gradual melt release, when the molten corium is released over a long time (hours). This case was studied recently by using a dedicated computer code DECOSIM (DEbris COolability SIMulator) developed at KTH [6], [7], [18]. The code implements the multifluid model for liquid-vapor flows in the heat-releasing debris bed, as well as in the volume of the pool. The following phenomena are taken into account (Figure 3.24) in the modeling: i) filtration of water and vapor in the porous debris bed with heat release; ii) turbulent natural convection flows in the water pool; iii) sedimentation of melt particles and their interaction with circulatory flow in the pool due to drag and turbulent dispersion; iv) fallout of particles, their packing, avalanche and growth of debris bed. To address the multiscale nature of the problem, a computationally efficient "gap-tooth" algorithm was developed to speed up considerably the simulations of long transients typical of gradual melt release mode.

Clarification of the overall effect of pool subcooling on particle spreading efficiency is the primary focus of this work. Detailed description of the DECOSIM models, closing relationships and numerical methods is given in [6][7][18]. Debris bed formation in DECOSIM simulations is governed by two mechanisms, namely, by particle avalanching and by lateral spreading of particles by the convective flows. While in a saturated pool the latter mechanism plays the predominant role (at least for particle sizes below 5 mm), both mechanisms can contribute to particle spreading in a subcooled pool.

The geometry used in calculations corresponds to the parameters typical of BWR designs adopted in Sweden. The pool diameter was taken equal to 11.4 m (which gives the effective pool area of 102 m^2), pool height 12 m, the initial fill level 7.6 m

(volume of water 884 m^3). The corium had the initial temperature $T_m^0 = 3000$ K, its thermophysical properties are $\rho_m = 8285.1$ kg/m^3, $c_{m,l} = 680.7$ J/kg K, $c_{m,s} = 566.2$, $\Delta H_f = 428$ kJ/kg, $T_m^M = 2811$ K. The porosity of debris bed was taken constant $\varepsilon = 0.4$. The particle size distribution assumed in the calculations was based on the data from different FCI experiments including DEFOR-A. Seven groups of particles with diameters ranging from 1 to 10 mm were specified, with the Sauter mean diameter equal to $\bar{D}_m = 2.6$ mm. For each particle sort, total of 10^4 representative particles were used in the Lagrangian model. The angle of repose for the debris bed was taken $\alpha_0 = 35°$ from the experiments for granular materials. It should be kept in mind that these experiments were performed for non-boiling setup. Boiling in the debris bed can lead to partial fluidization of particles and reduce the angle of repose by promoting the avalanching and gradual lateral spreading. Note that the debris bed height (and, as a consequence, bed coolability) is sensitive to the angle of repose, therefore, the result obtained for the above angle of repose are conservative.

Total of $M_m^0 = 200$ t of corium was released over the release time $t_0 = 1$ h. Melt was supplied by a source located on the top boundary (at the height 12 m), with Gaussian distribution of particle mass flux (the characteristic radius was 1 m, the flux was clipped at the radius 2 m). The initial temperature of water in the pool is an uncertain parameter because the pool can be heated by vapor condensation prior to melt release. Two initial subcoolings of the pool water, ΔT_w^0 = 20 and 50K (initial temperatures 353 and 323K) were used in the simulations.

The results obtained for the higher initial water temperature (353K) demonstrate the effects of feedback between natural circulation and the formation of debris bed. The fluid heated by the debris bed, as well as by the falling particles, rises upwards and spreads under the pool surface, reducing the subcooling in the top part of the pool. As a result, temperature stratification develops in the pool. As the water reaches saturation and boils up near the pool surface, the convection in the pool is intensified dramatically. Boiling distorts the horizontal pool surface as large amounts of vapor are generated.

After the pool boils up, the debris bed mostly grows laterally, rather than upwards. Thus, spreading of particles by the convective flows plays the predominant role at this stage. The radial distributions of debris bed height are shown in Figure 3.25 for the 50°C and 20°C subcoolings. One can see that the central cone-shaped part of the debris bed is formed on the initial (pre-boiling) stage of the process, whereas at the later stages the "wings" of the debris bed are formed due to the enhanced particle spreading. The time history of maximum debris bed height obtained in these calculations is presented in Figure 3.26 together with the case where the debris bed growth is governed solely by avalanching (dashed line).

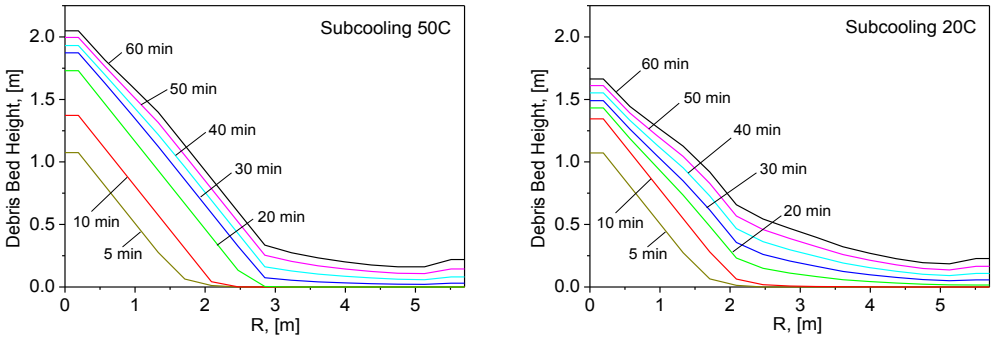

a) b)

Figure 3.25: Debris bed shape at different times for initial pool temperature (a) 50C and (b) 80C.

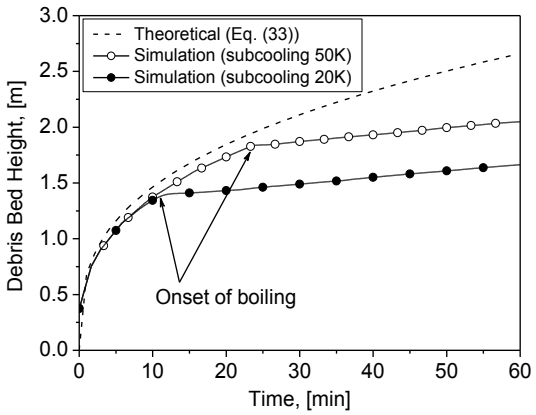

Figure 3.26: Maximum debris bed height for different subcoolings.

A tall mound-shaped configuration of the debris bed can be non-coolable. The results obtained in this work suggest that development of natural convection in an initially subcooled pool can affect the formation of debris bed in the case of gradual corium melt release. Intensive convective flows capable of spreading melt particles over the pool basemat start to develop as soon as local boil up of water in the upper stratified layer occurs. Such spreading of the debris effectively limits the maximum height of the debris bed and helps to prevent the formation of non-coolable configurations. However initial subcooling of the pool affects timing of the onset of boiling and large scale circulation and thus maximum height of the debris bed. This phenomenon can be considered in development of severe accident managment guidelines and procedures. Further research is needed to obtain the complete debris bed shape map depending on various problem parameters, and to estimate the implications of particle spreading on debris bed coolability in the initially subcooled water pool.

Results of application of DECOSIM code to reactor accident conditions show that particulate debris spreading in the pool can be hindered at high initial subcooling of water leading to formation of a tall mound shape bed. However, there is another

mechanism of particulate debris spreading which takes place after settlement of the debris at the bottom of the pool. There is so called "self-leveling" of the debris which occurs in case of boiling inside the debris bed. Intensive boiling promotes slow motion of granular media which gradually changes the shape of the bed. If melt release from the vessel is sufficiently long to achieve significant reduction of the debris bed height, then self-leveling can be credited as additional factor which enhances formation of a coolable debris bed.

Figure 3.27: PDS: Particulate Debris Spreading experiment.

A new experimental facility PDS (Particulate Debris Spreading) has been designed and commissioned at the division of Nuclear Power Safety, KTH. The goal of the experiment is to assess the time scale for particulate debris spreading by self-leveling mechanism and to provide experimental data for development of analytical models for prediction of particulate spreading. Compressed air is injected from the bottom of the debris bed in order to simulate boiling and two-phase flow inside the bed. First series of PDS exploratory tests have been performed with 6 L (30kg) of stainless steel particles. The purpose of the tests was to check effect of the 2D and 3D shapes on particulate debris spreading. Qualitative results of the tests are illustrated in Figure 3.27. On the left results of a 2D test on particulate debris spreading, from top to bottom initial shape, gas injection, final shape of the bed; on the right results of a 3D spreading test, from top to bottom initial and final shape of the bed. Further experimental investigations are necessary for model development and validation.

3.3.5. Sensitivity and Uncertainty Analysis for Debris Bed Coolability

From the reactor safety point of view, it is important not only to obtain the conditions at which debris bed dryout can occur, but also to assess the uncertainties related to (i) intrinsic variability of debris bed properties (i.e., particle size and porosity), which generally depend on melt ejection conditions (including pressure in the containment) defined by the plant accident scenario; and (ii) deficiencies and incompleteness of the models used for prediction of coolability (e.g. drag laws for two-phase flow in porous media) [23]. If formation of a non-coolable debris bed cannot be ruled out, then the risk (probability) of such event has to be demonstrated as sufficiently low, given the uncertainties in the accident scenario (aleatory) and in the modeling (epistemic). If uncertainties are large, then one way for solving such problem is to perform further studies to reduce the uncertainty in risk assessment.

In this work, global sensitivity analysis based on the Morris diagrams and Sobol sensitivity indices is applied in order to rank the importance of different input and model parameters and to quantify the influence of physical factors on the uncertainty in prediction of dryout heat flux and pressure drop in top-fed and bottom-fed debris beds. We also discuss results of the optimization of the coolability models for better prediction of the available experimental data. Finally we show the sensitivity of the coolability margins to the uncertainty in the ranges and distribution of the input parameters and suggest the research objectives that have highest return in terms of reduction of uncertainty in assessment of coolability.

The classical simplification used to obtain the critical coolability conditions at given (assumed) properties of the bed was to consider a uniform flat debris bed in saturated water (top-fed debris bed), with counter-current flows of water (flowing down) and vapor (flowing up), or a bottom-fed debris bed with vertical water inflow through the bottom boundary. In the one-dimensional case, the critical conditions are conveniently expressed in terms of the Dryout Heat Flux (DHF), or the heat release rate per unit area of debris bed top surface. A number of experiments aimed at obtaining the relationship between the DHF and debris bed parameters, i.e., mean particle diameter, porosity, has been carried out. In these experiments, either the pressure drop in the debris bed was obtained, or conditions at which dryout zones occur in the debris bed were measured directly and compared with the predictions of different models. Since the two-phase flow in the debris bed is governed by drag and gravity, different values of DHF are obtained from different drag models.

The traditional scheme for the determination of dryout conditions in a flat debris bed is mainly based on the one-dimensional momentum equations:

$$-\frac{dP}{dz}-\rho_L g=\frac{\mu_L}{KK_{rL}}\,j_L+\frac{\rho_L}{\eta\eta_{rL}}\left|j_L\right|j_L-\frac{F_i}{1-\alpha} \tag{4}$$

$$-\frac{dP}{dz}-\rho_G g=\frac{\mu_G}{KK_{rG}}\,j_G+\frac{\rho_G}{\eta\eta_{rG}}\left|j_G\right|j_G+\frac{F_i}{\alpha} \tag{5}$$

Here, g is the gravity acceleration, ρ_i and μ_i are the phase densities and viscosities ($i=L,G$). The relative permeabilities K_{ri} and passabilities η_{ri} as functions of the void fraction α are described by the power-law relations in the "classical" models:

$$\begin{aligned} K_{rL}&=(1-\alpha)^{nL}, \quad \eta_{rL}=(1-\alpha)^{mL}\\ K_{rG}&=\alpha^{nG}, \quad \eta_{rG}=\alpha^{mG}\end{aligned} \tag{6}$$

Of the models which explicitly take into account the interphase drag, the one by Schulenberg and Müller is considered here:

$$K_{rL}=(1-\alpha)^{nL}, \quad \eta_{rL}=(1-\alpha)^{mL}, K_{rG}=\alpha^{nG}, \quad \eta_{rG}=\begin{cases}0.1\alpha^{mGL}, & \alpha\le\alpha_*\\ \alpha^{mGH}, & \alpha>\alpha_*\end{cases} \tag{7}$$

$$F_i=C_{SM}(1-\alpha)^{nSM}\,\alpha\,\frac{\rho_L K}{\eta\sigma}\,g(\rho_L-\rho_G)\left|j_r\right|j_r,\ C_{SM}=350,\ nSM=7 \tag{8}$$

where $nL=3$, $mL=5$, $nG=3$, $mGL=4$, $mGH=6$, the boundary between two regimes for the gas passability is $\alpha_* = 0.1^{1/(mGH-mGL)} = 0.1^{1/2} \approx 0.316$, σ is the coefficient of surface tension at liquid-vapor interface, $j_r = j_G/\alpha - j_L/(1-\alpha)$ is the relative phase velocity.

The dryout heat flux and pressure drop depend on the properties of porous medium and operating conditions. In application to reactor safety, these parameters are accident scenario-dependent. The particle size and morphology distributions (which together define the porosity of the bed) are affected by both the scenario of melt release and inherent uncertainties in fuel-coolant interaction phenomena. As there is a significant dependence of these input parameters on stochastic features of accident scenarios, therefore in this study we treat them as *aleatory* uncertainties by defining respective probability density distributions.

On the other hand, the mathematical model (4) - (7) that predicts the dryout heat flux at given operating conditions and properties of the debris bed involves a number of constants. These constants were obtained from a limited number of experiments and often differ between different authors, even for the same functional form of closing relationships. In this work, we consider these model coefficients as *epistemic* uncertainty in knowledge about physical phenomena determining the dryout heat flux. Traditionally, the models of different authors are taken "as is" in terms of the constants involved, and then their predictions are compared to some experimental data to see which model is more adequate. Here, an alternative approach is taken: the functional form of the closing relationships (4) - (7) is maintained, however, the parameters involved are considered as variable in certain ranges, rather than numerical constants. The main idea behind this is to clarify which model parameters are the most influential, and to see if such a "generic" model can be optimized against a large set of experimental data. The ranges of physical and model parameters relevant to assessment of debris bed coolability are summarized in Table 3.4. Detailed discussion of these parameters is given in [23].

Sensitivity and uncertainty analysis was performed by running Cool1D code for prediction of DHF and pressure drop coupled with DAKOTA, Version 5.0 package. To enable communication between the programs, appropriate interface scripts were developed. Screening sensitivity analysis was carried out [23] by the Morris method that allows one to determine factors which have (a) negligible, (b) linear and additive, or (c) non-linear effects or involved in interactions with other factors. In Figure 3.28, the Morris diagrams are presented for DHF in a top-fed debris bed for the model and physical parameters listed in Table 3.4. Results are shown for the "classical" model (a) and Schulenberg and Müller's model (b), the model parameters are plotted by black and white points, the physical parameters are given in color. One can see that the most influential (i.e., having the largest value of μ^*) *model* parameters are the exponents in the relative phase passabilities *mL* and *mG* (Table 3.4). This means that, in the conditions close to dryout, the flowrates are high and the quadratic (passability-related) terms are the main contributors to the total drag.

Sensitivity studies enabled ranking the model parameters with respect to their influence on DHF and pressure drop. The least influential parameters can be fixed at

some values, while the most influential ones can be optimized against the relevant experimental data.

Table 3.4: Parameter ranges.

Parameter	**Description**	**Range**
P_{sys}	System pressure, bar	1-4
d	Mean particle diameter, mm	1-5
ε	Porosity, [-]	0.35-0.5
nL	Exponent in relative permeability K_{rL}	2-4
mL	Exponent in relative passability η_{rL}	3-7
nG	Exponent in relative permeability K_{rG}	2-4
mG	Exponent in relative passability η_{rG}	3-7
C_{SM}	Constant in interphase drag for SM model	200-500
nSM	Exponent in the drag force in SM model	6-9
mGL	Exponent in η_{rG} for low void in SM model	3-4
mGH	Exponent in η_{rG} for high void in SM model	4-7

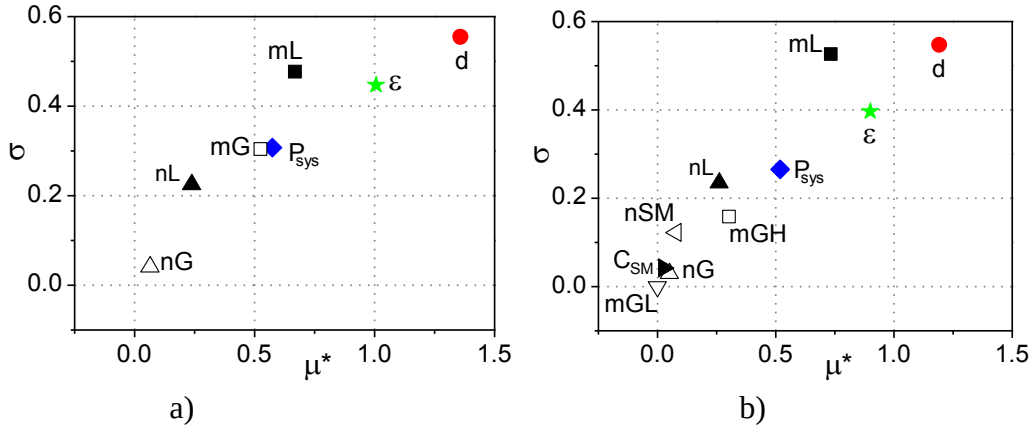

Figure 3.28: Morris diagrams for DHF in a top-fed debris bed: (a) classical models, (b) Schulenberg and Müller's model.

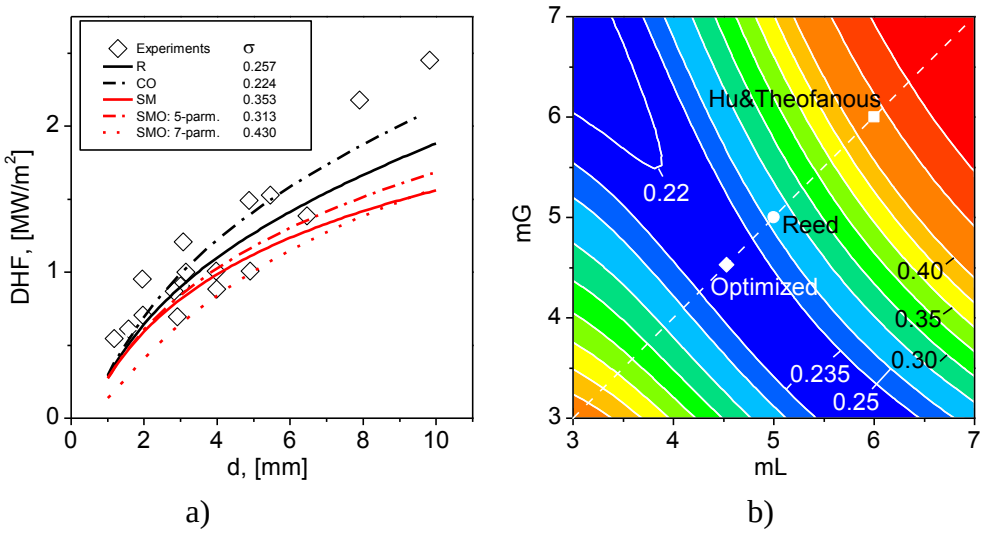

Figure 3.29: Optimization of models on DHF for top-fed debris bed: (a) comparison with experimental data; (b) standard deviation σ on the (mL, mG) plane.

An attempt was undertaken to find the optimum values for relative passability exponents *mL* and *mG* in the classical model which would provide the best fit to the experimental data on DHF as a function of particle diameter (Figure 3.29). It turned out, however, that the optimization problem is ill-posed. This could be interpreted as the same DHF can be achieved by increasing the porous drag by one or another phase. Here, in line with all "classical" models, it was assumed that the exponents for both phases are equal. In this case, the optimum value can be easily found along the diagonal of the graph in Figure 3.29b.

Optimization of Schulenberg and Müller's model was performed using the pressure drop data from total of 13 experiments (see details in [23]). In the first optimization run, five model parameters listed in Table 3.4 were varied, except the fixed *nL* = *nG* = 3. In the second run, seven model parameters (including *nL* and *nG*) were varied. In Figure 3.30, the standard deviations σ are plotted for each experiment (parameters are listed to the right of the graph) obtained for the original Schulenberg and Müller's model and its optimized versions.

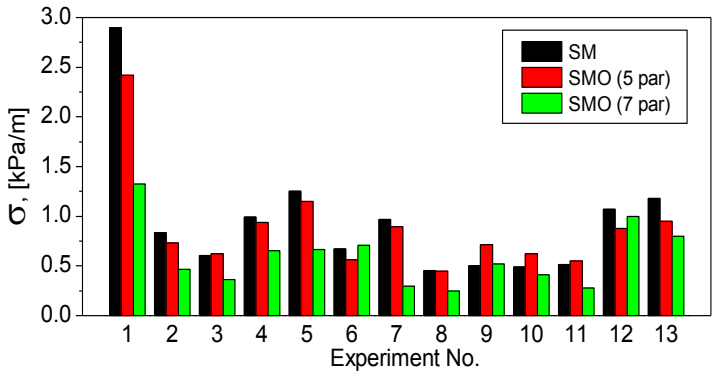

Exp.	d	j_{LB}	P_{sys}
1	6	7.2	1
2	6	2.9	1
3	6	0	1
4	3	7.2	1
5	3	2.9	1
6	3	0	1
7	6	7.2	3
8	6	2.9	3
9	6	0	3
10	6	0.2	1
11	6	0.5	1
12	3	0.2	1
13	3	0.8	1

Figure 3.30: Optimization of Schulenberg and Müller's model on experiments [45]: standard deviations for each experiment are shown for the original model (SM), and optimized model (SMO) with 5 and 7 variable parameters.

While the above optimization improved the agreement with experimental data on pressure drop, it is important to see what effect it had on the DHF prediction. The dependencies of DHF on the particle diameters calculated with the optimized parameters are plotted in Figure 3.29a. Evidently, the parameter set obtained in 7-parameter optimizations gives underestimated DHFs due to the increased porous drag of phases caused by increased relative permeability exponents. The 5-parameter optimization, however, gives better agreement than the original SM model, however, the deviation is still larger than for Reed's and optimized classical models.

Consider now the uncertainties in the DHF caused by the uncertainties of the *physical* parameters (d, ε, P_{sys}). The cumulative distribution functions (CDF) for the dryout heat flux obtained by the Monte Carlo sampling of the three physical parameters in the ranges listed in Table 3.4 are presented in Figure 3.31a [23]. In Table 3.5, the values of DHF corresponding to 5% CDF are listed for different models and inflow velocities. These values can be regarded as lowest coolability limits which will be exceeded with 95% probability, given the ranges of physical parameters assumed in Table 3.4. Importantly, the discrepancy between predictions of different drag model are small for this quantity (within 6% for top-fed debris bed and within 0.5% for bottom-fed).

For better understanding of the effect of uncertainties in the physical parameters, it is necessary to determine what fraction of DHF variance is attributed to each of them. The total Sobol sensitivity indices S_{Ti} show by what fraction the variance of DHF will be reduced if the i-th parameter is fixed (its uncertainty is eliminated). In Figure 3.31 the Sobol total sensitivity indices are presented for the top-fed and bottom-fed debris beds (model CO). One can see that about 63-76% of the DHF variance is due to the uncertainty in particle diameter, 40-63% due to porosity. System pressure uncertainty gives 23-49% input into DHF variance for inflow velocities up to 1 mm/s, while for $j_{LB} = 2$ mm/s the input of system pressure increases to 75%.

Results of sensitivity and uncertainty analysis presented in this work suggest that:

- Contribution of epistemic uncertainty in drag laws to the DHF uncertainty appears to be minor in comparison with contribution of uncertainty in the parameters.
- Effective particle diameter has the largest Sobol sensitivity indexes for given ranges and uniform distribution of the input parameters.

Thus the most effective way for reduction of the uncertainty in the DHF would be reduction of uncertainty in the ranges and distribution of effective particle size.

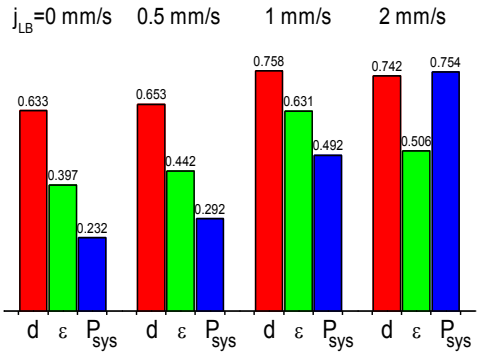

Figure 3.31: Sobol total sensitivity indices S_{Ti} for DHF

Table 3.5: Table 3.3 DHF (MW/m^2) at CDF = 5%

Model	$j_{LB}=0$	0.5	1.0
R	0.547	1.070	2.023
CO	0.583	1.073	2.028
SM	0.508	1.064	2.017
SMO	0.515	1.065	2.023
Mean/ σ	0.539/ 0.034	1.068/ 0.004	2.023/ 0.005

Sensitivity analysis and optimization of model parameters allow one to obtain better agreement between the predictions and experiments. However, "blind" optimization of all model parameters with respect to a chosen set of data can deteriorate predictions of other quantities, as was demonstrated by optimization of drag models on the pressure drop experiments which resulted in worse prediction of DHF. For the chosen debris bed parameters, it was shown that the model-to-model differences are noticeable on the cumulative distribution functions. However, the lower coolability boundary, corresponding to 5% of cumulative distribution function of DHF, is predicted by all models in quite narrow range. In the future, it will be important to assess the modeling uncertainties in evaluation of the coolability margins for 2D and 3D configurations of the debris beds.

3.4 Debris Coolability (POMECO)

3.4.1. Motivation

The objective of POMECO subproject is to assess the coolability of a debris bed formed in FCI during a postulated severe accident of LWRs. To assess debris bed coolability, a great number of analytical models have been developed for prediction of single/two-phase flow (friction) and heat transfer (dryout heat flux) in particulate beds. It is generally accepted that the frictional pressure drop of single-phase flow in porous media can be predicted by the Ergun equation:

$$-\frac{dp}{dz}=\frac{\mu}{K}J+\frac{\rho}{\eta}J^2=150\frac{(1-\varepsilon)^2\mu}{d^2\varepsilon^3}J+1.75\frac{(1-\varepsilon)\rho}{d\varepsilon^3}J^2 \qquad (9)$$

The Ergun equation can be adapted to the case of two-phase flow through the particulate beds by introducing relative permeability K_r, relative passability η_r, and interfacial friction F_i (see Eqs. (4)-(8)). Such approach was adopted in the classical models for dryout heat flux (see Table 3.4). For these models, the central point is to provide the formulations of K_r, η_r and F_i in the momentum equations, based on experimental data. From the models one can see the particle diameter is one of the key parameters in the determination of frictional terms. A debris bed formed from FCI during a severe accident tends to be packed with particles of varied sizes and shapes

(see DEFOR section). Thus, the first task of POMECO research is to determine a proper mean diameter for the debris particles (called "effective particle diameter") which can be used in the model(s) for coolability analysis.

The second task of POMECO research is to obtain the dryout heat fluxes of the particulate beds packed with various particles, and to investigate how the mode of water ingress (top-flooding or bottom-fed by a downcomer or forced injection) affects the dryout heat fluxes. This study gives ideas for coolability enhancement measures and provides data for the validation of coolability analysis codes.

The third task of POMECO research is to investigate the influence of a "cake" on the debris bed coolability. This activity is motivated by the past FCI tests where particles can be agglomerated or even an impermeable "cake" (a chunk of non-fragmented melt) can form in the debris bed. Detailed experimental study of the debris agglomeration has been performed in the DEFOR-A experiment (see the preceding section).

The fourth task of POMECO research is an analytical support to the experimental tasks, by using coolability simulation tools (e.g., MEWA and DECOSIM codes). The idea is to interpret the experiment as well as validate the tools. Finally, the tools are employed to perform coolability analysis for an ex-vessel debris bed in a hypothetical severe accident of BWRs.

Two test facilities, namely POMECO-FL and POMECO-HT, were designed and constructed at KTH to investigate frictional drags of adiabatic single/two-phase flow in porous media and dryout heat flux of volumetrically heated particulate bed, respectively.

3.4.2. Test Facilities

Figure 3.32a illustrates the schematic diagram of the POMECO-FL test facility. The test section accommodating the packed bed is made of a Plexiglas pipe of 90 mm in inside diameter and 635 mm in height. Air and water are supplied from the bottom and flows up through the packed bed. Detail information about POMECO-FL facility can be found in [26].

The schematic of the POMECO-HT facility is shown in Figure 3.32b, which consists of test section, water supply system, electrical heaters and their power supply system, instrumentation (thermocouples, flow meters and pressure transducers) and data acquisition system (DAS). The test section for accommodating the particulate bed and heaters is a stainless steel vessel whose cross-sectional area is 200mm×200mm rectangular with the height of 620mm. A total number of 120 electrical resistance heaters and 96 thermocouples are uniformly distributed in the particulate bed. The facility has a high power capacity (up to 84 kW) which enables to reach the coolability limit (dryout heat flux) of particulate beds within a broad range of porosity and particle diameters as well as coolability-enhanced measures such as bottom injection of water. More information about POMECO-HT facility can be found in [27]. In addition to calibration of instrumentation, the test facilities and its measurement system are qualified by measurements of single-phase flow through a bed packed with single-size spheres. The quality of experiment can be ensured by the good agreement [26].

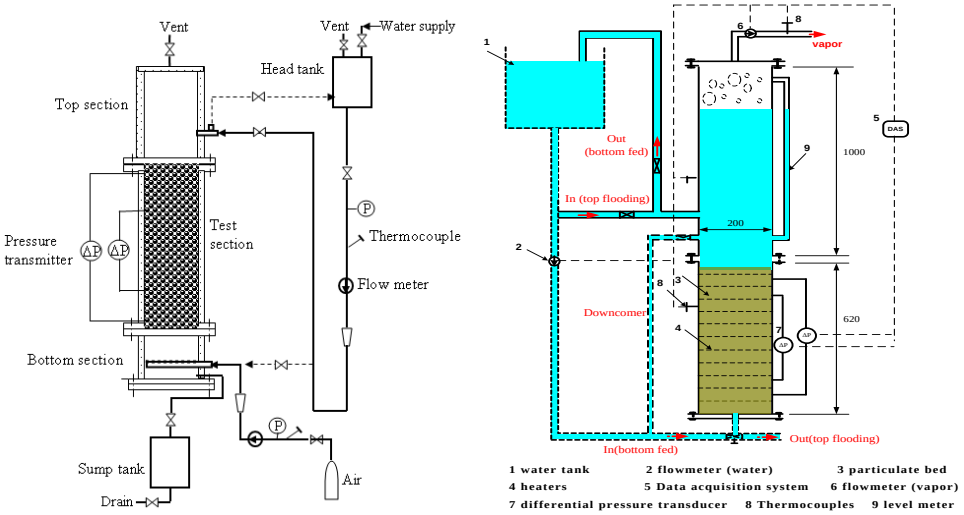

(a) (b)

Figure 3.32: Schematic diagrams of (a) POMECO-FL facility and (b) POMECO-HT facility.

3.4.3. Effective Diameter of Bed Packed with Multi-diameter Spheres

In this study, the pressure gradient was measured on the POMECO-FL facility, when the single-phase flow through the bed packed multi-diameter spheres, and then the effective diameter of the particles which form the bed was obtained, by applying the Ergun's equation. Comparison of the effective particle diameter with various mean particle diameters is provided, so as to guide the selection of a proper mean particle diameter for coolability analysis.

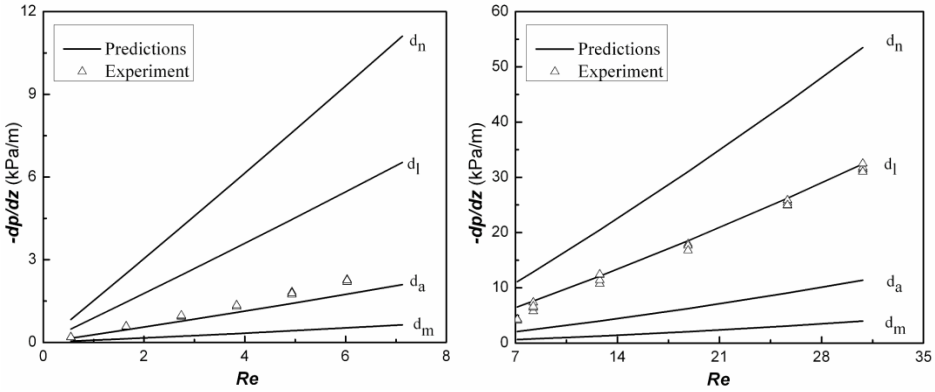

(a) at low Reynolds number *(b) at high Reynolds number*

Figure 3.33: Pressure gradients of bed packed with multi-diameter spheres with a size distribution similar to debris particles of FCI tests [26].

Serial tests with beds consisting of different size of spheres were performed on the POMEOCO-FL facility. The results show that at low flowrate (*Re*<7) the effective particle diameters can be represented by the area (Sauter) mean diameters of the particles in the beds, while at high velocity (*Re*>7) the effective particle diameters are closer to the length mean diameters, as shown in Figure 3.33. More information can be found in [26]. Figure 3.34 shows the pressure gradients of two-phase flow

through a particulate bed with multi-diameter spheres whose effective diameter is also plotted in the figure, together with the experimental data. It can be seen that the prediction of Reed model has a good agreement with the experimental data if Sauter mean diameter is used as effective particle diameter.

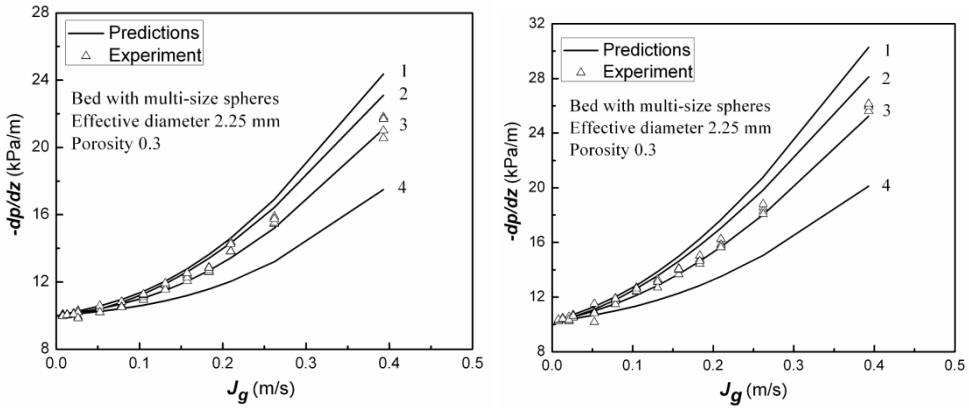

(a) J_l=0.13 mm/s *(b) J_l=0.26 mm/s*

1–Hu & Theofaneous (1991); 2–Schulenberg & Műller (1987); 3–Reed (1982); 4–Lipinski (1982).

Figure 3.34: Pressure drops of air/water two-phase flow through a bed packed with multi-diameter particles [28].

3.4.4. Effective Diameter of Bed Packed with Non-Spherical Particles

Experiment was carried out on POMECO-FL facility to examine the applicability of the Ergun equation to flow resistance assessment for packed beds with non-spherical particles such as spheres with through-holes or cylindrical particles. It was found that the pressure drops in the packed bed are much higher than the predictions of the Ergun equation if the diameters of the spheres and cylinders are employed in the equation.

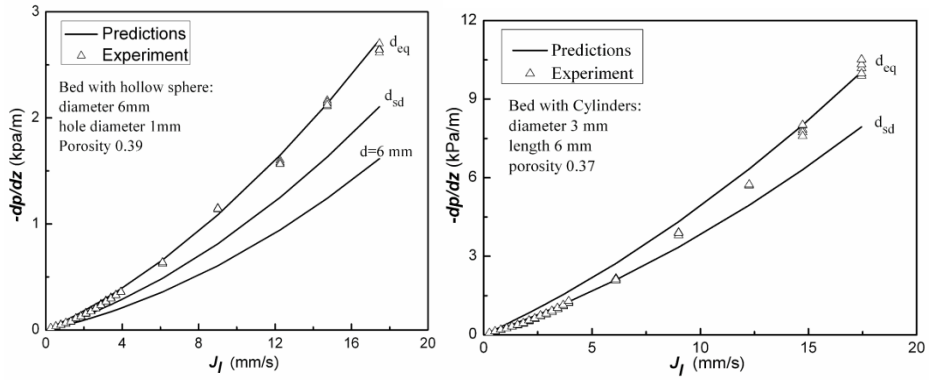

(*a) 6mm spheres with 1mm through-holes* *(b) Cylinders, 3mm (diameter)*6mm (length)*

Figure 3.35: Pressure gradients in Beds packed with non-spherical particles.

The other models (e.g., using Sauter mean particle diameter in the Ergun equation or modifying the Ergun constants) could not predict the measured pressure drops either. However, the Ergun equation is capable of predicting the experimental data for all the test beds if the effective particle diameter used in the equation is chosen

as the equivalent diameter of the particles, which is the product of Sauter mean diameter and shape factor of the particles in each bed, as illustrated in Figure 3.35. Details of the study were reported in [29].

It should be noted that the debris particles from FCI are multi-size and irregular in shapes (see DEFOR section). It is not a trivial task to obtain their effective diameter through sieved mean diameters. For the DEFOR debris particles whose size distribution is as illustrated in Figure 3.36a, what we did was to load the particles in the POMECO-HT facility and measure the pressure drops of water flow through the debris bed. The effective particle diameter for the debris is estimated to be 1 mm, based on the pressure drop data and the bed's porosity of 0.45.

Dryout Heat Flux of Particulate Beds with Multi-Diameter Particles

Experiment was carried on the POMECO-HT facility to obtain the dryout heat fluxes of particulate beds packed with multi-diameter particles, which is the limiting parameter of particulate bed coolability. For a bed packed with multi-diameter spheres whose size distribution is shown in Figure 3.36a, the dryout heat flux of the bed under top-flooding condition is shown in Figure 3.36b. The effective particle diameter is 2.25mm and the porosity of 0.29. The dryout heat flux is most close to the prediction of the Reed model.

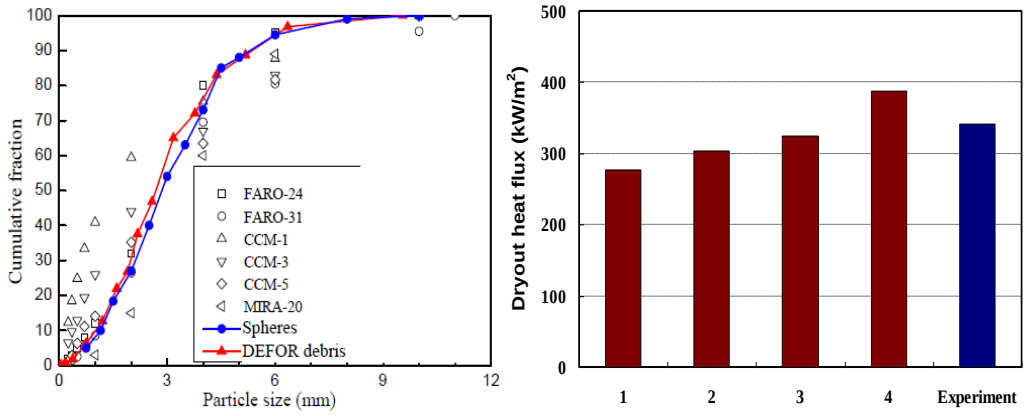

(a) (b)

Figure 3.36: Size distributions of particles in the test bed (a) and (b) dryout heat flux measured and predicted by various models for the top-flooding bed (1–Hu & Theofaneous (1991); 2–Schulenberg & Műller (1987); 3–Reed (1982); 4–Lipinsk (1982).).

Tests with forced injection of water from bottom were also performed. Compared with the top-flooding case, the bottom injection increases the dryout heat flux significantly, and the dryout heat flux rises with increasing water velocity of bottom injection. The dryout heat flux of the bed can be more than double of that in top-flooding case, if the superficial velocity of water injection is greater than 0.21 mm/s. More details of the study can be found in [30]. The forced injection tests were performed to obtain the relationship between the dryout heat flux and the bottom-fed flowrate, which can be used to guide the design of back-fitting for coolability enhancement.

3.4.5. Influence of Downcomer on Dryout Heat Flux

The effect of bottom water ingression on coolability is also investigated by natural circulation through a downcomer which connects the bottom of the bed to the water pool atop in the POMECO-HT facility. In reality, the downcomer represents a hypothetical retrofit device or coolant access to the bottom of a heap-like bed, which enhances the coolability of the bed. Two downcomers with the diameter of 8 mm and 12 mm internal diameter are employed separately, for the particulate bed packed with same multi-diameter spheres as above. The test results show that compared with top-flooding case, the dryout heat flux is enhanced 31% and 39% by 8-mm and 12-mm downcomer respectively [30].

3.4.6. Effects of Cake-Simulant on Dryout Heat Flux

In this study the effect of debris agglomeration and cake formation on debris coolability is studied by embedding a cake-simulant in a particulate bed. Basically two beds dubbed Bed-A and Bed-B are employed and both are packed with sand particles. The feature of Bed-B is a cake-simulant region embedded in the upper part of the bed. The cake-simulant is formed by a fine-particle (<0.5mm) layer surrounded from the top and the bottom by an aluminum foil. The thickness of the cake is 30 mm with the cross-sectional area of 160×160 mm^2. The mean diameter of the sand particles employed in the particulate beds is 1.75mm obtained by a companion test performed on the POMECO-FL facility. The porosity of the two beds is 0.37. More information is available in [31]. The dryout heat flux of top-flooding Bed-A is 450 kW/m^2 which is very close to the prediction of the Reed model. The dryout heat flux for Bed-B is 198 kW/m^2. In comparison with Bed-A, the dryout heat flux of Bed-B is significantly decreased (less than 50% of that in Bed-A) at top-flooding condition**.** This implies that the existence of non-fragmented melt chunk in the debris beds will deteriorate the debris coolability.

3.4.7. Coolability Analysis using Simulation Tools

In this study the MEWA code, developed at Stuttgart University for simulating transient behavior of debris bed formed in severe nuclear reactor accidents of LWRs, was employed to calculate the experiments performed on the POMECO-HT facility, with the objective to interpret the experimental data and validate the code. The code is then applied to coolability assessment for ex-vessel debris beds related to severe accident scenarios of a boiling water reactor (BWR). The characteristics of a prototypical debris bed, such as multidimensionality and higher porosity are emphasized in this study.

For the bed with an 8-mm-ID downcomer as in Section 4.6, the dryout heat flux predicted by the MEWA code is 428 kW/m^2, which is 4.5% lower than the experimental value (448 kW/m^2). Figure 3.37b shows the profiles of liquid velocity and particle temperature in the debris bed after dryout is initiated. It is observed that the water enters the bed mainly at the bottom of the bed through the downcomer. The dryout begins at the elevation of ~400 mm, which is just a little bit lower than the experimental value (438 mm). If the inside diameter of the downcomer increases to 12 mm, the dryout heat flux predicted by the MEWA code is 468 kW/m^2, which is comparable with the experimental value (475 kW/m^2), and 9% higher than that of the bed with an 8-mm-ID downcomer (428 kW/m^2). It appears that the gain in the dryout heat flux is not proportional to the increase in flow area of the downcomer,

since the flow area of the 12-mm tube is 2.25 times of that of the 8-mm tube. This means there is a threshold value for the downcomer size, above which the further coolability enhancement will be dismissing. The reason is that in this case the flow is governed by the resistance in the particulate bed. More calculations for POMECO-HT tests can be found in [32].

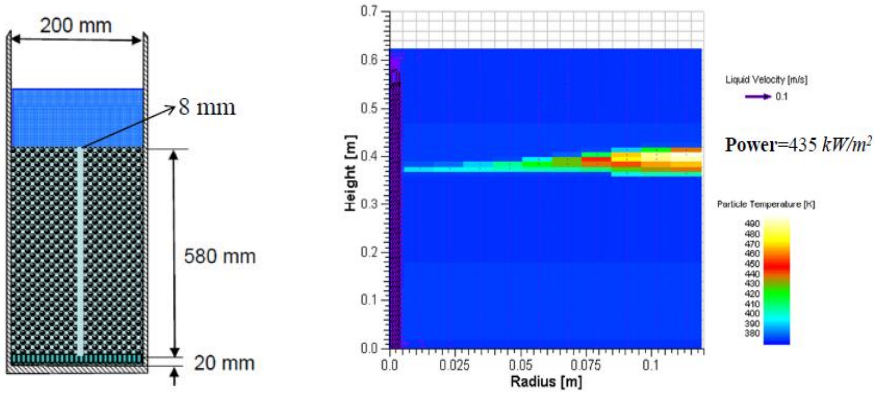

(a) bed in simulation *(b) temperature profile*

Figure 3.37: Dryout of the glass sphere bed with an 8-mm-ID downcomer.

For application of the MEWA code to coolability analysis of a prototypical-scale debris bed, we investigate the effect of debris bed configurations. The analysis is performed for an ex-vessel debris bed formed in the reactor cavity flooded with water. The rector has the thermal power of 3900 MW and the cavity diameter of 12 meters (see Figure 3.38). The maximum mass of the corium melt ejected to the reactor cavity is 256000 kg, with the solid volume of 29.1 m^3 (without void). The depth of the water pool in the cavity is 8 meters, and the melt is assumed to be well fragmented in the deep water pool due to FCI.

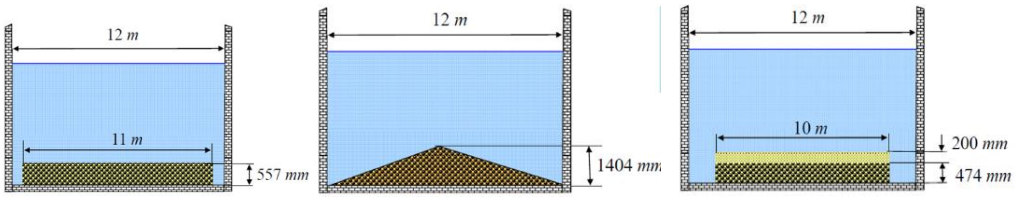

(a) cylindrical ***(b) heap-like*** ***(c) stratified***

Figure 3.38: Configurations of an ex-vessel debris bed.

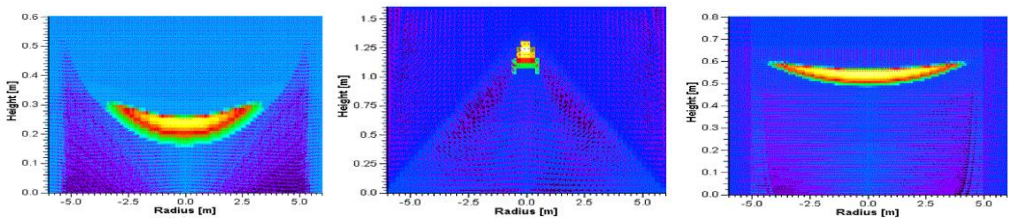

(a) cylindrical bed ***(b) heap-like bed*** ***(c) stratified bed***

Figure 3.39: Temperature profiles of the various debris beds as shown in Figure 3.38.

In the previous study [2], the effective particle diameter of ex-vessel debris beds is assumed as 3 mm and the bed's porosity as 0.4. However, the recent works [1][3]

indicate the porosity tends to be higher than 0.4, while the effective particle diameter is smaller than 3 mm. Based on the data of DEFOR debris as shown in Section 4.4, here the effective particle diameter of the ex-vessel debris beds are chosen as 1 mm and the bed's porosity as 0.45. If the pressure in the containment is 1 bar and the water in the cavity is assumed to be saturated (long-term coolability), the dryout power density of top-flooding such bed is 910 kW/m^3 predicated by the MEWA code. Since the decay heat is within the range of 0.5~1% the thermal power of the reactor, which is 375~750 kW/m^3 in term of the debris bed volume, the debris bed is coolable by only top-flooding (i.e., the debris particles evenly spread over the entire floor of the cavity, to form a bed with 1D counter-current flow in it). The coolability margin is getting smaller for the high decay case.

What if other configurations of the debris beds are formed to allow multi-dimensional flow? A few of representative beds are as shown in Figure 3.38 where Figure 3.38a represents a scenario where the debris does not occupy the entire floor of the cavity, leading to an annular gap between the bed and the cavity wall. In this case, the dryout power density is 956 kW/m^3, 9% higher than that of the top-flooding bed, due to water supply from the annular to the bottom of the bed. The gain in coolability appears marginal since the large diameter of the bed prevents the side coolant from flowing into the center of the bed. For the bed with a heap-like shape (cone) as shown in Figure 3.38b, the dryout power density is 535 kW/m^3. Surprisingly, instead of increase in dryout power density, it decreases by 41%, compared with the value of the top-flooding bed (910 kW/m^3). This is because the heap-like bed has the height of around three times the top-flooding bed, given the same mass of the debris. The special geometry results in a high void zone near the tip of the cone, where dryout occurs first. Notably, due to the high rate of steam flow through the tip, the dryout zone and its temperature do not vary rapidly with increasing power load. In other words, the steam flow plays a role in coolability. An axially stratified debris bed with a fine-particle layer settle atop a larger-size particle layer is considered (see Figure 3.38c). The coolability of such bed is determined by the top layer in top-flooding scheme, since the capillary force across the interface of the two layers prevents coolant from reaching the lower layer. Such a barrier, however, can be alleviated if coolant is supplied from the bottom through the annular gap as shown in Figure 3.38c where it is assumed that a 200-mm-thick layer with 0.5-mm-diameter particles sits atop a 474-mm-thick layer with 1-mm-diameter particles. The porosity is 0.45 for both layers. The dryout power density is calculated to be 356 kW/m^3, which is 63% higher than the values (218 kW/m^3) of the top-flooding bed packed with the 0.5-mm-diameter particles.

The dryout positions for the three beds can be seen in Figure 3.39. The co-current two-phase flow in the multi-dimensional beds raises the vulnerable location of dryout upward.

3.4.8. Implications to Reactor Safety

The experiments performed on the POMECO-FL and POMECO-HT test facilities provides the data for the effective particle diameters of particulate beds packed with multi-size and irregular particles. For a particulate bed packed with multi-diameter spheres, the friction law of two-phase flow in the bed can be represented by the Reed model using the Sauter mean diameter of the spheres. For a bed packed with

through-hole spheres or cylindrical particles, the effective particle diameter is comparable with the product of Sauter mean diameter and shape factor of the particles in each bed. In principle, this approach is valid for debris particles. However, it is not a trivial task to get the Sauter mean diameter and shape factor of debris from FCI tests. For DEFOR debris, we obtained the porosity and the effective particle diameter by direct measurement performed on the debris beds loaded to the POMECO-FL and POMECO-HT facilities. The so-obtained effective particle diameter of the debris bed with porosity of 0.45 is 1 mm. Given these parameters to safety analysis of a 3900 MWth BWR with its all core melt discharged to the cavity and fragmented in a deep water pool during a hypothetical severe accident, coolability is achieved with varied margins for various ex-vessel debris beds: i) the bed spreading over the entire floor of the cavity (top-flooding bed) is coolable; ii) compared with the top-flooding bed, the cylindrical bed with an annular-gap water supply enhances coolability, but the gain is marginal since the large diameter of the bed prevents the side coolant from flowing into the center of the bed; iii) a heap-like debris bed reduces rather than improves coolability due to its considerable height and base diameter; iv) a stratified debris bed with a fine-particle layer or agglomerated debris on the top may challenge the coolability.

The bottom-fed coolant driven by natural circulation through downcomer or other means enhances the coolability significantly. However, a cake formation or debris agglomeration in the debris bed will reduce the coolability margin if only dryout is concerned. It should be noted that dryout does not necessarily mean remelting of the debris when co-current flow of water and steam dominates in the debris bed. The contribution of steam cooling should be considered. More research is also needed for the effective particle diameter and porosity of debris beds with varied simulant materials and experimental conditions, as well as for validation of simulation tools with regard to multidimensional and large-scale debris beds.

3.5 Steam Explosion Energetics (SERA)

3.5.1. Motivation and Approach

The objectives of the SERA subproject are to investigate the effects of material properties on the triggerability and energetics of single droplet steam explosion, as well as to perform reactor-scale risk analysis for steam explosion. Since the latter is still in the preparation stage, i.e., collecting the plant data for a reference Nordic BWR and testing tools (e.g., MC3D code), only the former (MISTEE experiment for material effects on steam explosion) is presented here.

The past experiments concerning the steam explosion phenomena show a mixed record on the triggerability and explosivity of various molten materials (from pure metallic melts to prototypic corium melts). For instance, large scale experiments such as FARO showed no explosion or only mild interaction of corium with water even when a substantial external trigger was applied, while spontaneous energetic explosions were observed in KROTOS tests with pure alumina melt. The differences in the premixing characteristics and peculiarities of the alumina could be the reason for such a difference, thus obscuring the factual material effect on the steam explosion. Large scale experiments in TROI experiments with the eutectic UO_2-ZrO_2 melt produced energetic interactions, whereas the non-eutectic melt composi-

tions lead to mild interactions, raising the awareness of the possible role of the melt material effect as a limiting mechanism.

The large scale experiments are struggling to identify the physical mechanisms involved, since they incorporate all the phases of the steam explosion phenomena (premixing, triggering, propagation and expansion). In this respect, the MISTEE experiment for single-droplet steam explosion provides a possibility for separate effect investigations. The MISTEE facility [35] features a visualization system [36] which enables a simultaneous high-speed photography and radiography, and thus provides vapor film dynamics as well as the melt fragmentation dynamics [37], which is vital to understand the governing mechanisms for steam explosions.

3.5.2. Binary-Oxides Single Droplet Dynamics

Two series of externally triggered single-drop experiments were performed on the MISTEE test facility. In the first test series, an eutectic composition (75:25 mol%, $T_{liquidus}$=1135°C,) and a non-eutectic composition (72:27 mol%, $T_{liquidus}$=1232°C, $T_{solidus}$=1135°C) of WO_3-CaO were used as melt simulant with high initial melt superheat ($\Delta T_{superheat}$~200°C to 300°C) and high subcooling of water (~20°C). In the second test series, similar water subcooling and melt compositions, i.e. eutectic and non-eutectic WO3-CaO, were employed; the melt superheat, however, was lower (~100°C) than in the first test series.

The tests chosen for the actual post processing have simultaneous record of bubble and melt dynamics. Still photographic images, with a temporal resolution of 0.05 ms per frame and the corresponding X-ray radiography images, with a temporal resolution of 0.2 ms per frame, are presented in Figure 3.40 to Figure 3.43. The images reveal the vapor film and melt progression during the steam explosion of ~1 g of eutectic and non-eutectic molten WO_3-CaO droplets under high water subcooling, and different melt superheat. Similar to the single droplet experiments performed with a metallic melt (tin) [35], the vapor film dynamics produces three defined cycles of bubble expansion and collapse, as seen in Figure 3.44. For convenience, we define t=0 ms at the final collapse of the first bubble's cycle.

Due to the melt's high temperature, a vapor film with a small dome on the rear side is immediately formed at the time the molten WO_3-CaO droplet enters the water, and endures as it descends into the test section, Figure 3.40a to Figure 3.43a, with a velocity of approximately 0.47 m/s. The interaction is initiated once the external pressure wave destabilizes the vapor film, Figure 3.40b to Figure 3.43b initiating the bubble's *first cycle* expansion. During this cycle, the vapor film dynamics creates complex internal flows that disturb the melt droplet surface facilitating its deformation (i.e. preconditioning) clearly seen in the radiographic images, in which the initial elliptical droplet (bottom Figure 3.40a to Figure 3.43a), evolves into a convoluted droplet with fine fragments present in the droplet's periphery, Figure 3.40c to Figure 3.43c (bottom). The overgrown bubble/rear reaches its maximum, Figure 3.40c to Figure 3.43c, and starts to collapse towards the molten droplet. The accelerating interface hits the molten droplet. At this point (t=0 ms), the actual direct melt-coolant mixing takes place, Figure 3.40d to Figure 3.43d, which leads to the bubble's *second cycle* characterized by the explosive evaporation and fine fragmentation of the melt droplet.

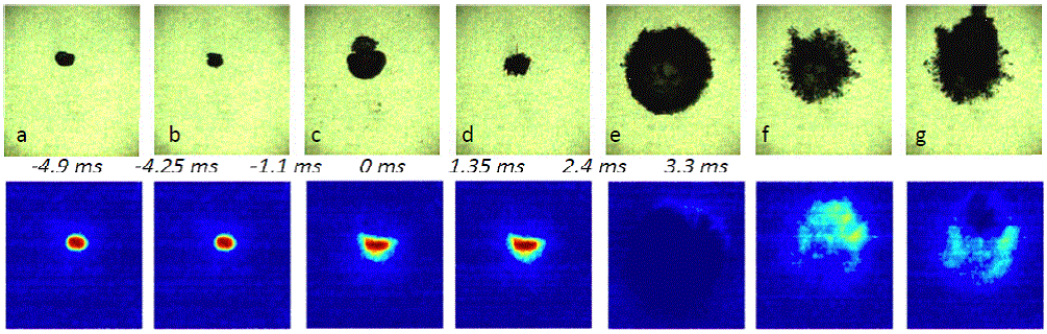

Figure 3.40: Vapor film (top) and melt dynamics (bottom) of a single droplet of eutectic WO_3-CaO initially at 1350°C superheat, undergoing vapor explosion in water at 20.4°C.

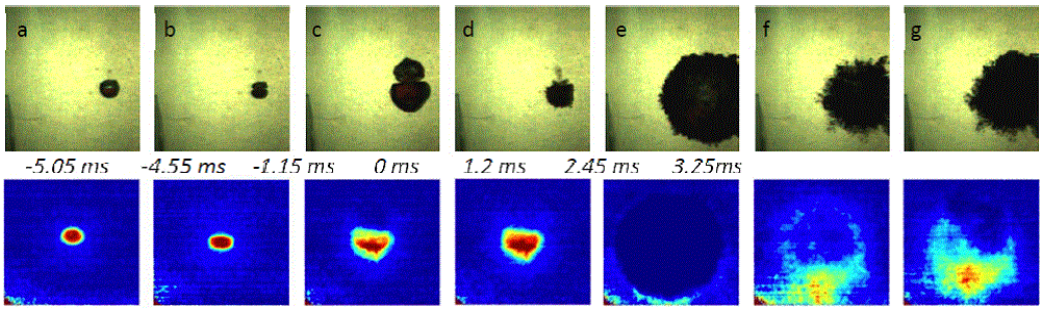

Figure 3.41: Vapor film (top) and melt dynamics (bottom) of a single droplet of non-eutectic WO_3-CaO initially at 1480°C superheat, undergoing vapor explosion in water at 20.1°C.

The produced fine fragments set off in the radial direction following the interface of the growing bubble, forming a shell-like region of finely fragmented melt particles. As the vapor bubble decelerates, the inertia continues to drive the fine fragments to penetrate deeper into the liquid domain. The bubble reaches its maximum size, Figure 3.40e to Figure 3.43e, and subsequently collapses, leaving the fine fragments behind. At this point, the bubble dynamics cannot be precisely discerned since the cloud of fine fragments unable the exact resolution of the vapor interface. Nevertheless, the bubble's *third cycle* can still be recognized, when the collapsing bubble promotes the mixing of the coolant and the remains of the molten material, Figure 3.40f to Figure 3.43f, leading to a secondary explosive vaporization, Figure 3.40g to Figure 3.43g. The fine fragments are then dispersed within the coolant after the bubble has finally collapsed.

No apparent dissimilarities in the vapor film and melt dynamics were found for the test series under high melt superheat (Figure 3.40 and Figure 3.41): both melt compositions, i.e. eutectic and non-eutectic WO_3-CaO, consistently led to three cycle interactions. Conversely, the test series with non-eutectic WO_3-CaO under lower melt superheat (Figure 3.43) reveal the presence of portions of a crust on the second cycle during fragmentation, Figure 3.43e-f, whereas the eutectic tests (Figure 3.42) regularly led to the fine fragmentation of melt droplet similar to the high superheat tests.

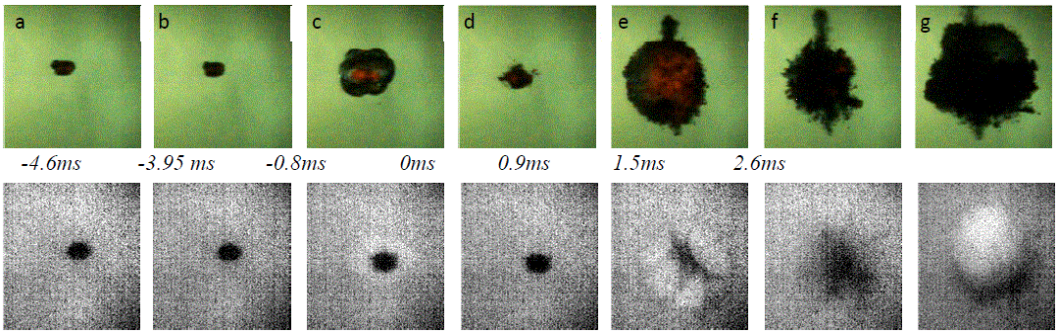

Figure 3.42: Vapor film (top) and melt dynamics (bottom) of a single droplet of eutectic WO_3-CaO initially at 1251°C superheat, undergoing vapor explosion in water at 23°C.

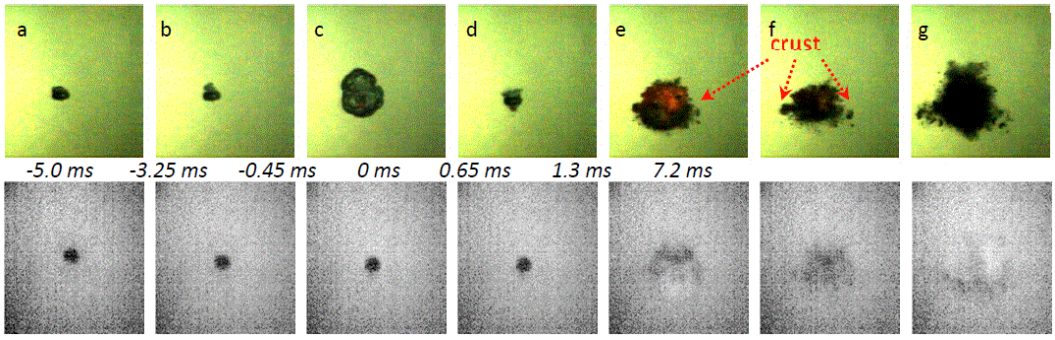

Figure 3.43: Vapor film (top) and melt dynamics (bottom) of a single droplet of non-eutectic WO_3-CaO initially at 1350°C superheat, undergoing vapor explosion in water at 22.3°C.

The equivalent diameter (estimated from the vapor bubble projected area), normalized by its value prior to the external disturbance, is shown in Figure 3.44 for eutectic (e) and non-eutectic (ne) mixtures of WO_3.-CaO and different melt superheat. One can clearly identify the three cycles mentioned previously. In the high melt superheat tests, Figure 3.44a, both melt compositions cover a wide spectrum of the vapor film history and no particularity can be discerned. The lower melt superheat tests, Figure 3.44b, appear to show a tendency of a more pronounced 2nd and 3rd cycle in the eutectic runs; however a clearer picture of such differences should arise by evaluating the energetics associated with the interaction. The melt preconditioning (deformation/pre-fragmentation of a molten droplet during the first bubble cycle), postulated to influence the interaction's conversion ratio, is quantified by the droplet's projected area evolution depicted in the radiographic images. Figure 3.45a points out to no apparent differences between the eutectic and non-eutectic tests with high melt superheat in terms of steam explosion energetics and preconditioning, which is a reflection of what is seen in the bubble dynamics, Figure 3.44a. In contrast, Figure 3.45b shows a divergence between the energetics and melt preconditioning of the eutectic and non-eutectic tests, i.e. non-eutectic test led to a milder interaction than the eutectic tests.

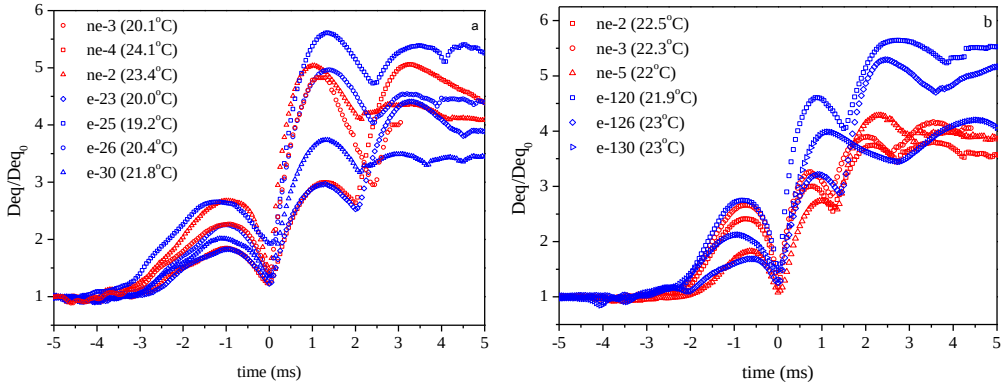

Figure 3.44: Radial history of eutectic (e) and non-eutectic (ne) WO_3-CaO single droplet for high (a) and low (b) melt superheat, with the respective water temperature.

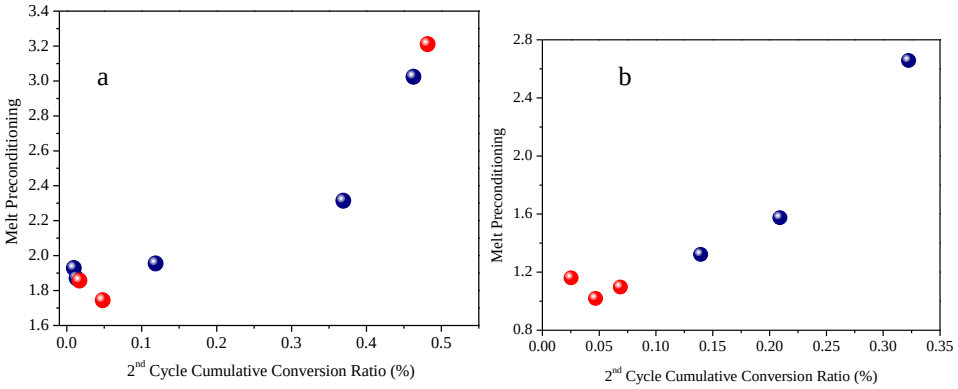

Figure 3.45: Melt droplet preconditioning and 2nd cycle cumulative conversion ratio of eutectic (blue) and non-eutectic (red) WO_3-CaO single droplet for high (a) and low (b) melt superheat.

Such observations can be rationalized by considering the phase change of a non-eutectic binary oxidic melt droplet. If the droplet superheat is high enough the material phase will be kept liquid during the interaction for both melt compositions. In the case of low superheat experiments, the melt temperature falls between the liquidus and solidus line for the non-eutectic material, which is augmented by the difference in undercooling characteristic of such fast quenching. In fact, for non-eutectic materials, it suffices to remove only a fraction of the latent heat of fusion to bring the melt into a mushy state. Once in this regime, formation of a thin crust or even a mushy layer on the droplet's surface would significantly increase the resilience to fragmentation due to melt-coolant contacts. Correspondingly, the non-eutectic WO_3-CaO melt droplet shows a diminutive melt preconditioning and steam explosion conversion ratio, Figure 3.45b. Moreover, the consistent presence of a crust, Figure 3.43e-g, on the non-eutectic tests implies less melt material available for the interaction, contributing to the differences in energetics between eutectic and non-eutectic tests.

3.5.3. Debris Analysis

To further explore the solidification trends of the binary oxide melt discussed previously, debris collected from the fuel and coolant interaction were subject to physical and chemical analysis by means of Scanning Electron Microscopy (SEM). The fragmented WO_3-CaO particles were collected from two experiments for the different melt compositions, i.e. eutectic and non-eutectic. The debris size distribution was attained by sieving the particles (sieve size from 38μm to 1.70mm) and it is represented in Figure 3.46.

Generally speaking, eutectic WO_3-CaO produced mostly fine fragments (38-150μm), while the non-eutectic produced mostly larger ones (300-1700μm); thus, indicating different fragmentation rates between the materials. The morphology of debris may help understand the solidification characteristics of droplets, as shown in Figure 3.47. For instance, deep undercooling leads to high growth velocities (solidification rate) producing debris mildly stratified, as is seen in the eutectic case. And the opposite is true for the non-eutectic material.

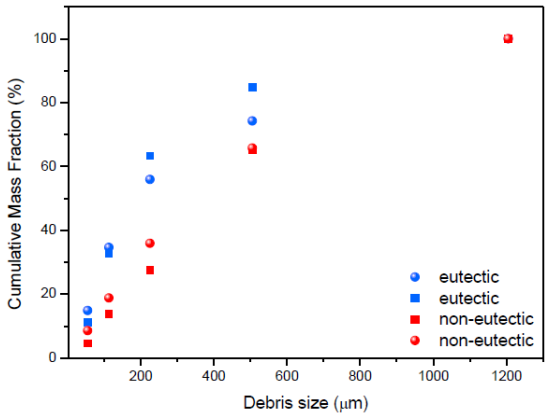

Figure 3.46: Debris size distribution of eutectic and non-eutectic WO_3-CaO melt droplets, with a 100˚C superheat, which underwent a steam explosion.

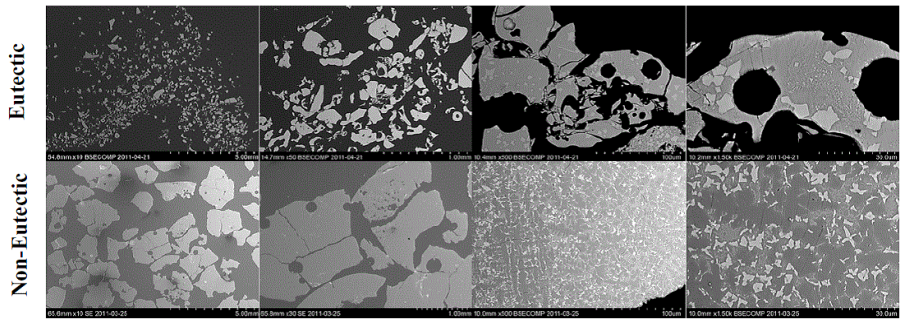

Figure 3.47: Morphology of the fragmented debris.

3.5.4. Implications to Reactor Safety

The MISTEE experimental data confirm the correlation between the melt droplet preconditioning (fragmentation prior to steam explosion) with the interaction's energetics (conversion ratio), and implicate the role of the melt composition (binary oxides) affecting the single droplet steam explosion.

It is suggested that the distinction in energetics between eutectic and non-eutectic mixture of binary oxides at lower superheat is due to the solidification characteristics of the melt droplet during the direct melt-coolant contact. However, that can explain observed in TROI tests "material effect" only when the melt temperature is quite close to liquidus temperature (small melt superheat).

3.6 Severe Accident Information Distillation (SAID)

The SAID task is mainly fulfilled by KTH participation in the OECD/SERENA-2 project and EU project SARNET2 (Severe Accident Research Network of Excellence - Phase 2). KTH provides the APRI7 research results into SARNET2 and takes useful information from SERENA-2 and SARNET2 for Swedish nuclear power plants.

An international programme, known as Phase-1 of SERENA concluded that in-vessel FCI would not challenge the integrity of the containment whereas this cannot be excluded for ex-vessel FCI. However, the large scatter of the predictions indicated lack of understanding in some areas, which makes it difficult to quantify containment safety margins to ex-vessel steam explosion. The results clearly indicated that uncertainties on the role of void (gas content and distribution) and corium melt properties on initial conditions (pre-mixing) and propagation of the explosion were the key issues to be resolved. The Phase-2 of SERENA is formulated to resolve the uncertainties on these issues by performing a limited number of well-designed tests with advanced instrumentation reflecting a large spectrum of ex-vessel melt compositions and conditions, and the required analytical work to bring the code capabilities to a sufficient level for use in reactor case analyses. The objective of the experimental programme is threefold: (i) Provide experimental data to clarify the explosion behaviour of prototypic corium melts, (ii) Provide innovative experimental data for validation of explosion models for prototypic materials, including spatial distribution of fuel and void during the premixing and at the time of explosion, and explosion dynamics, (iii) Provide experimental data for the steam explosion in more reactor-like situations to verify the geometrical extrapolation capabilities of the codes. These goals are achieved by using the complementary features of KROTOS (CEA) and TROI (KAERI) corium facilities including fitness for purpose oriented analytical activities. Tests accomplished so far provide useful data for addressing the uncertainties in the physical phenomena of steam explosion with different prototypic melt simulant materials. The experimental program will be completed in 2013. The report outcome is under preparation and will be available for KTH.

The SARNET2 was conceived to join the research capacities of 41 organizations in 20 countries from EU, USA, Canada and Korea, with the goal to i) resolve the most important pending SA issues for enhancing the safety of existing and future Nuclear Power Plants (NPPs), and ii) optimize the use of the available resources and to constitute a sustainable integration of European research on Severe Accident phenomenology and management. The time span of SARNET2 is from 1 April 2009~31 March 2013, and divided into three periods corresponding to three Joint Programs of Activities (JPA), i.e., JPA1, JPA2 and JPA3. JPA1 is from April 2009 to March 2010, JPA2 from April 2010 to September 2011 and JPA3 from October 2011 to March 2013. SANET2 has 8 work-packages. KTH is mainly involved in

WP1~WP7. Since the activities of SANET2 are still ongoing, the reporting here is only given to the status of the main work packages with KTH involvement.

3.6.1. WP2: Spreading of Excellence

The textbook "Nuclear Safety in Light Water Reactors - Severe Accident Phenomenology" was finalized and agreed to be published by ELSEVIER in January 2012. About 400 pre-orders have been done on the ELSEVIER's web site. In the mobility programme, exchange of students and researchers is supported between partners for training/spreading of excellence activities. One conference (European Review Meetings on Severe Accident Research – ERMSAR 2009) has been organized in Italy, and next one (ERMSAR 2012) will be held in Cologne, Germany, March 2012. One short course for severe accident phenomena was also given in 2010.

3.6.2. WP4: ASTEC Code

The ASTEC code, jointly developed by IRSN and GRS, is the integrated code for severe accident simulation. The latest release of the code is V2.0 with various revisions. The ASTEC code has been extensively applied for severe accident safety analysis of pressurized water reactors (LWRs), such as the reactors of French PWR, Konvoi 1300, Westinghouse AP1000, VVER-440, VVER-1000. However, the code is not ready for boiling water reactors (BWRs) yet. This is an intention for such a further development. In SARNET2, detailed adaptation plan of physical model with regard of BWRs was made with the joint efforts of GRS, KTH and IKE- Stuttgart University. Nevertheless, the work of adaptation or new models development is more or less on hold, due to lacking national interest and support of the three partners involved.

3.6.3. WP5: Corium and Debris Coolability

KTH is heavily involved in this work package. A lot of data have been generated in this work package regarding reflooding of a degraded core, melt pool behavior, debris bed formation and coolability. Specifically, QUENCH-Debris test is under preparation and will be performed in spring 2012 to investigate the debris formation in the reflooding phase, using the QUENCH facility at KIT, Karlsruhe, Germany. New tests were performed in the LIVE research program at KIT to investigate melt pool behavior (e.g., heat transfer, crust formation, stratification), including tests performed on both LIVE-3D and LIVE-2D test facility. The results allow a direct comparison between 2D and 3D tests, and further comparisons with the findings obtained in other experiment programs (SIMECO, ACOPO, BALI, etc.) performed earlier, so as to improve the understanding of melt pool heat transfer and reduce the uncertainty in assessment of thermal load to the lower heat during a severe accident.

To investigate the effect of multidimensionality of debris bed on its coolability, IRSN launched the experimental program PEARL mainly supported by EDF to validate simulation tools to be used in the safety issues studies dealing with the evaluation of the consequences of water reflooding of a severely damaged reactor core where a large part of the core has collapsed and formed a debris bed. The experimental data will allow fulfilling a gap by extending the validation of debris reflooding models in 2D and 3D situations.

The DEBRIS facility at Stuttgart University (Germany) is also dedicated to experimental study on debris bed coolability, which can operate at pressure up to 40 bar and temperature up to 300°C. The total height of the vessel is 2.8 m and inner diameter is 625 mm. The height of the bed is 870 mm and its inner diameter is 125 mm. In addition to STYX test facility for study of one-dimensional debris bed coolability, a new test facility named COOLOCE was constructed by VTT to investigate the coolability of cone-shaped particulate beds, with the objectives to compare coolability of a conical (heap-like) debris bed with a cylindrical debris bed, and address the effects of multi-dimensional flooding on coolability. The conical bed is 500 mm in bottom diameter and 270 mm in height.

3.7 Conclusions

Significant progress was made and important findings were obtained in the APRI-7 project at KTH. The risk-oriented approach is continued to guide us to identify risk-significant phenomena/effects and suggest appropriate level of treatment. The capabilities emerging in APRI-6 to perform analyses of the phenomena have been further advanced and maturated, and new activities/capabilities were introduced and developed in APRI-7 during the risk quantification process.

The INCOSAM study reveals that the vessel integrity cannot be secured if only CRGT (Control Rod Guide Tube) cooling is activated and the melt pool depth is higher than 0.7 m. Two types of vessel wall failure modes were identified: (i) a ballooning-creep failure in (melt pool up to 1.1 m); and (ii) a localized-creep failure (melt pool depths above 1.5 m). These two modes may lead to different melt release modes in terms of breach size, melt mass and melt compositions and superheat. If an external vessel cooling is implemented in addition to CRGT cooling right before creep accelerates, we found that in-vessel retention (IVR) of the melt is possible in all the melt pool configurations considered (0.7 m to 1.9 m). If there is only CRGT cooling applied, then the IGT (Instrumentation Guide Tube) close to the bottom center is not clamped in its housing during accident, and can fail at least 1 h before the global vessel failure. Therefore the identified dominant vessel failure mode is IGT melt-through.

The DEFOR study shows that the particle morphology of the prototypic corium debris obtained in the past is inclusive of types identified in the DEFOR-S tests. The results of the DEFOR-S experiment also reveals the influence of water subcooling on particle morphology, on encapsulated porosity and finally on average porosity of the debris bed which was found to be higher (~45-70%) than the traditionally assumed value of 40% characteristic of solid spherical particles packing. The dependency of mass fraction of agglomerated debris on water pool depth is studied systematically in the DEFOR-A experiment. It is found that the fraction of agglomerated debris decreases rapidly with increasing pool depth. Size distribution of the particles obtained in the DEFOR-A tests is quite close to that from the FARO tests carried out with corium. Analysis performed to explain DEFOR-S experimental findings demonstrates that rapid changes in cooling rate during transition from film to nucleate boiling and resulting thermal stresses can explain different morphologies of the melt simulant particles observed at different subcooling of water. A mechanistic conservative approach to predict the debris agglomeration is proposed based on the VAPEX FCI code. Validation of the approach is performed against DEFOR-

A experimental data, and an agglomeration mode map is proposed as a means for quantification of the fraction of agglomerated debris in plant accident conditions. The DECOSIM code is developed and applied for investigation of feedbacks and self-organization processes in the debris bed formation and coolability, and self-spreading of the bed in a gradual melt release mode for subcooled pool conditions has been analyzed. Extensive sensitivity-uncertainty analysis has been performed for 1D debris bed coolability. Calibrated "classical" model has been proposed based on the optimization with regards to available experimental data. Comprehensive sensitivity analysis suggests that up to 70% of the uncertainty in the debris bed coolability is due to the uncertainty in the particle size distribution.

The POMECO study provides an approach to determine friction laws and dryout heat fluxes of particulate beds packed with multi-size and irregular particles. For a particulate bed packed with multi-diameter spheres, the frictional pressure drop of two-phase flow and dryout heat flux of the bed can be predicted by Reed model using the Sauter mean diameter of the spheres. For a bed packed with through-hole spheres or cylindrical particles, an equivalent diameter can be chosen in the Reed model, which is the product of Sauter mean diameter and shape factor of the particles. For debris particles whose shape factor is unknown, one can obtain the effective particle diameter (to be used in Reed model) via direct measurement of single-phase flow on the debris bed. The so-obtained effective particle diameter of the selected DEFOR debris particles is 1 mm in a bed of porosity 0.45. Given these parameters to safety analysis of a 3900 MWth BWR with its all core melt discharged to the cavity and fragmented in a water pool during a hypothetical severe accident, coolability is achievable with varied margins for the various ex-vessel debris beds. The bottom-fed coolant driven by natural circulation through downcomer or other means enhances the coolability significantly, whereas cake formation or debris agglomeration in the debris bed will reduce the coolability margin.

The SERA in MISTEE study by using corium simulant (WO_3-CaO) provides data on the processes that the eutectic and non-eutectic binary mixture affects the steam explosion energetics, and it reveals noticeable differences only at lower superheat. The effect is due to distinct solidification of eutectic melt from non-eutectic melt. This finding is insufficient to explain how different concentrations of UO_2-ZrO_2 (eutectic and non-eutectic) lead to substantial differences in the resulting energetics of steam explosion in TROI tests.

Overall, substantial progress has been achieved in the APRI-7 research at KTH, to help reducing uncertainties in quantification of ex-vessel melt risks in Nordic BWRs. The present report summarized only some key selected activities and the corresponding results. More detailed descriptions of the project achievements can be found in the relevant publications [1] - [44]. Notably, three PhD students (Drs. C.T Tran, Mikhail Davydov, and R.C. Hansson) were graduated during the APRI-7 project, whose theses are dedicated to the studies on in-vessel coolability [15], debris formation [5][20][21][22] and steam explosion exegetics [35].

3.8 Referenser

[1] A. Karbojian, W.M. Ma, P. Kudinov and T.N. Dinh, A scoping study of debris formation in the DEFOR test facility, *Nuclear Engineering and Design*, **239** (9):1653-1659, 2009.

[2] W.M. Ma and T.N. Dinh, The effects of debris bed's prototypical characteristics on corium coolability in a LWR severe accident, *Nuclear Engineering and Design*, **240**: 598-608, 2010.

[3] P. Kudinov, A. Karbojian, W.M. Ma, and T.N. Dinh The DEFOR-S experimental study of debris formation with corium simulant materials, *Nuclear Technology*, **170**(1): 219-230, 2010.

[4] P. Kudinov, A. Karbojian, C.-T. Tran, and W. Villanueva, The DEFOR-A experiment on fraction of agglomerated debris as a function of water pool depth, *Proc. of The 8th International Topical Meeting on Nuclear Thermal-Hydraulics, Operation and Safety (NUTHOS-8)*, Shanghai, China, October 10-14, 2010.

[5] P. Kudinov and M. Davydov, Development and validation of the approach to prediction of mass fraction of agglomerated sebris, *Proc. of NUTHOS-8*, Shanghai, China, October 10-14, 2010.

[6] S. Yakush, P. Kudinov, and T.N. Dinh, Multiscale simulations of self-organization phenomena in the formation and coolability of corium debris bed, *Proc. of The 13th International Topical Meeting on Nuclear Reactor Thermal Hydraulics (NURETH-13)*, Kanazawa City Japan, September 27-October 2, 2009.

[7] S. Yakush and P. Kudinov, Effects of water pool subcooling on the debris bed spreading by coolant flow, *Proc. of 2011 International Congress on Advances in Nuclear Power Plants (ICAPP 2011)*, Nice, France, May 2-5, 2011.

[8] C.T. Tran and T.N. Dinh, The effective convectivity model for simulation of melt pool heat transfer in a light water reactor pressure vessel lower head. Part I: Physical processes, modeling and model implementation, *Progress in Nuclear Energy*, **51**: 849-859, 2009.

[9] C.T. Tran, P. Kudino, and T.N. Dinh, An approach to numerical simulation and analysis of molten corium coolability in a BWR lower head," Nuclear Engineering and Design, **240**: 2148–2159, 2010.

[10] W. Villanueva, C.T. Tran and P. Kudinov, Assessment with coupled thermo-mechanical creep analysis of combined CRGT and external vessel cooling efficiency for a BWR, *Proc. NURETH-14*, Toronto, Canada, Sept. 25-29, 2011.

[11] W. Villanueva, C.T. Tran and P. Kudinov, Coupled thermo-mechanical creep analysis for boiling water reactor pressure vessel wall lower head, *Proc. of NUTHOS-8*, Shanghai, China, October 10-14, 2010.

[12] C.T. Tran and P. Kudinov, Local heat transfer from the corium melt pool to the boiling water reactor pressure vessel wall, *Proc. of NURETH-14*, Toronto, Canada, September 25-29, 2011.

[13] F. Cadinu, C.T. Tran and P. Kudinov, Analysis of in-vessel coolability and retention with control rod guide tube cooling in boiling water reactors, *Joint Workshop of OECD/NEA and EC SARNET2 on In-Vessel Coolability*, NEA Headquarters, Issy-les-Moulineaux, France, October 12- 14, 2009.

[14] W. Villanueva, C.T. Tran and P. Kudinov, A Computational study on instrumentation guide tube failure during a severe accident in boiling water reactors, *Proc. of NURETH-14*, Toronto, Ontario, Canada, September 25-29, 2011.

[15] C.T. Tran, *The Effective Convectivity Model for Simulation and Analysis of Melt Pool Heat Transfer in a Light Water Reactor Pressure Vessel Lower Head*, Ph. D thesis of Royal Institute of Technology, Stockholm, September 2009.

[16] P. Kudinov, V. Kudinova, and T.-N. Dinh, Molten oxidic particle fracture during quenching in water, 7th International Conference on Multiphase Flow ICMF 2010, Tampa, FL USA, May 30-June 4, 2010.

[17] P. Kudinov and V. Kudinova, Influence of Water Subcooling on fracture of melt debris particle, ANS Transactions, 2009.

[18] S. Yakush and P. Kudinov, Simulation of ex-vessel debris bed formation and coolability in a LWR severe accident, *Proc. of ISAMM-2009*, Böttstein, Switzerland, October 26 – 28, 2009.

[19] P. Kudinov, A. Karbojian, and C.T. Tran, Experimental investigation of melt debris agglomeration with high melting temperature simulant materials, *Proc. of ISAMM-2009*, Böttstein, Switzerland, October 26 – 28, 2009.

[20] P. Kudinov and M. Davydov, Approach to Prediction of melt debris agglomeration modes in a LWR severe accident, *Proc. of ISAMM-2009*, Böttstein, Switzerland, October 26 - 28, (2009).

[21] P. Kudinov and M. Davydov, Development of ex-vessel debris agglomeration mode map for a LWR severe accident conditions, *Proc. of ICONE-17*, Brussels, Belgium, July 12-16, 2009.

[22] P. Kudinov and M. Davydov, Prediction of mass fraction of agglomerated debris in a LWR severe accident, *Proc. of NURETH-14*, Toronto, Ontario, Canada, September 25-29, 2011.

[23] S. Yakush, P. Kudinov and N.T. Lubchenko, Sensitivity and uncertainty analysis of debris bed coolability, *Proc. of NURETH-14*, Toronto, Ontario, Canada, September 25-29, 2011.

[24] P. Kudinov, A. Karbojian, W.M. Ma and T.N. Dinh, An experimental study on debris formation with corium stimulant materials, Proc. ICAPP'08, Anaheim, CA USA, June 8–12, 2008.

[25] L.A. Dombrovsky, M.V. Davydov, and P. Kudinov, Thermal radiation modeling in numerical simulation of melt-coolant interaction, *Computational Thermal Science*, **1**(1), pp.1-35 (2009).

[26] L.X. Li and W.M. Ma, Experimental characterization of effective particle diameter of a packed bed with multi-diameter spheres, *Nuclear Engineering and Design*, **241**: 1736-1745, 2011.

[27] W.M. Ma, L.X. Li and A. Karbojian, An experimental study on coolability of volumetrically heated particulate beds of prototypical characteristics, *Proc. of NUTHOS-8*, Shanghai, China, October 10-14, 2010.

[28] L.X. Li and W.M. Ma, Experimental investigations on friction laws and dryout heat flux of particulate bed packed with multi-size spheres or irregular particles, *Proc. of ICONE19*, May 16-19, Chiba, Japan.

[29] L.X. Li and W.M. Ma, An experimental study on the effective particle diameter of a packed bed with non-spherical particles, *Transport in Porous Media*, **89**: 35-48, 2011.

[30] L.X. Li, S. Thakre and W.M. Ma, An experimental study on two-phase flow and coolability of particulate beds packed with multi-size particles, *Proc. of NURETH-14*, Toronto, Canada, September 25-29, 2011.

[31] L.X. Li, A. Karbojian, P. Kudinov and W.M. Ma, An experimental study on dryout heat flux of particulate beds packed with irregular particles, *Proc. of ICAPP2011*, Nice, France, May 2-5, 2011.

[32] W.M. Ma, Prediction of dryout heat flux of volumetrically heated particulate beds packed with multi-size particles, *Proc. NURETH-14*, Toronto, Canada, September 25-29, 2011.

[33] L.X. Li, S.J. Gong and W.M. Ma, An experimental study on two-phase flow regime and pressure drop in a particulate bed packed with multi-diameter particles, *Nuclear Technology*, in press.

[34] L.X. Li and W.M. Ma, Toward quantification of debris bed coolability in corium risk assessment, *Transactions of ANS Winter Meeting*, Washington DC, Oct. 30-Nov. 3, 2011.

[35] R.C. Hansson, *An experimental study on the dynamics of a single droplet vapor explosion*, Ph. D thesis of Royal Institute of Technology, Stockholm, November 2010.

[36] R.C. Hansson, H.S. Park and T.N. Dinh, Simultaneous high speed digital cinematographic and X-ray radiographic imaging of an intense multi-fluid interaction with rapid phase changes, *Experimental Thermal and Fluid Science*, **33**: 754-756, 2009.

[37] R.C. Hansson, H.S. Park and T.N. Dinh, Dynamics and preconditioning in a single droplet vapor explosion, *Nuclear Technology*, **167**: 223-234, 2009.

[38] R.C. Hansson, L.T. Manickam and T.N. Dinh, The effect of binary oxide materials on a single droplet vapor explosion triggering, *Proc. NURETH-14*, Toronto, Canada, September 25-29, 2011.

[39] S. Thakre, L.X. Li and W.M. Ma, A numerical analysis on the hydrodynamics of heavy molten droplets in a water pool, Proceedings of ICAPP 2011, Nice, France, May 2-5, 2011.

[40] *Proc. of the 28th Review Meeting for Project "Melt-Structure-Water Interactions in a Severe Accident" (MSWI-28)*, KTH, Stockholm, Sweden, June 10, 2009, 84p.

[41] *Proc. of the 29th Review Meeting for Project "Melt-Structure-Water Interactions in a Severe Accident" (MSWI-29)*, KTH, Stockholm, Sweden, December 9, 2009, 90p.

[42] *Proc. of the 30th Review Meeting for Project "Melt-Structure-Water Interactions in a Severe Accident" (MSWI-30)*, KTH, Stockholm, Sweden, June 10, 2010, 105p.

[43] *Proc. of the 31st Review Meeting for Project "Melt-Structure-Water Interactions in a Severe Accident" (MSWI-31)*, KTH, Stockholm, Sweden, December 9, 2010, 90p.

[44] *Proc. of the 32th Review Meeting for Project "Melt-Structure-Water Interactions in a Severe Accident" (MSWI-32)*, KTH, Stockholm, Sweden, June 15, 2011, 118p.

[45] P. Schäfer, M. Groll, R. Kulenovic, Basic investigations on debris bed cooling, *Nuclear Engineering and Design*, **236**: 2104-2116, 2006.

4. CHALMERS RESEARCH ON SEVERE ACCIDENTS

4.1 General description of iodine chemistry during severe accidents

Radioactive iodines, which are short lived fission products, pose an exceptional threat to the health of the general public. This is because the fission yields of the iodines are high, that iodine can exist in several mobile forms [4.1] and because humans (and other mammals) accumulate iodine inside a single small gland (thyroid gland). The thyroid gland is responsible for the production of a series of organoiodine hormones (thyroxines) which are responsible for the regulation of heat production (basal metabolic rate) and other metabolic processes. While the prognosis for a human diagnosed thyroid cancer is less grave than it is for many other forms of cancer, the after effects of a successful treatment for thyroid cancer with ^{131}I are likely to require the patient to consume thyroid supplements [4.2] on a daily basis for the remainder of their life, thus causing everlasting inconvenience to the patient and a high cost to society.

As a result of damage to the fuel during a severe nuclear accident in light water reactors (LWR`s), large amounts of iodine (both in elemental and anionic form) will be liberated from the fuel. Under the harsh conditions of the accident (heat and irradiation) this iodine can participate in a complex web of chemical reactions. The organic substances released from organic materials (paint and plastics) and boron carbide into the containment gases can form volatile organoiodine species [4.3]. These organic iodine species include methyl iodide [4.4] (CH_3I, MeI) and may also include ethyl iodide (C_2H_5I, EtI). These organic species can not efficiently be removed from gases by the mitigating systems deployed at Swedish nuclear power plants.

The concrete walls, floors and other surfaces in the containment of a modern Swedish nuclear power plant (eg Ringhals 2) are painted with epoxy paints. These coatings are of interest since they can act as an “iodine depot” and thus may have a beneficial effect on the iodine behaviour during a severe nuclear accident. The absorption of methyl iodide and other forms of iodine into paint is being investigated at Chalmers.

In addition to the formation of the mobile organoiodines during an accident, particles containing radioactive iodine can form. Depending on the size of the particles they will either be unlikely to escape far from a damaged plant during an accident or they will be able to escape and thus exert a harmful effect upon the general public and the environment. After Chernobyl the discovery of fine particles at great distances from the plant illustrates this mode of transport for radioactivity [4.5]. A need existed for an expansion of our understanding of the process by which common volatile iodine species react with the radiolysis products of air [4.6]. To this end an experimental rig named EXSI [4.7] has been used to study the formation of iodine oxide particles.

During an accident inside the containment, acid can be formed by overheating plastics containing clorine, for example electrical cables. An investigation was made to allow better understanding of the conditions which will exist shortly after a severe

accident. The introduction of acid into the water pools inside the containment can have a harmful influence on the iodine chemistry. It has been known since Napoleonic times that acidification promotes the formation of volatile elemental iodine. The effects of pH and redox potential on the volatility of iodine were probed by electrochemical and computational means.

4.2 Investigation of cable insulation materials such as Hypalon

Inside the containment of a BWR there are many cables which are located near the lower part of the reactor pressure vessel, these are for instrumentation, supplying power and for delivering commands to devices. During a severe accident, these cables can be degraded by heat and radiation as the core melts. This part of the project is intended to a) determine the amount of hydrochloric acid, other acids and bases formed by the cables and b) identify and quantify the volatile organic molecules which could then form volatile organic iodides.

The introduction of hydrogen chloride (HCl) into the water pools of the containment is of great concern as this acid is a nasty impurity. According to the mathematical models the acidification of the water is likely to alter the volatility of the iodine. Furthermore the hydrogen chloride present in dry parts of the containment could alter the chemistry of the iodine in these areas. One key source of hydrogen chloride is the thermal dehydrochlorination of halogenated electric cable insulation materials such as chlorinated polyethene. The abilities of different cable plastics to form small organic molecules is being investigated. So far the cable materials which have been included in the pre-study include polyvinyl chloride (PVC is close to everywhere in modern electrical cables), pure chlorosulfonated polyethylene (which is the basis of the hypalon cable which is used in Swedish nuclear reactor containments), two flame retardant polyurethane cable plastics and finally an electron beam crosslinked polyethene sold under the name Radox.

Pyrolysis gas chromatography is an analytical technique which has been used for many years for the forensic examination of small traces of paint from cars [4.8]. In this method a small sample of the paint is rapidly heated to decompose it, the vapors from the paint are then examined by gas chromatography. This analytical equipment provides an opportunity to subject paints and plastics to a simulation of the overheating which will occur as a molten core breaks through the lower part of the reactor pressure vessel.

When pure chlorosulfonated polyethene was heated to 275^{o}C sulfur dioxide and hydrogen chloride were emitted by the sample. When the same sample was reheated to 360^{o}C hydrogen chloride was emitted again but in addition a small trace of benzene was formed. When the sample was reheated again to 500^{o}C both benzene and hydrogen chloride were detected. Finally the sample was reheated to 750 ^{o}C thus forming a complex mixture of benzene, toluene, xylenes, styrene, naphthalene and other compounds. This series of aromatic pyrolysis products suggests that the chlorosulfonated polyethene decomposes in a similar way to PVC.

It was found that chlorosulfonated polyethylene emitted a similar amount of hydrogen chloride to the sample of the PVC cable, but this result needs to be taken with some caution. A plastic typically contains at least one polymer together with plasti-

cizers (such as dialkyl phthalates) and inorganic additives such as dolomite ($CaCO_3/MgCO_3$) are typically added to retard the aging of the plastic by scavenging the acid formed by the degradation of the polymer. Below is shown the graph of the production of hydrogen chloride as a function of time for the larger scale pyrolysis of PVC cable and chlorosulfonated polyethene (hypalon).

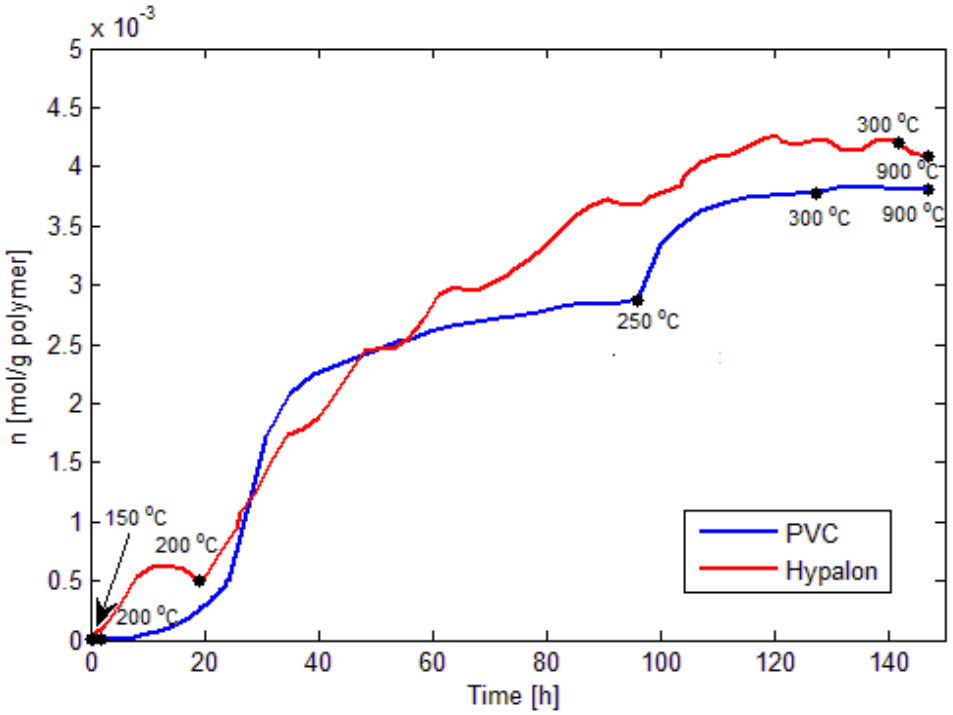

Figure 4.1. Titration results from a pyrolysis experiment.

When a sample of a PVC electrical cable was subject to the examination by Pyro-GCMS the hydrogen chloride production was far less obvious. The gas chromatogram at 275, 360 and 500°C was dominated by the plasticizer (dibutyl phthalate) while at 750°C the complex mixture of aromatic compounds was observed.

When the polyurethane and cross linked polyethylene (Radox™) cables were heated, far less acidic matter was released. For the polyurethane sample a large pH increase was obtained at 400°C, from pH 4.8 to pH 8.8 due to release of alkaline gases suspected to be amines.

The thermal degradation of hypalon electrical cables is likely to generate a large amount of hydrogen chloride (hydrochloric acid) during an accident. The hypalon may behave chemically in a similar way to PVC cable during an accident.

The alternative flame retardant cable plastics (polyurethane and cross linked polyethylene) are less able to form acidic gases during an accident. The accident gases formed by the halogenated cable plastics may alter the pH of the water pools in the containment thus altering the iodine chemistry.

.

4.3 Iodine chemistry in severe accidents

There have been only a few experimental studies of the effect of radiolytic decomposition of gaseous organic iodine compounds. Tang *et. al.* [4.9] found that the reaction rate of the decomposition was zero-order at concentrations below $2.4x10^{-3}$ $mol \cdot dm^{-3}$ and pseudo-first order below $2.4 \cdot 10^{-7}$ $mol \cdot dm^{-3}$. The experiments were performed at room temperature. The first-order rate constant was calculated by Dickinson *et. al.* to be $5.75 \cdot 10^{-4}$ Gy^{-1}[4.10].

Tang *et. al.* proposed a mechanism for the radiolytic destruction of CH_3I, which involved reaction with an activated species:

$$CH_3I + M^* \rightarrow CH_3\cdot + I\cdot + M$$

It was assumed that the γ-ray energy is primarily absorbed by air to form active particles, M*, which in turn transfer energy to CH_3I molecules upon collision. It is generally accepted that the reaction of methyl radicals with oxygen takes place *via* two routes: a thermomolecular reaction leading to the formation of methyl peroxide radicals

$$CH_3\cdot + O_2 + M \rightarrow CH_3O_2\cdot + M$$

and a bimolecular reaction which forms formaldehyde:

$$CH_3\cdot + O_2 \rightarrow HCHO + OH\cdot$$

Formaldehyde and methanol has been shown to be formed before in earlier NROI experiment. When the iodine radicals, I·, are recombined elemental iodine, I_2, is formed:

$$I\cdot + I\cdot \rightarrow I_2$$

The last reaction accounts for the formation of I_2 observed in the experiments at high CH_3I concentrations, but would be unlikely to occur at low concentrations where other reactions of I· would be more likely.

Ozone is a radiolysis product that can have an influence on the iodine chemistry in the containment. The reaction between ozone and iodine is well-known in the atmospheric chemistry community and has been investigated by Jimenez *et. al*. [4.11] and other workers.

Cox *et. al.* [4.12] have performed experiments of CH_3I photolysis with presence of ozone at 303 K. Cox *et. al.* used low-pressure mercury lamps, UV-quanta emitted mainly at 254 nm, for the photolysis. This can be compared to the UVC radiation used in our study with the main peaks at 185 and 254 nm. Cox *et. al.* found that IO· radicals were produced by the photolysis of methyl iodide in the presence of ozone through a series of reactions which are analogous to some of those responsible for the destruction of ozone in the upper atmosphere by chlorofluorocarbons (freons).

$CH_3I + h\nu \rightarrow CH_3\cdot + I\cdot$

$I\cdot + O_3 \rightarrow IO\cdot + O_2$

Bimolecular association of the formed $IO\cdot$ radicals is then the initiating step for production of bigger iodine oxides (I_xO_y):

$IO\cdot + IO\cdot \rightarrow I_2O_2$

Cox *et. al.* also found that I_4O_9 was formed in the system as a yellow deposit on the cell surfaces. This deposit was finally converted to I_2. The speciation of the particles was determined using Raman spectroscopy. The authors determined the photo dissociation rate constant for CH_3I to $0.65\text{-}1.41\cdot10^{-3}$ s^{-1}.

The mechanism for the reaction between ozone and methyl iodide, is not fully understood yet. Two possible mechanisms are suggested: either the ozone molecule is decomposed to O_2 and $O\cdot$ that further react with CH_3I, or there is a direct reaction between ozone and methyl iodide [4.13]-[4.14]. However, the work of Jimenez *et. al*. [4.15] using methylene diiodide $\{CH_2I_2\}$ as precursor suggested that ozone does not react with alkyl iodides, but the ozone does react with the iodine atoms formed by the light induced homolysis of the carbon iodine bond. In Jimenez's experiments no particles were detected when ozone (100 ppb) and methylene diiodide (5 ppb) were combined in the dark.

The projects, NROI-2 and 3 were divided into an investigation of methyl iodide exposed to a simulation of an intense radiation field (ozone with or without ultraviolet light) and an investigation of the radiolysis of a mixture of air and methyl iodide. The experiments in the first section were performed at VTT in Finland in the EXSI-facility, which has been used in previous NROI experiments. The design of the facility is based on the sampling system manufactured previously at VTT [4.16]. The experiments in the second section of the NROI-3 project were performed at Chalmers University of Technology using a gammacell 220.

When methyl iodide was exposed to ozone and UV-radiation in the different conditions the particle formation was instant and extensive. No particles were formed when only methyl iodide was present in the system. The particle mass concentration is increasing with both increased ozone concentration and UV-radiation intensity. Our work at 50ºC when no UVC light was used largely confirms that Jimenez *et. al.* was correct as the yield of iodine particles was low regardless of the ozone level.

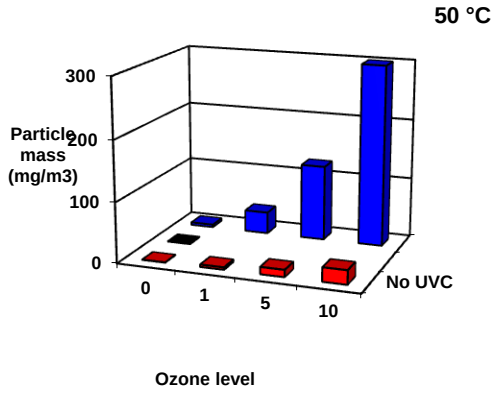

Figure 4.2. The relationship between ozone, UVC light and the yield of particles at 50 °C.

However when the temperature was increased to 90 and 120°C the effect of excluding the ultra violet light became smaller.

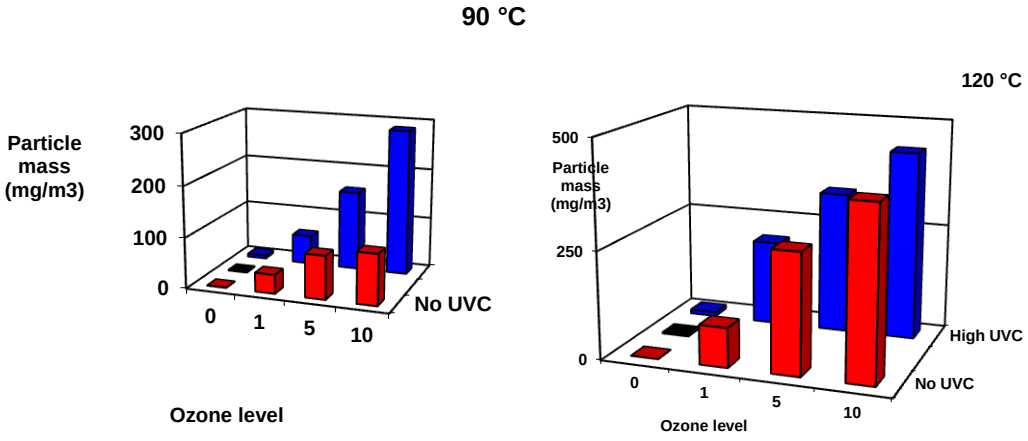

Figure 4.3. The relationship between ozone levels, UV light and the yield of particles at 90°C and 120°C.

This difference can be rationalized by the fact that at the higher temperatures that thermoylsis of the carbon iodine bond provides an alternative means of converting the methyl iodide into methyl radicals and iodine atoms. The behavior is very different to that of freons in the stratosphere where short wavelength UV light is required to start the series of reactions which consume ozone gas. This difference can be rationalized by the fact that the methyl halogen bond becomes less stable with regard to homolytic bond dissociation as the halogen becomes heavier[9]. Assuming that alkyl chloride chemistry can be extrapolated to alkyl iodide chemistry the ho-

[9] Morrison and Boyd, Organic Chemistry, 5th Ed, Inside front cover, Allyn and Bacon, Massachusetts, 1987 states that the bond dissociation energy for the formation of a methyl radical and a halogen atom is 452 KJ mol^{-1} for fluorine, 352 KJ mol^{-1} for chlorine, 293 KJ mol^{-1} for bromine and 234 KJ mol^{-1} for iodine.

molytic bond dissociation energy for higher alkyl iodides should be even lower thus making the thermal reaction of ozone with these compounds even more facile.

Some variation of the particle size was observed when the conditions inside the experimental rig were altered, while no clear relationship exists between the particle size and the ozone concentration the temperature appears to have a strong effect on the size of the particles. Also the UV light does promote the formation of larger particles. It was concluded that the particles are of an iodine oxide, presumably I_2O_5 or I_4O_9.

One conclusion that can be drawn from the ICP-MS data is that the ratio between iodine aerosols and gaseous iodine were far below 1, regardless of the condition in the system. This suggests that a large amount of the gaseous iodine escaped the particle forming process.

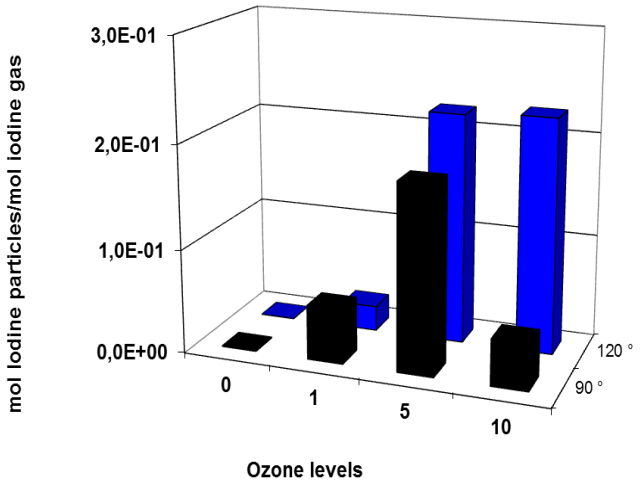

Figure 4.4. The ratio between the amount iodine particles and iodine gas at different ozone concentrations in the system at maximum possible UV-radiation intensity.

In some experiments water was present in the gas mixture. It was found that water promoted the formation of particles and also caused the size of the particles to increase. The presence of water also promoted the conversion of methyl iodide into other iodine species. We reasoned that the particles combine together with the water vapor. These results are in good agreement with the work of Kumas *et. al.* who reported that the iodine oxide particles formed in the marine environment were hydroscopic and tended to absorb water to form iodic acid (HIO_3) [4.17].

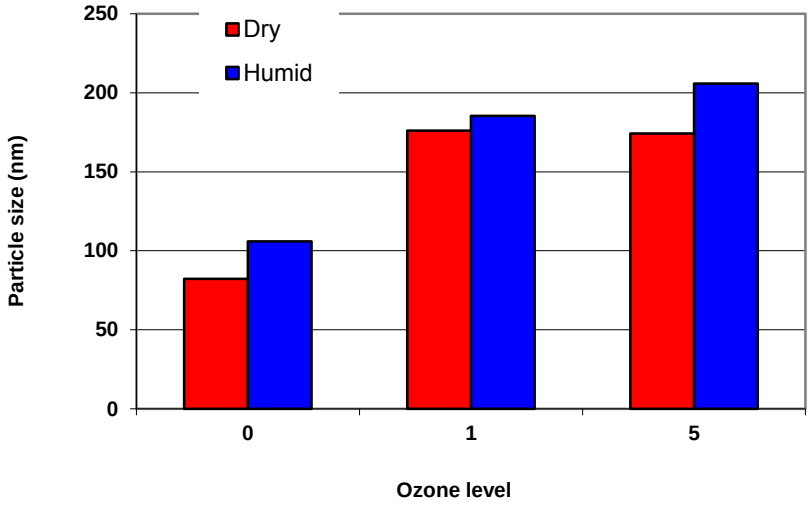

Figure 4.5. The effect of water vapour on the particle size at different ozone concentrations. An UV- field is activated in these conditions.

The outcome of the experiments using gamma rays were not as reproducible as those performed using UV light. Only some of the data of the methyl iodide behaviour in a gamma radiation field are presented in this report because the data is rather uncertain.

Some aerosol particles were formed by irradiation when methyl iodide and ozone were irradiated in the gas phase together. The particle concentration decreased by at least two orders of magnitude when the supply of methyl iodide feeding was discontinued.

Increasing temperatures and UV radiation levels promoted the conversion of methyl iodide into iodine particulates. When water vapour was present the size of these particles was especially large. This formation of large particles under the humid conditions suggests that after a severe accident in a light water reactor, the oxidation of the methyl iodide by ozone will tend to convert the mobile methyl iodide into a less mobile form of iodine. However methyl iodide has less of an ability to form iodine oxide particles than elemental iodine, so this protective effect will be less marked for the alkyl iodides than it will be for elemental iodine.

It had been suggested that short wavelength ultra violet (UVC) light is a good model for gamma radiation for the iodine oxide formation, our experiments in which the two radiations are compared suggests that this assumption is correct.

Due to the short residence time inside the gamma irradiator only a small amount of ozone was formed in air. As a result little of the methyl iodide was converted into aerosol particles unless additional ozone was introduced into the system. When additional ozone was added a high concentration of aerosol particles was observed. This study was the first test with gamma radiation and therefore only preliminary results were obtained.

The extensive results obtained using UV light as a means of breaking the carbon iodine bond can be reconciled to the results obtained by scientists studying the behaviour of iodine in the atmosphere.

4.4 Electrochemical work on the water-iodine system

The reasoning behind the mitigation of the iodine release from a damaged nuclear reactor has traditionally concentrated on the maintenance of a high pH in the containment water. This is because under alkaline conditions the iodine is predominantly in the form of non-volatile compounds [4.18]. This work considered the effect of the redox potential (pE) of the water. The aim of this project was to perform experiments to investigate the validity of the existing models of the iodine chemistry in water.

Speciation calculations of iodine solutions in the pE/pH system were done with the speciation program PHREEQEC. At pH 4, iodide (I^-) is the dominating species at low pE (<10), but at high pE (>10) I_2 is the dominating species. Thus, iodine is most volatile at low pH and high pE (oxidative environment). No other species than I^- and I_2 will be present at pH 4 in significant amounts in the pure iodine-water-system. At pH 10 the speciation of iodine differs significantly compared to the case with pH 4, regardless pE. At low pE (<10), in pH=10 solutions water starts to dissociate[10] at pE=12, I^- is still the dominating species. But already at pE 7 other species, *e.g.* I_2 and especially I_2OH^-, dominate. But, the volatile specie I_2 is under no circumstances the most dominating specie, regardless pE, in water solutions with pH 10. At pE <10 the dominating specie in pH 10 solutions is iodate (IO_3^-), which is non-volatile. These predictions suggest that the risk of formation of volatile iodine species at high pH is fairly low, regardless of the redox potential in the water phase.

The redox potential (pE) has been varied in iodide (NaI) solutions with constant pH (4, 7 and 10). In the pH 4 and 7 solutions the conversion of iodide (I^-) to iodine (I_2) starts to be significant when pE is above 9-10 in the system. A color change was observed at a potential of pE 9 suggesting that iodide was being converted into iodine. The results of these experiments were in good agreement with the prediction made by the calculations. Volatile forms of iodine were observed when the system was oxidizing while under reducing conditions the iodine was in an involatile form.

The experiments were repeated at pH 10, the results from these experiments were very different to those performed under less alkaline conditions. Firstly no color change was observed when the redox potential was altered. This suggests that little if any iodine (or I_3^-) was formed. Also, regardless of the redox potential, the total amount of radioactive iodine which remained in the aqueous layer was constant. This result affirms the PHREEQEC calculations which suggest that the iodine will exist mainly as either iodide or iodate.

When the water was either acidic or neutral (pH $\leq$7) the volatility of the iodine is dependant on the redox potential of the system, oxidizing conditions favor the va-

[10] Water is dissociated to oxygen gas and H^+ ions in: $2H_2O \rightarrow O_2 + 4H^+ + 4e^-$

porization of the iodine, while reducing conditions favor the conversion of iodine into iodide. When the water is alkaline, regardless of the redox potential, no volatile iodine species were formed. Our findings affirm the advice that it is important to exert control over the pH of the water pools within a nuclear plant during an accident. If it is impossible to maintain the water pools in an alkaline state, then the water should have its redox potential controlled.

4.5 The properties of methyl iodide

Methyl iodide is the smallest possible organic iodine compound; it is a liquid at room temperature which has a vapour pressure far higher than that of elemental iodine even at 20 ^{o}C. In common with most alkylation agents it is toxic, despite concerns that it may be a chemical carcinogen [4.19] it is used as a replacement for methyl bromide as a sterilising agent for soil. In California it is commonly used on strawberry farms for this purpose [4.20], it is not considered to be a threat to the ozone layer as it has a far shorter lifetime [4.21] in the lower atmosphere than methyl bromide, a typical freon (such as F-12 dichlorodifluoromethane) or a fire extinguishing agent such as halon-1211 (bromochlorodifluoromethane). The use, sale and production of all three compounds are strictly regulated by international law (Montreal Protocol) [4.22]. It is known that methyl iodide is formed by some marine organisms [4.23]; the methyl iodide which is formed from these organisms is typically converted into iodine oxides which have been observed off the coast of Spain [4.24] and Ireland [4.25]. While the formation of methyl iodide in biological systems might be surprising, it is important to note that methylation of many p-block elements can occur in living cells [4.26]. Even rare elements such as polonium can be converted into the methylated forms [4.27].

The distribution of methyl iodide (MI) between an aqueous and gaseous phase and its hydrolysis have been studied and described based on the kinetics on these reactions in a mathematical model devised at Chalmers. In addition different trapping agents for organic iodides have been studied in an attempt to increase the decontamination factor of the scrubber solution.

The iodine radioactivity in the containment gases will exist mainly in two forms when it reaches the scrubber: Elemental iodine (I_2) and methyl iodide (CH_3I, MeI). The containment air is currently scrubbed using an alkaline (pH > 7) solution of sodium thiosulfate. This scrubbing is a very effective means of removing elemental iodine (I_2). But, the decontamination factor[11] (DF) for methyl iodide (DF ≈ 5) is lower than that of elemental iodine (DF = 100 which is the design value for the scrubbers in the Swedish BWRs).

The work of Borkowski [4.28] studying the partitioning of methyl iodide is used in safety codes like MAAP. Analysis of the mathematical model he used showed that the formula included some errors concerning e.g. the mass balance [4.29]. Based on Borkowski`s data and model a new mathematical model (the Chalmers model) was developed at Chalmers University of Technology. The Chalmers model allows dif-

[11] A decontamination factor of 100 indicates that the gas mixture leaving the scrubber has one hundred times less of a contaminent than the gas mixture entering it.

ferent starting conditions (e.g. initial liquid MI, initial gaseous MI) and can be used to gain the partition coefficient based on experimental data of different origin (in the hydrolysis formed I^- (aq) ions, MI(g) or MI(aq)).

The Chalmers model is based on the following simplified reactions of the partitioning and hydrolysis of methyl iodide. It is assumed that the hydrolysis of MI takes place under formation of iodide ions (I^-) as main inorganic, ionic iodine species according to:

$$MI_g \underset{K_1}{\overset{K_2}{\leftrightarrow}} MI_{aq} \xrightarrow{K_h} MOH + I^- + H^+$$

where K_1 and K_2 are temperature dependent kinetic rate constants, K_h is the hydrolysis rate constant, MeI_g is the amount of methyl iodide in the gas phase, MI_{aq} is the amount of methyl iodide in aqueous phase and MOH is the amount of methanol which is formed in the aqueous phase. The reaction rates for the species are:

$$\frac{dMI_g}{dt} = K_2 MI_{aq} - K_1 MI_g$$

$$\frac{dMI_{aq}}{dt} = K_1 MI_g - K_h I^- - K_2 MI_{aq}$$

$$\frac{dI_{aq}}{dt} = K_h MI_{aq}$$

By solving the set of differential equations, expressions for MI_g, MI_{aq} and I^- can be obtained:

$$MI_g = \frac{1}{2\mu} e^{-\frac{1}{2}t\left(K_h + \frac{AK_2}{V_{aq}} + \mu + \frac{AK_1}{V_g}\right)} \left(-MI_{g0}K_h - MI_{g0}\frac{AK_2}{V_{aq}} - MI_{aq0}\frac{2AK_2}{V_{aq}} + e^{\mu t}\left(MI_{aq0}\frac{2AK_2}{V_{aq}} + \right.\right.$$

$$\left.\left. + MI_{g0}\left(K_h + \frac{AK_2}{V_{aq}} - \frac{AK_1}{V_g} \right)\right) + MI_{g0}\mu\left(1 + e^{\mu t}\right) + MI_{g0}\frac{AK_1}{V_g} \right)$$

with

$$\mu = \sqrt{\left(K_h + \frac{AK_2}{V_{aq}} + \frac{AK_1}{V_g} \right)^2 - \frac{4AK_1K_{\mathrm{h}}}{\mathrm{V_g}}}$$

$$MI_{aq} = \frac{1}{2\mu} e^{-\frac{1}{2}t\left(K_h + \frac{AK_2}{V_{aq}} + \mu + \frac{AK_1}{V_g}\right)} \left(MI_{aq0}K_h + MI_{aq0}\frac{AK_2}{V_{aq}} + e^{\mu t}\left(MI_{aq0}\left(-K_h - \frac{AK_2}{V_{aq}} + \frac{AK_1}{V_g} \right) + \right.\right.$$

$$\left.\left. + MI_{g0}\frac{2AK_2}{V_g} \right) + \mu MI_{aq0}\left(1 + e^{\mu t}\right) - \frac{AK_1}{V_g}\left(2MI_{g0} + MI_{aq0}\right) \right)$$

and

$$I_{aq} = \frac{1}{2\mu}\left(e^{-\frac{1}{2}\eta t}\left(\left(1-e^{\mu t}\right)\left(MI_{aq0}\left(-K_h + \frac{AK_2}{V_{aq}} + \frac{AK_1}{V_g} \right) + MI_{g0}\left(K_h - \frac{AK_2}{V_{aq}} + \frac{AK_1}{V_g} \right) \right) + \right. \right.$$

$$\left. \left. + \mu\left(-MI_{g0} - MI_{aq0} - 2MI_{g0}e^{\frac{1}{2}\eta t} + 2MI_{aq0}e^{\frac{1}{2}\eta t} - MI_{g0}e^{\mu t} - MI_{aq0}e^{\mu t} \right) \right) \right)$$

where η is equal to

$$\eta = K_h + \frac{AK_2}{V_{aq}} + \mu + \frac{AK_1}{V_g}$$

The partition coefficient D for methyl iodide is defined as:

$$D = \frac{MI_{aq}}{MI_g}$$

The gas- and liquid phase volumes and the surface area between the two phases are known in the experiments. By curve fitting the kinetic parameters K_1, K_2 and K_h to experimental data the partition coefficient for a specific temperature can be calculated as:

$$D = \frac{MI_{g0}\frac{2AK_1}{V_g}\left(e^{\mu t}-1\right) + MI_{aq0}\left(-\frac{AK_1}{V_g} + K_h + \frac{AK_2}{V_{aq}} - e^{\mu t}\left(K_h + \frac{AK_2}{V_{aq}} - \frac{AK_1}{V_g} \right) + \mu\left(1+e^{\mu t}\right) \right)}{MI_{g0}\left(\frac{AK_1}{V_g} - K_h - \frac{AK_2}{V_{aq}} + e^{\mu t}\left(K_h + \frac{AK_2}{V_{aq}} - \frac{AK_1}{V_g} \right) + \mu\left(1+e^{\mu t}\right) \right) + MI_{aq0}\frac{2AK_2}{V_{aq}}\left(e^{\mu t}-1\right)}$$

The Chalmers model has been validated against experimental data using two different experimental methods involving two different aggregate states of methyl iodide (liquid and gas). The experiments have been done in temperature ranges between RT (22.7°C) and 70°C and are now further investigated up to 150 /170°C gas phase temperature.

Batch experiments with non-radioactive liquid methyl iodide and radioactive experiments with gaseous methyl iodide in the FOMICAG facility (Facility set-up for On-line Measurements of the Iodine Concentration in an Aqueous and a Gas phase) were performed [4.30]. In the radioactive online experiments the methyl iodide was introduced in gaseous form and it was assumed that the only iodine species in the vapor phase was methyl iodide. The concentration of iodine species measured in the aqueous phase was assumed to be in form of iodide ions. In the non-radioactive batch experiments the dissociation of injected liquid methyl iodide formed iodide ions (I^-(aq)) that was measured with an iodide selective electrode (ISE).

Using the new model it was possible to obtain a close fit between the experimental results and the calculated values, see Figures 4.6 and 4.7.

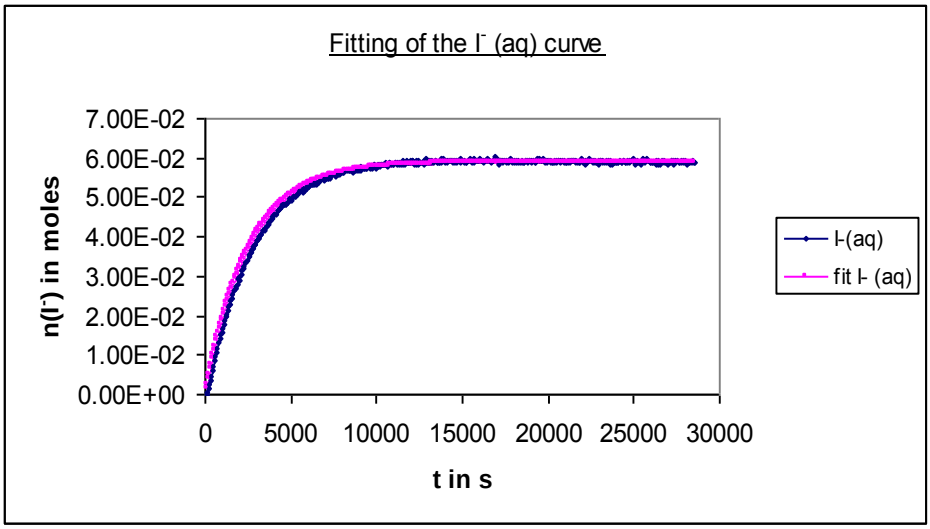

Figure 4.6. Fitting of the I⁻ (aq) curve for pH = 4, room temperature FOMIAG experiment (radioactive).

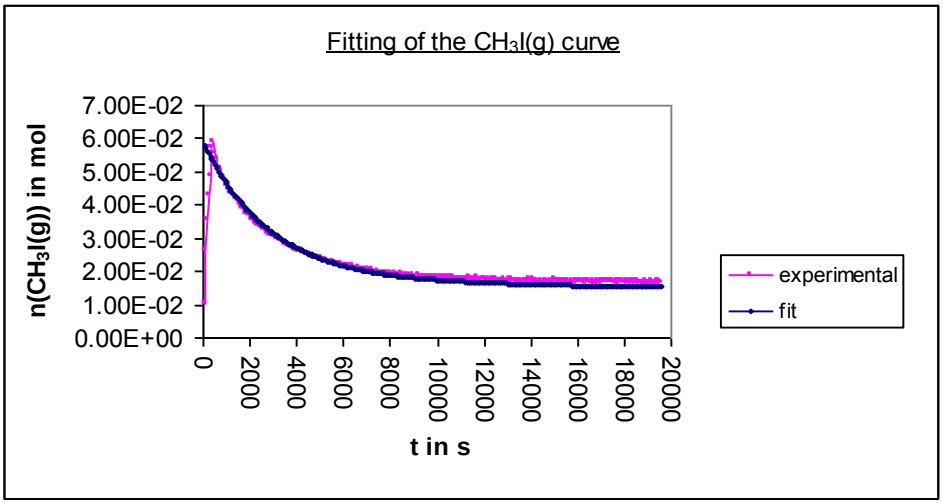

Figure 4.7. Fitting of the MI (g) curve for pH = 4, room temperature FOMIAG experiment (radioactive).

The Chalmers model has corrected the errors occurring in Borkowski`s model. While Borkowski was only able to describe the hydrolysis of methyl iodide (MI(aq)), the Chalmers model is able to describe as well the mass transfer between the gas- and liquid phases. A surface-to-volume dependence is also introduced in the model, which is a further improvement compared to Borkowski's model. Thus, the model can describe the behaviour of gaseous methyl iodide, as well as the behaviour of solvatised methyl iodide and iodide ions in the aqueous phase.

The Chalmers model is generally applicable and can be scaled up for any aqueous-gas systems with known volume ratios and surface area between the two phases.

The Chalmers model allows different starting conditions (initial liquid MeI; initial gaseous MeI; all 3 species MI(aq), MI(g) and I^-(aq) present) and can be used to calculate the partition coefficient based on experimental data. Experimental data of one species only is needed to gain all 3 kinetic parameters and thus the partition coefficient.

The Chalmers model can be applied as well to other species with similar chemical behavior (such as ethyl iodide) according to the simplified reaction scheme of methyl iodide on which the model is based.

4.6 Modification of the scrubber liquid to trap organic iodine

A series of organic additives for the scrubber water were tested in the FOMICAG rig. The reagents tested included pyridine, *N*-methyl imidazole, polymers of 4-vinyl pyridine, cobaloxime [4.31], diisoamylsulfide, *tris*-hydroxymethylphosphine and tributyl phosphine.

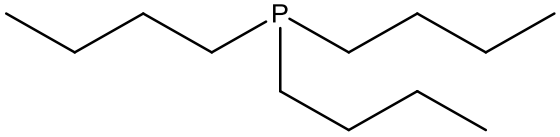

Figure 4.8. The structure of tributyl phosphine.

Of these reagents the tributyl phosphine was found to have an exceptional ability to remove methyl iodide, ethyl iodide and elemental iodine from air. The other non-phosphine reagents are all poorer than aqueous sodium thiosulfate solution. The water soluble *tris*-hydroxymethylphosphine has a disadvantage that it needs to be generated from *tetrakis*-hydroxymethylphosphonium chloride using a base such as sodium hydroxide.

By comparing tributyl phosphine with diisoamyl sulfide it was shown that phosphorus atom in the phosphine is the feature which imparts the useful activity to the compound. Tributyl phosphine is non-corrosive and will be easy to remove from the scrubber medium after a severe nuclear accident. When the flow of gases and liquids is stopped in the scrubber the phosphine will form a liquid layer on top of the water solution.

It is likely that the scrubber can be improved by adding some tributyl phosphine to the tank holding the sodium thiosulfate solution to form a second liquid layer on top of the aqueous scrubbing liquid. The cost of the tributyl phosphine is not likely to be high; it is a semi bulk chemical which was introduced by Shell to industrial hydroformylation as an additive for the cobalt carbonyl based processes.

4.7 Interaction of iodine with the paint film in a LWR containment

The Three Mile Island accident demonstrated that a simple paint layer is an effective prophylactic measure which prevents the contamination of porous surfaces during a radiological accident. Partly as a result of this lesson all concrete and other porous surfaces within a nuclear plant are normally coated with paint. The paint

layers together with the plastics used in electrical products (cables) are a potential source of small organic molecules which could react under the influence of heat or radiation to form alkyl iodides. Conversely the components of the paint (resin, solvents, plasticizer) could react with mobile iodine species forming immobile iodine species thus protecting the public by hindering the escape of iodine from the stricken nuclear power plant.

4.7.1. Characterization of paints

The pyrolysis of paint has been investigated using gas chromatography-mass spectroscopy (GC-MS) and other pyrolysis experiments. The analytical pyrolysis of the paint together with other analytical methods has revealed that the paint sample from the containment wall of the disused Swedish nuclear power plant at Barsebäck is very different to the paint which has been used for repainting the inside of the containment of Ringhals 2.

The Barsebäck paint is not epoxy paint; it appears to be an alkyd paint which is an early version of polyester which is made from glycerol, phthalic anhydride, vegetable oil and sometimes maleic anhydride. The paint solvents present in this old paint were 2-ethoxyethyl acetate, xylene, 2-ethoxyethanol and butyl acetate. By means of GC-MS we found that such species can react with iodine thus forming organoiodine compounds. We expect under the influence of heat and irradiation further small molecule organoiodines will be formed, which increases the likelihood that iodine will enter the gas phase.

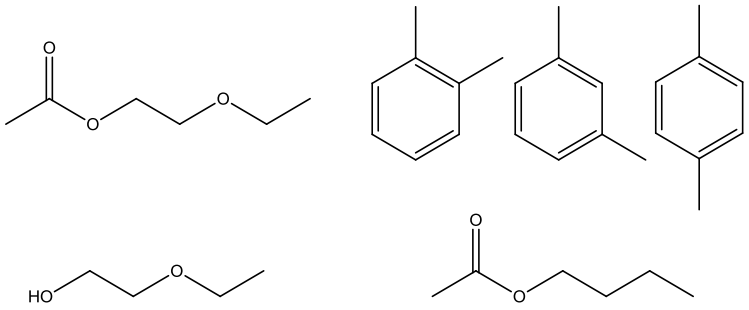

Figure 4.9. Structures of 2-ethoxyethyl acetate, the xylene isomers, 2-ethoxyethanol and butyl acetate.

The solvents used in the modern epoxy paint (TEKNOS AQUA VA) are mainly benzyl alcohol and a mixture of the two texanol mono isobutyrate esters.The paint solvent profile alone suggests that this paint is very different to the older paint.

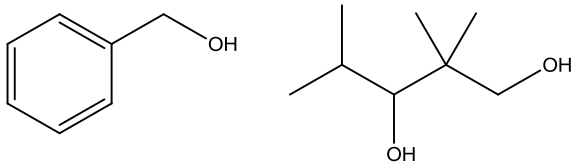

Figure 4.10. Structures of benzyl and texanol alcohols.

In addition a nuclear fuel plant[12] has provided samples of emulsion paint which was removed from a plaster coated wall and a gloss paint which was removed from a steel surface within one of their buildings. It is noteworthy that the residual paint solvent profiles of the four paints are all very different. The main solvents detected in the emulsion paint were methanol, acetone, 2-ethylhexanal, octamethyl tetrasiloxane and 2-ethylhexanol.

The gloss paint from the nuclear site contained xylenes and other alkylbenzenes suggesting that the paint solvent and thinner was a mixture of aromatics from some fraction of petroleum. The gloss paint was also found to contain an aliphatic diester which is thought to be di(2-ethylhexyl) oxalate.

4.7.2. Reaction of organic iodine with paint

It has been shown that the epoxy paint (Teknos Aquapox VA) has a greater ability to absorb radioactive iodine species (both as elemental iodine, methyl iodide) than glass, polystyrene, aluminum, zinc and copper surfaces. A short aging process of one month at 100°C led to a significant decreased uptake ability of the epoxy paint for methyl iodide. Also with increasing doses of radiation the paint was less able to absorb methyl iodide. These results suggest that a thermally or radiologically aged paint film will be less effective in means of removing methyl iodide from air.

It is important to note that the exact speciation of the radioactive organic iodines emitted during a serious nuclear accident is shrouded in mystery. Often "methyl iodide" is detected by using a series of different filters, for example it was assumed by Noguchi and Murata [4.32] that if iodine collected in a DABCO impregnated charcoal layer after passing through other filters (silver mesh, a mechanical filter and phenol loaded charcoal), the iodine will be in the form of methyl iodide [4.33]. However, ethyl iodide is also able to react with the DABCO (triethylene diamine, TEDA) [4.34]. As a result of this inability of DABCO to selectively react with only methyl iodide the existence of ethyl iodide within the gases escaping from a wrecked nuclear plant can not be discounted.

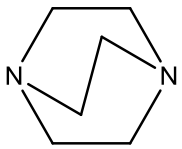

Figure 4.11. The structure of DABCO.

A convenient method for the synthesis of ^{131}I labeled ethyl iodide has been implemented; this is the reaction of sodium iodide with diethyl sulphate. Using radioac-

[12] The operators of the plant kindly provided us with the paint samples but for business reasons they do not wish to be publically associated with the work or for details of the nature of their paint work to become public knowledge. In order to protect their privacy we have entered into a confidentiality agreement in which we have agreed never to reveal the source of the paint or the location of the plant. The paints are simple described as nonradioactive samples of gloss and emulsion paints from a fuel handling facility. The emulsion paint was applied to a plaster wall while the gloss paint was applied to a steel surface inside the building. The same grades of paint are used in the radioactive areas of the building.

tive ethyl iodide, methyl iodide and elemental iodine the absorption on the epoxy paint used at Ringhals has been investigated. For all three forms of iodine a uniform distribution upon the surface was observed, both after the initial absorption and after thermal desorption. This uniform re-release of iodine was also observed for paint samples which were irradiated after the iodine was deposited in the paint layer. Quantitative data of those experiments will be presented later.

4.7.3. Re-release of iodine absorbed in paint

One facet of the study is the re-release of iodine from paint which has been previously exposed to iodine compounds before being subject to heating or immersion in water. The leaching of ^{131}I from paint surfaces by water at room temperature starts immediately upon immersion. Examination of the leaching water with ion chromatography revealed that most of the leached iodine is in the form of iodate and iodide ions. It has been found that a high concentration of chloride favors the leaching of the iodine (see below). This can be rationalized by the hypothesis that by ion exchange the chloride is able to liberate the iodine (as iodide anions).

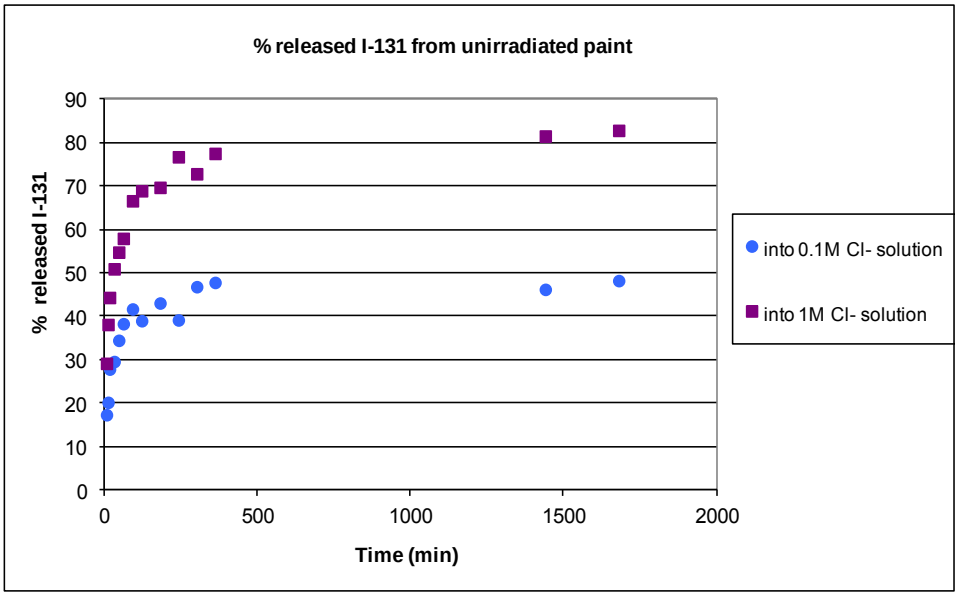

Figure 4.12. A graph showing some results from a leaching test.

Paint samples which had been exposed to radioactive iodine in a range of forms were heated to simulate a prolonged overheating of the containment. The surfaces were examined using autoradiography while the total amount of radioactive iodine in the samples was estimated with gamma counting. The use of the two methods enables the activity at the surface (beta) to be distinguished from the activity in the bulk (gamma). This work suggested that the iodine on the surface of the paint was lost while the iodine deep within the paint film was retained.

On storage at room temperature a sample of paint released *circa* one third of its radioactivity, while samples stored at higher temperatures re-released larger amounts of radioactive iodine. However even after pyrolysis at 300^{o}C the paint retained 12 % of the original radioactivity it absorbed. This behavior can be rationalized by using a multiple compartment model of the iodine. While much of the io-

dine remains in the form of methyl iodide some of the iodine has been converted into an involatile form by chemical reactions. Our results suggest that irradiation of the paint decreases its ability to retain radioactive iodine. Quantitative data showing the change of ^{131}I activity on the surface in comparison to the total by the paint originally absorbed activity from different iodine species (I_2; MeI and EtI) will be presented later.

As part of our investigation of the release of iodine from paint, a sample of the Teknos Aquapox VA paint was treated with iodine monochloride before being washed with organic solvent to remove the excess of this iodination reagent. After drying the sample was examined with pyrolysis-GCMS to discover if the paint could form organic iodine compounds when it was heated. During all of the sequential pyrolysis experiments (275, 360, 500 and 750^{o}C) some methyl and ethyl iodides (ions at 156, 142 and 127) were detected by gas chromatography.

The chemical nature of the paint varies wildly between sites and the newer paint can not (even after aging) be used as a surrogate for the older paint. The modern epoxy paint (Teknos Aquapox VA) has a great ability to immobilize methyl iodide. Both heating and irradiation of the paint reduce the ability of the paint to react with methyl iodide and the ability of the paint to retain the radioactive iodine. This decrease in the ability of the paint to absorb and retain radioiodine may be important when deciding what protective effect the paint will have during an accident.

The epoxy paint tended to convert organic iodine (methyl iodide) into ionic inorganic iodine (iodide and iodate), hence the paint will convert the volatile organic iodines into less volatile forms of iodine. However we have shown that the same paint is able to produce both methyl and ethyl iodides when heated.

4.8 Participation in SARNET

During APRI-7 Chalmers has been a member of WP-8, Source Term, in SARNET. This work package is divided into three sub work packages (WP-8.1 - WP-8.3).

The research in WP-8.1 is dedicated to the effects of air-ingress-accidents, the oxidizing impact of the source term. Mainly the participants in this sub work package are investigating the behavior of ruthenium in the primary system (transport to the containment) and in the containment (retention mechanisms). Earlier Chalmers has been an active member of this sub work package, but during APRI-7 the participation has only been at observation level. However, during APRI-8 Chalmers has planned to take a more active part by perform experiments of the behavior of ruthenium in the containments (revaporisation and ruthenium chemistry in aqueous solutions).

Some examples on-going experiments in WP-8.1 are:

- CEA is investigating the transport of ruthenium released from MOX fuel in air/steam mixture.
- AEKI are studying ruthenium transport and the influence of different surfaces.

- IRSN is working with high temperature ruthenium chemistry experiments in the gas phase and interaction with surfaces in the primary system.
- VTT is working with ruthenium revaporisation from primary system surfaces.
- EDF is modeling the ruthenium behavior in the containment using MAAP4 code.
- USNRC is studying the aqueous chemistry of ruthenium and molybdenum.

In WP-8.2 the research is about the iodine behavior in the containment during a severe accident. There are several research projects on-going in WP-8.2:

- PSI are performing experiments on the effect of the impurities on iodine volatility from sump water.
- EPICUR tests conducted by IRSN; investigation particularly on the reaction of iodne with paint under irradiation and formation of volatile iodine species.
- Experiments with the THAI facility; iodine oxide formation/destruction and the interaction between iodine behavior and containment thermal hydraulics.

A description of the experiments and major results from the experiments are presented in Haste *et al*. [4.36]. In WP-8.2, Chalmers has contributed with experiments described in Section 4.3.

In WP-8.3, where Chalmers is not participating, the participants are trying to bring research results into reactor applications. The main topics in WP-8.3 are

- Assessment of the significance of iodine chemistry on source term uncertainties.
- Code calculations benchmarks on *e.g.* THAI and PHEBUS-FP experiments.
- Creation and maintenance of reference data-books on iodine and ruthenium chemistry.

4.9 References

4.1 F.A. Cotton and J. Wilkinson, Advanced Inorganic Chemistry, 5th Ed, page 544, John Wiley and Sons, New York, 1988.

4.2 W.A. Volkert and T.J. Hoffman, Chemical Reviews, 1999, 99 (9), 2269-2292

4.3 Taghipour, F., Evans, G. J., Radiolytic Organic Iodide Formation under Nuclear Reactor Accident Conditions, Environ. Sci. Technol. 2000, 34, 3012-3017

4.4 Weber, C. F., Beahm, E. C., Kress, T. S., Iodine Chemical forms in LWR Severe Accidents, Third CSNI Workshop on Iodine Chemistry in Reactor Safety, Tokai-mura, Japan, September 11-13 1991

4.5 F.J. Sandalls, M.G. Segal and N. Victorova, *Journal of Environmental Radioactivity*, 1993, **18**, 5-22.

4.6 B. Clément, L. Cantrel, G.. Ducros, F. Funke, L. Herranz, A. Rydl, G.. Weber, C. Wren, State of the art report on iodine chemistry, NEA/CSNI/R(2007)1, 2007.

4.7 T. Kärkelä, J. Holm, A. Auvinen, C. Ekberg, H. Glänneskog, U. Tapper, R. Zilliacus, Gas Phase oxidation of Elemental Iodine in Containment Conditions, Proceedings of the 17th International Conference on Nuclear Engineering, ICONE17, Belgium, 12-16 July, 2009.
T. Kärkelä, J. Holm, A. Auvinen, C. Ekberg, H. Glänneskog, EXperimental Study on Iodine chemistry – Containment experiments with elemental iodine, NKS-204 report, 2009.
J. Holm, T. Kärkelä, A. Auvinen, H. Glänneskog, C. Ekberg, Experimental study on iodine chemistry (EXSI) Containment experiments with methyl iodide NKS-220 report, 2010.
T. Kärkelä, J. Holm, A. Auvinen, R. Zilliacus, T. Kajolinna, U. Tapper ,C. Ekberg, H. Glänneskog, Gas Phase Reaction of Organic Iodine in Containment Conditions, Conference Proceedings, ICAPP 10, San Diego, USA, 13-17 June, 2010.

4.8 Wampler, G.A. Bishea and W.J. Simonsick, Journal of Analytical and Applied Pyrolysis, 1997, **40-41**, 79-89.

4.9 N. Tang, A. W. Castleman Jr., Kinetics of γ-induced decomposition of methyl iodide in air, J. Phys. Chem., 74(22) 3933-39 1970.

4.10 S. Dickinson, H. Sims, Iodine Data Book Part 5: Gaseous Iodine Chemistry, SARNET-ST-P50, 2007.

4.11 J. L. Jimenez, R. Bahreini, D.R. Cocker, New particle formation from photooxidation of diiodomethane (CH_2I_2), J. Geophys. Res.-A., 108(D10), art. no. 4318, 2003.

4.12 R.A. Cox, G..B. Coker, Absorption cross-section and kinetics of IO in the photolysis of CH_3I in the presence of ozone, *J. Phys. Chem*, 1983, **87**, 4478–4484.

4.13 S. Dickinson, National Nuclear Laboratory, Personal Communications, 2010.

4.14 F. Funke, Literature Review on the Radiolytic Oxidation of Molecular Iodine in the Containment Atmosphere, EC Report SAM-ICHEMM-D002, 2000.

4.15 J. L. Jimenez, R. Bahreini, D.R. Cocker, New particle formation from photooxidation of diiodomethane (CH_2I_2), J. Geophys. Res.-A., 108(D10), art. no. 4318, 2003.

4.16 Auvinen, J. Lyyränen, T. Kärkelä, L. Kåll, R. Järvinen, J. Roine, S. Vänttinen, Qualification of the sampling systems for CHIP test facility – Final report, VTT TK504, VTT-R-11382-07, 2007.

4.17 R. Kumas, R.W Saunders, A.S. Mahajan, J.M.C. Plane and B.J. Murray, Atomspheric Chemistry and Physics, 2010, **10**, 12251 to 12260.

4.18 E.C. Beahm, R.A. Lorenz, C.F. Weber, Iodine Evolution and pH control, NUREG/CR-5950, Oak Ridge National Laboratory, 1992.

4.19 http://articles.latimes.com/2009/aug/03/local/me-fumigants3

4.20 Duniway, JM, *Phytopathology*, 2002, **92**, 1337-1343.

4.21 D. Youn, K.O. Patten, D.J. Wuebbles, H. Lee, C.W. , *Atmospheric Chemistry and Physics*, 2010, **10**, 10129-10144.

4.22 http://ozone.unep.org/Publications/MP_Handbook/Section_1.1_The_Montreal_Protocol/

4.23 G. Gribble, *Journal of Chemical Education*, 1994, **71**, 907-911.

4.24 A.S. Mahajan, M. Sorribas, J.C.G. Martin, S.M. MacDonald, M. Gil, J.M.C. Plane, A. Saiz-Lopez, *Atmospheric Chemistry and Physics*, 2011, **11**, 2545-2555.

4.25 L.J. Carpenter, W.T. Sturges, S.A. Penkett, P.S. Liss, B. Alicke, K. Hebestreit and U. Platt, Journal of Geophysical Research-Atmospheres, 1999, **104**, 1679-1689.

4.26 G.M. Gadd, *Fems Microbiology Reviews*, 1993, **11**, 297-316.

4.27 N. Momoshima, L.X. Song, S. Osaki and Y. Maeda, Y, *Environmental Science & Technology*, 2001, **35**, 2956-2960.

4.28 Borkowski, R., Untersuchungen zum Chemischen Verhalten des Methyliodides bei schweren Störfällen in Druckwasserreaktoren, KfK 3968, 1985

4.29 S. Holgersson, Chalmers Technical University, Nuclear Chemistry, personal communication, 2009

4.30 H. Glänneskog, Y. Albinsson, J-O. Liljenzin and G. Skarnemark, *Nuclear Instruments and Methods in Physics Research,*2003, **498**, 517-521.

4.31 L.G. Marzilli, P.J. Toscano, L. Randaccio, N. Bresciani-Pahor, M. Calligaris, Journal of the American Chemical Society, 1979, 101, 6754-6756.

4.32 H. Noguchi and M. Murata, Journal of Environmental Radioactivity, 1988, 7, 65-74.

4.33 DABCO is a common additive in the charcoals used in respiratory protection and the nuclear industry. For examples of its use see J.J. Mahle, G.W. Peterson, B.J. Schindler, P.B. Smith, J.A. Rossin, G.W. Wagner, *Journal of Physcial Chemistry,* 2010, **114**(47), 20083-20090 and J.C. Wren , W. Long, C.J. Moore and K.R. Weaver¸ *Nuclear Technology*, 1999, **125**(1), 13-27.

4.34 J-Y.Kazock, M. Taggougui, B. Carre, P. Willmann, D. Lemordant, Synthesis, 2007, (24), 3776-3778.

4.35 J. Holm, C. Ekberg, H. Glänneskog, Journal of Nuclear Materials, xx (2009).

4.36 T. Haste, A. Auvinen, J. Colombian, F. Funke, G. glowa, S. Güntay, J. Holm, T. Kärkelä, G. Langrock, G. Poss, B. Simondi-Teisseire, S. Tietze and G. Weber, Containment Iodine Experiments in the SARNET 2 Project, 5th European Review Meeting on Severe Accident Research (ERMSAR 2012), Cologne (Germany), March 21-23, 2012.

5. SLUTSATSER OCH REKOMMENDATIONER

5.1 Sammanfattning av projektet

APRI 7 har följt den internationella forskningen och utvärderat resultaten. Det fortsatta stödet till KTH har gett ökad kunskap om möjligheten att kyla den smälta härden i reaktortanken och om processer i samband med kylbarheten i inneslutningen samt vid ångexplosioner. Stödet till Chalmers har gett ökad kunskap om haverikemi, främst jods uppförande i inneslutningen efter ett haveri.

5.1.1. Internationella forskningsprojekt

Deltagande i CSARP ger tillgång till en mängd information om olika fenomen av betydelse för händelseförlopp vid svåra haverier som kommer fram från internationell forskning. Informationsutbytet sker huvudsakligen vid en årlig konferens. Deltagandet ger också tillgång till beräkningskoder utfärdade av NRC, varav MELCOR används i flera projekt.

SARNET utgör en viktig plattform för forskningen inom svåra haverier och främjar utbyte av kunskap och erfarenheter. De forskningsprojekt som stöds av APRI ingår i SARNET. I gengäld får APRI och forskningsinstitutionerna tillgång till de forskningsresultat som genereras i de övriga deltagarländerna. I APRI 7-projektet har forskningsinstitutionerna KTH och Chalmers varit aktiva.

Vad gäller PHEBUS-projektet som pågått under 20 år, är det svårt att beskriva alla resultat men några viktiga observationer och lärdomar har sammanställts i rapporten, se avsnitt 2.3. Ett avslutande seminarium kommer att hållas sommaren 2012 i Aix-en-Provence. För att behålla viss kritisk personal, startades det uppföljande forskningsprogrammet ISTP (International Source Term Project). Även detta projekt har nu avslutats och analysarbetet pågår. Troligen kommer även resultaten från detta projekt att presenteras vid PHEBUS-seminariet.

I MCCI 2 - programmet har fortsatta studier av härdsmältans kylbarhet om vatten påförs ovanifrån genomförts. Det noteras att experimentuppställningarna främst är tillämpliga för anläggningar med ”dry cavity” (haveristrategi där smältan inte faller i vatten). För svenska förhållanden har resultaten därför varit av begränsat intresse.

OECD-projektet SERENA, fas 2, (Steam Explosion Resolution for Nuclear Applications) har syftat till att bringa klarhet i ångexplosionsfenomen genom att genomföra ett begränsat antal väl designade experiment med avancerad mätutrustning. Experimenten genomförs i den s.k. TROI-anläggningen som finns hos KAERI i Sydkorea samt i KROTOS-anläggningen vid CEA:s Centre of Cadarache i Frankrike. Projektet håller på att slutföras och ett slutseminarium planeras till 13–15 november 2012.

OECD-projektet BIP (Behaviour of Iodine Project) har syftat till studier av jodkemin inom följande områden: a) Kvantifiering av processer i färg och på ytor som bildas av organisk jod, b) Mätning av adsorptions/desorptions-konstanter på ytor i inneslutningen som funktion av temperatur, relativ fuktighet och atmosfärssammansättning och c) Analys av utvalda RTF-experiment. Hittills genomförd

forskning visar att organisk jod bildas men bildningsmekanismen är fortfarande inte känd.

5.1.2. Smältans kylbarhet i reaktortanken

Ett beräkningsverktyg, ECM/PECM, med syfte att analysera en härdsmälta i reaktortankens nedre plenum med CFD-teknik har utvecklats och kopplats till ett hållfasthetsberäkningsprogram. Verktyget tar hänsyn till den komplexa geometrin i reaktortankbotten för BWR-reaktorer och olika haveriscenarier. Modellen har validerats.

Resultaten indikerar att kylning via drivdonsflöde bara kan förhindra tankgenomsmältning om en mindre del av härden har relokerat. Om en mer omfattande relokering har skett, indikerar resultaten att kylning via drivdonsflöde istället kan leda till en ogynnsam tankgenomsmältningmod som ökar risken för en icke-kylbar konfiguration i reaktorinneslutningen.

5.1.3. Smältans kylbarhet i reaktorinneslutningen

Tidigare experiment och analyser har visat att smältans kylbarhet i inneslutningens kondensationsbassäng är beroende av vilken form grusbädden (”debris bed”) har då den slutligen hamnar på bassänggolvet.

KTH:s DEFOR-experiment visar att porositeten hos den fragmenterade smältan är hög, upp till 45 – 70 % vilket är högre än 40 % som man tidigare antagit. Porositeten förefaller också vara oberoende av smältans sammansättning och underkylning på bassängvattnet. En ökad porositet är gynnsam ur kylbarhetssynpunkt. Experimenten visar också att partiklarna till största delen är icke-sfäriska med en grov yta. Minskande vattendjup och/eller ökande diameter på smältstrålen ökar risken för en icke-kylbar konfiguration.

Genomförda DEFOR-experiment och analyser har bekräftat att geometrin av den grusbädd som bildas påverkas i hög grad av den vattencirkulation som uppkommer i bassängen p.g.a. smältans resteffekt. Detta betyder bl.a. att konfigurationer med ett isolerande lager av fina partiklar ovanpå grusbädden är mindre sannolika. Dessutom bildas kanaler i grusbädden p.g.a. vattencirkulationen vilket bidrar till ökad kylbarhet.

POMECO-experiment har givit data för validering av beräkningsmodeller för kylbarhet av en grusbädd. Resultaten visar att så länge det går att undvika ”melt-cake”, är konfigurationen kylbar.

5.1.4. Ångexplosioner i reaktorinneslutningen

I SERA-experimenten studeras ångexplosionsförloppet genom studier av enskilda smältdroppar. Syftet är att få ökad förståelse av fysiken bakom ångexplosioner för att kunna förklara varför olika material har olika benägenhet att explodera samt att kunna bestämma explosionens verkningsgrad.

Under perioden har testmatrisen utökats med experiment med simulanta material (binära oxider) med högre smälttemperatur. Experimenten är genomförda med såväl

eutektisk[13] som icke-eutektisk sammansättning. Resultaten indikerar att skillnader i energiutbyte mellan dessa sammansättningar finns endast vid låg överhettning.

5.1.5. Jodkemi vid svåra haverier

Under perioden har samarbetet mellan Chalmers och VTT fortsatt avseende studier av radiolytisk oxidation av jod för att få ökad förståelse av specieringen av de slutliga produkterna. Testmatrisen har utvidgats till att inkludera gammabestrålning av gasfasen.

Experiment har undersökt hur metyljodid påverkas av ozon, vattenånga, UV-bestrålning och gammastrålning. Resultaten visar att ökande temperatur och UV-bestrålning gynnar omvandling av metyljodid till jodoxidpartiklar samt leder till ökande partikelstorlekar. Närvaro av vattenånga ger ökad partikelbildning och ökad partikelstorlek. Det har också bekräftats att UV-bestrålning på ett acceptabelt sätt kan imitera gammastrålning vid studier av jodoxidbildning.

5.1.6. Potentiostatmätningar av jod-vattensystemet

Experiment och analyser har klarställt att redoxpotentialen i en vattenmiljö har en underordnad betydelse för förmågan att kvarhålla jod så länge som pH hålls ovanför det sura området.

5.1.7. Egenskaper hos metyljodid

Metyljodid som vållar störst bekymmer vad gäller omgivningskonsekvenser vid en radiologisk olycka, har studerats genom att utveckla teorin som Borkowski lade fram angående hydrolys av metyljodid i vatten. En analytisk modell för hydrolys av metyljodid i vatten har tagits fram på Chalmers. Modellen är mycket grundligt genomarbetad och har åtgärdat sådana brister som identifierats i Borkowskis motsvarande modell. Med modellens hjälp är det möjligt att ta fram temperaturberoende hastighetskonstanter som tillsammans ger oss ett uttryck för fördelningen av metyljodid mellan vatten och gas vid olika temperaturer.

5.1.8. Modifiering av scrubberlösning

En organisk fosforförening har visat sig effektivt kunna fånga metyljodid i en vattenlösning. Genom att tillsätta denna förening till natriumtiosulfatlösningen i scrubbern, skulle dess jodavskiljande förmåga kunna förstärkas och källtermen kunna reduceras.

5.1.9. Reaktioner mellan jod och färg

Beståndsdelarna i alkydfärg (Barsebäck) och epoxyfärg (Ringhals) har analyserats. Av dessa har ingående lösningsmedel visats kunna bilda flyktiga organiska jodider. Å andra sidan kan färgen också absorbera såväl organisk jod som elementär jod vilket är gynnsamt ur utsläppssynpunkt. De exakta mekanismerna är inte klarlagda, dock påverkar ökande temperatur och strålning absorptionen negativt.

[13] Eutektiskt material är ett material där blandningsförhållandet för de ingående ämnena är sådant att blandningen stelnar/smälter vid samma temperatur.

5.2 Slutsatser

Från projektet APRI 7 kan följande slutsatser dras:

- Deltagande i CSARP har ökat kunskapen om svåra haverier genom utbyte av forskningsresultat och givit tillgång till haverianalyskoden MELCOR.
- Deltagande i SARNET är viktigt för att samordna forskning med andra länder och utnyttja andra forskningsresultat.
- PHEBUS-projektet har satt kemi och aerosolbeteende inom svåra haverier i fokus.
- Genom ökad tillförsel av medel till KTH och Chalmers från SSM och industrin har kontinuiteten avseende forskning om svåra haverier kunnat säkras.
- Ett beräkningsverktyg har vidareutvecklats för att analysera en härdsmälta i reaktortankens botten. Beräkningarna tyder på att ett kylflöde genom drivdonen kan ge möjlighet att fördröja tankgenomsmältning men riskerar att försvåra det fortsatta förloppet om tankgenomsmältning ändå sker.
- Experiment och analyser visar att porositeten hos grusbädden är hög och att geometrier med ett isolerande lager av fina partiklar ovanpå en grusbädd är mindre sannolika. Båda resultaten visar på ökad kylbarhet jämfört med tidigare bedömningar. Minskande vattendjup och/eller ökande diameter på smältstrålen ökar risken för en icke-kylbar konfiguration.
- Genomförd forskning om ångexplosioner har gett oss ökad detaljkunskap men denna är ännu inte tillräcklig för att ge full förståelse av förloppet vid en ångexplosion i samband med en härdsmälta.
- Baserat på resultaten av forskningen vid KTH, görs bedömningen att det inte är realistiskt att på helt deterministisk grund kunna avgöra hur en haverisekvens utvecklas.
- Förståelsen av det grundläggande sambandet för fördelning av metyljodid mellan vatten och gasfas har ökat.
- Experiment och analyser har klarställt att redoxpotentialen i en vattenmiljö har en underordnad betydelse för förmågan att kvarhålla jod så länge som pH hålls ovanför det sura området.
- Det finns potential att förstärka scrubberns jodavskiljande förmåga med tillsats av en organisk fosforförening.

5.3 Rekommendationer

Följande rekommendationer lämnas inför fortsättningen av APRI-projektet:

- Fortsatt deltagande i internationella projekt som CSARP, SARNET, PHEBUS, THAI, SERENA2 och BIP2.
- Uppföljning av haveriet i Fukushima.
- Fortsatta studier av smältans kylbarhet i reaktortankens botten.
- Fortsatta studier av smältans kylbarhet i reaktorinneslutningen.

- Fortsatta studier av de mekanismer som styr ångexplosioner.
- Pröva om tillämpning av ROAAM-teknik kan leda till att haverisekvensen kan bestämmas på ett bättre sätt och om slutsatser kan dras om de lösningar som valts i den svenska strategin för haverihantering ger ett tillräckligt skydd för omgivningen.
- Fortsatta studier av haverikemi i inneslutningen avseende jod och andra fissionsprodukter.
- Fortsatta studier av metoder för att förbättra retentionen av organisk jod.

6. FÖRKORTNINGSLISTA

AECL	Atomic Energy of Canada Limited
ANL	Argonne National Laboratory
APRI	Accident Phenomena of Risk Importance
ASTEC	Accident Source Term Evaluation Code
BIP	Behaviour of Iodine
BWR	boiling water reactor
CCI	Core-Concrete Interaction
CFD	computational fluid dynamics
CHF	critical heat flux
CRGT	control rod guide tube
CSARP	Cooperative Severe Accident Research Program
DCH	Direct Containment Heating
DECOSIM	code for debris bed coolability simulation
DEFOR	debris bed formation
DEM	discrete element method
DHF	dryout heat flux
LIVE	Late In-Vessel Phase Experiments
LWR	light water reactor
EC	European Commission
ECM	effective convectivity model
EDF	Electricité de France
ERMSAR	European Review Meetings on Severe Accident Research
FCI	fuel coolant interaction
FP	framework programme
FPT	Fission Product Test
IGT	instrumentation guide tube

INCO	in-vessel coolability
IRSN	Institut de Radioprotection et de Sûrité Nucléaire
ISTP	International Source Term Project
IVR	in-vessel retention
KROTOS	a small-scale test facility for FCI (steam explosion) study at CEA
KTH	Royal Institute of Technology
LOCA	loss of coolant accident
LWR	Light Water Reactor
MCCI	Melt Corium Concrete Interaction
MET	Melt Eruption Test
MELCOR	code for integral simulation of severe accident developed by USNRC
MISTEE	micro interactions of steam explosion energetics
MSWI	melt structure water interactions
NCG	non-condensable gas
NPP	nuclear power plant
NRC	Nuclear Regulatory Commission
NROI	Nordic Research on Radiolytic Oxidation of Iodine
OECD	Organisation for Economic Co-operation and Development
PECM	phase-change ECM
POMECO	porous media coolability
PSA	probabilistic safety analysis
PWR	pressurized water reactor
ROAAM	risk oriented accident analysis methodology
RPV	reactor pressure vessel
RTF	Radioiodine Test Facility
SAID	severe accident information distillation
SA	severe accident

SAM	severe accident management
SARNET	severe accident research network of excellence
SBO	station blackout
SEE	steam explosion energetics
SERENA	Steam Explosion REsolution for Nuclear Applications
SIMECO	simulation of melt coolability
SSWICS	Small-Scale Water Ingression and Crust Strength
TROI	a medium-scale test facility for FCI (steam explosion) study at
VAPEX	code for FCI simulation developed in Russia

2012:12

Strålsäkerhetsmyndigheten har ett samlat ansvar för att samhället är strålsäkert. Vi arbetar för att uppnå strålsäkerhet inom en rad områden: kärnkraft, sjukvård samt kommersiella produkter och tjänster. Dessutom arbetar vi med skydd mot naturlig strålning och för att höja strålsäkerheten internationellt.

Myndigheten verkar pådrivande och förebyggande för att skydda människor och miljö från oönskade effekter av strålning, nu och i framtiden. Vi ger ut föreskrifter och kontrollerar genom tillsyn att de efterlevs, vi stödjer forskning, utbildar, informerar och ger råd. Verksamheter med strålning kräver i många fall tillstånd från myndigheten. Vi har krisberedskap dygnet runt för att kunna begränsa effekterna av olyckor med strålning och av avsiktlig spridning av radioaktiva ämnen. Vi deltar i internationella samarbeten för att öka strålsäkerheten och finansierar projekt som syftar till att höja strålsäkerheten i vissa östeuropeiska länder.

Strålsäkerhetsmyndigheten sorterar under Miljödepartementet. Hos oss arbetar drygt 250 personer med kompetens inom teknik, naturvetenskap, beteendevetenskap, juridik, ekonomi och kommunikation. Myndigheten är certifierad inom kvalitet, miljö och arbetsmiljö.

Strålsäkerhetsmyndigheten
Swedish Radiation Safety Authority

SE-171 16 Stockholm
Solna strandväg 96

Tel: +46 8 799 40 00
Fax: +46 8 799 40 10

E-mail: registrator@ssm.se
Web: stralsakerhetsmyndigheten.se